

# Models for a quantum atomic chain coupled to a substrate

Von der Fakultät für Mathematik und Physik  
der Gottfried Wilhelm Leibniz Universität Hannover  
zur Erlangung des akademischen Grades

DOKTOR DER NATURWISSENSCHAFTEN  
Dr. rer. nat.

genehmigte Dissertation  
von

**M.Sc. Anas Abdelwahab**

2018

Referent: Prof. Dr. Adrian E. Feiguin

Korreferent: Prof. Dr. Eric Jeckelmann

Tag der Promotion: 05.02.2018

# Contents

<b>1</b>	<b>Introduction</b>	<b>1</b>
1.1	1D metals: Theory and experiments . . . . .	1
1.2	1D metal on a semiconducting substrate: experimental realization . . . . .	6
1.3	Theoretical approaches for a 1D metal on a substrate . . . . .	10
1.4	Density matrix renormalization group: a numerical method for 1D systems	11
<b>2</b>	<b>Asymmetric 2-leg ladder system</b>	<b>21</b>
2.1	The model . . . . .	21
2.1.1	Weak interactions . . . . .	22
2.1.2	Strong interactions . . . . .	24
2.1.3	Chain limit . . . . .	25
2.1.4	Dimer limit . . . . .	25
2.2	Hartree-Fock approximation at half filling . . . . .	27
2.3	Ground-state properties and excitation gaps . . . . .	33
2.3.1	Definitions of excitation gaps . . . . .	33
2.3.2	Excitation energies at half filling . . . . .	34
2.3.3	Density profiles . . . . .	38
2.3.4	Correlation functions and ladder doping . . . . .	45
2.4	Comparison with Quantum Monte Carlo results . . . . .	52
2.5	Discussion . . . . .	56
<b>3</b>	<b>Ladder mapping and construction of quasi one-dimensional models</b>	<b>59</b>
3.1	Wire-substrate model . . . . .	59
3.1.1	The substrate . . . . .	60
3.1.2	The wire . . . . .	62
3.1.3	The wire-substrate hybridization . . . . .	62
3.1.4	Generalizations . . . . .	63
3.2	Ladder representation . . . . .	64
3.2.1	Impurity subsystems . . . . .	64
3.2.2	Chain representation . . . . .	65
3.2.3	Real-space representation . . . . .	68
3.2.4	Alternate representation for the insulating substrate . . . . .	70
3.3	Effective narrow ladder model (NLM) . . . . .	71
3.3.1	Noninteracting wire . . . . .	72
3.3.2	Interacting wire : testing with quantum Monte Carlo . . . . .	77
3.3.3	Interacting wire : testing with DMRG . . . . .	79

3.4	Summary . . . . .	81
<b>4</b>	<b>NLM for correlated Hubbard wires</b>	<b>82</b>
4.1	NLM for insulating Hubbard wire . . . . .	83
4.2	NLM for metallic Hubbard wire . . . . .	91
4.3	Discussion . . . . .	99
<b>5</b>	<b>Summary and outlook</b>	<b>101</b>

## Abstract

One-dimensional correlated conductors are described by the Luttinger liquid theory. Recently, several systems of atomic wires on semiconducting substrates have been reported to host some of the Luttinger liquid properties but without any explanation of the influence of the substrate on the one-dimensional electrons. This thesis addresses this issue by investigating two approaches for modeling wire-substrate systems.

The first model consists of an asymmetric 2-leg ladder system with one leg described using a Hubbard chain and an other leg described by a one-dimensional electron gas. The two-legs are connected by nearest-neighbor inter-leg hopping. This model revealed rich physics through the different phases that are uncovered as a function of the Hubbard interaction and the rung hopping at half filling. These phases include a Luttinger liquid at very weak interchain hopping, a Kondo-Mott insulator at moderate interchain hopping or strong Hubbard interaction and a spin-gapped paramagnetic Mott insulator at intermediate values of the rung hopping and the interaction. The last phase is a correlated band insulator for large rung hopping. This model is found insufficient to represent wire-substrate systems but it is useful, as a minimal model, to study coexistence and proximity effects of different quasi-long-range orders that could be relevant in higher-dimensions.

The second approach presents the successful construction of a suitable model for wire-substrate systems. The modeling is started by constructing a lattice Hamiltonian for a one-dimensional quantum wire on a three-dimensional substrate. This model is mapped onto an effective two-dimensional lattice using the Lanczos algorithm and then it is approximated by narrow ladder models that can be investigated using well-established methods for one-dimensional correlated quantum systems, such as the density-matrix renormalization group. The validity of this approach is investigated using a wire with noninteracting electrons as well as a correlated wire with a Hubbard electron-electron repulsion. The narrow ladder models capture the low-energy physics of wires on semiconducting substrates using at least 3-leg ladders. They accurately reproduce the quasi-one-dimensional excitations of the full three-dimensional model.

This approach can be extended to investigate other features such as electron-phonon coupling, spin-orbit coupling, etc. It is also suitable for comparisons with experiments and first-principles calculations.

**Keywords:** *Nanowires - Strongly Correlated Systems - Lattice Models in Condensed Matter*

## Zusammenfassung

Eindimensionale korrelierte Leiter werden durch die Theorie der Luttinger-Flüssigkeiten beschrieben. In jüngster Zeit wurde von mehreren Systemen von Atomdrähten auf halbleitenden Substraten behauptet sie würden einige der Eigenschaften von Luttinger-Flüssigkeiten besitzen, aber ohne eine Erklärung des Einflusses des Substrats auf die eindimensionalen Elektronen. In dieser Dissertation wird diese Frage behandelt, durch zwei Ansätze zur Modellierung von Draht-Substrat-Systemen.

Das erste Modell besteht aus einem asymmetrischen 2-Bein-Leitersystem, wobei ein Bein durch eine Hubbard-Kette und das andere durch ein eindimensionales Elektronengas beschrieben wird. Die beiden Beine sind durch einen Hüpfterm zwischen nächsten Nachbarn auf beiden Beinen verbunden. Die verschiedenen Phasen, die sich als Funktion der Hubbard-Wechselwirkung und des Hüpfterms bei Halbfüllung ergeben, offenbaren die reichhaltigen physikalischen Strukturen des Modells. Zu diesen Phasen gehören die Luttinger-Flüssigkeit bei sehr schwachem Hüpfterm, der Kondo-Mott-Isolator bei moderatem Hüpfterm oder starker Hubbard-Wechselwirkung und der "Spin-gapped" paramagnetische Mott-Isolator bei mittlerer Stärke der Wechselwirkung und des Hüpfterms. Diese letzte Phase ist ein korrelierter Band-Isolator bei starkem Hüpfterm. Es hat sich gezeigt, dass dieses Modell nicht ausreicht um Draht-Substrat Systeme zu beschreiben, aber es eignet sich als minimales Modell um Koexistenz und "proximity effects" von verschiedenen quasi-langreichweitigen Ordnungen, die in höheren Dimensionen auftreten können zu studieren.

Der zweite Ansatz liefert die erfolgreiche Konstruktion eines geeigneten Modells für Draht-Substrat Systeme. Dabei wird zunächst ein Gittermodell für ein eindimensionalen Quantendraht auf einem dreidimensionalen Substrat konstruiert. Dieses Modell wird mit Hilfe des Lanczos Algorithmus auf ein effektives zweidimensionales Gitter abgebildet und dann durch ein "narrow ladder" Modell genähert, das durch gut etablierte Methoden für eindimensionale korrelierte Quantensysteme, wie die Dichtematrix-Renormierungsgruppe, untersucht werden kann. Um die Gültigkeit dieses Ansatzes zu überprüfen werden ein Draht mit nicht wechselwirkenden Elektronen, sowie ein korrelierter Draht mit Hubbard Elektron-Elektron Abstoßung verwendet. Die "narrow ladder" Modelle zeigen die Niedrigenergie-Physik eines Drahtes auf einem halbleitenden Substrat, wenn mindestens drei Beine verwendet werden. Sie geben dann die quasi-eindimensionalen Anregungen des vollständigen drei-dimensionalen Modells mit hoher Genauigkeit wieder.

Dieser Ansatz kann erweitert werden um andere Eigenschaften wie Elektron-Phonon Kopplung, Spin-Orbit-Kopplung, etc. zu untersuchen. Des Weiteren ist er geeignet für den Vergleich mit Experimenten und "first-principles" Berechnungen.

**Schlagwörter:** *Nanodrähte - Stark korrelierte Systeme - Gittermodelle in der kondensierten Materie*

# Chapter 1

## Introduction

Strictly one-dimensional electron systems have been the subject of extensive theoretical studies for more than 60 years [1]. The main reason of such intensive investigations is that Fermi liquid theory of interacting electrons in three dimensions is not applicable in one dimension. Several features have been predicted for 1D electrons, e.g. the Peierls instability, [2, 3] incommensurate charge and spin density waves, [3] and the dynamical separation of spin and charge excitations [4]. Experimentally, several systems such as Bechgaard salts [5],  $\pi$ -conjugated polymers [6] and others have been classified as quasi-one-dimensional electron systems. The so-called Luttinger liquid theory [4] represents the established theoretical framework for quantum one-dimensional conductors similar to the Fermi liquid theory in three dimensions. A brief review of the Luttinger liquid theory and some experimental realizations are presented in the next section.

### 1.1 1D metals: Theory and experiments

#### Luttinger liquid universality

The concept of Luttinger liquid was introduced by Haldane [7] to generalize rigorously the low energy properties of Tomonaga-Luttinger model for any one-dimensional correlated electron model. These attempts have been motivated by the failure of Landau's Fermi liquid theory to describe the effect of electron correlations in one dimension. For a good review of Luttinger liquids one could take Refs. [7], [4] and [8]. The Tomonaga-Luttinger model is a one-dimensional exactly solvable model with excitations made of noninteracting collective density oscillations which have bosonic nature. Haldane has shown that the low energy excitations of any one-dimensional interacting electron model are similar to the excitations of Tomonaga-Luttinger model, however, with interactions between these bosonic density excitations [7]. These interactions can be eliminated using renormalization techniques. Therefore, the dispersion of these bosonic density excitations is linear in the low energy regime, i.e. close to the Fermi wave vector  $k_F$ . For the one component Luttinger liquid, i.e. interacting spinless fermions, the collective bosonic density excitation is characterized by a sound velocity,  $\nu$ , given by the slope of the dispersion. For the two components Luttinger liquids, i.e. spin- $\frac{1}{2}$  fermions, there are two kinds of bosonic collective density excitations, namely charge (holon) and spin (spinon) density excitations. These two excitations are independent and propagate with different sound velocities  $\nu_c$

and  $\nu_s$  respectively. An other characteristic feature of Luttinger liquids is the power-law decay of correlation functions in long distance and time at  $T = 0$  and  $k_F$ . The exponents of this decay are nonuniversal and determined using the dimensionless Luttinger parameters  $K_\rho$  and  $K_\sigma$  as well as the aforementioned velocities. The local density of states is characterized by power-law decay as a function of energy while approaching the Fermi energy at Fermi wave vector  $k_F$ . Such a power law takes the form of a pseudo-gap. This is applicable to any dynamical response measured with respect to frequency. The exponent depends on the dimensionless parameters  $K_\rho$  and  $K_\sigma$ . However, spectral functions that measure the spectral weight with respect to both momentum and frequency, reveal two peaks for the two-component Luttinger liquid. Each peak corresponds to one of the two components: one to the holon and the other to the spinon. The details of these peaks depend on the details of the two particle coupling[9].

A Luttinger liquid has an instability when the reciprocal lattice wave vector which reflect the lattice periodicity is equal to the nesting wave vector  $4k_F$ . In this case the momentum is not conserved between the scattered electrons. Instead, scattered electrons can transfer momentum to the lattice and get it back. This process is called the umklapp scattering. It leads to a gap opening (at  $T = 0$ ) in the holon excitation when the coupling strength and range are large enough. The multiple of the nesting wave vector  $4k_F$  is constrained also by the commensurate filling of the lattice (half filling, quarter filling and so on). By reducing the filling commensurate ratio, the necessary range of the coupling to open a gap increases. For example, any repulsive interaction is enough to open a gap at half-filling for spin- $\frac{1}{2}$  electrons but for quarter-filling it is necessary to introduce strong enough interaction with at least nearest-neighbor range. The spinon excitations remain gapless. This transition is known as a Mott metal-insulator transition [10, 4] and it is driven by the interaction. Mott insulators and their metal-insulator transition exist also in higher dimensions. However, in one-dimension they can be described within the framework of Luttinger liquid theory [4]. In one dimension, Mott transition is a Kosterlitz-Thouless transition characterized by discontinuous jump in the  $K_\rho$  value from a critical value  $K_c$  at the transition to zero in the Mott insulating phase. Furthermore, it affects charge density correlations as well as the transport properties at  $T = 0$ . The density correlations decay exponentially in the Mott phase due to the gap opening. On the other hand the optical conductivity for all the frequency range within the Mott gap is zero. For higher frequencies the optical conductivity is characterized by a peak which decays as a power-law.

Within the variety of models which are described by the Luttinger liquid theory there are some that can be solved exactly using the so called Bethe ansatz method such as the 1D Hubbard[11] and XXZ[12] models.

## Coupled Luttinger liquids

Luttinger Liquid properties are reported in bulk anisotropic materials. These materials are described as a set of one-dimensional correlated-electron chains. Therefore, it is important to introduce inter-one-dimensional coupling between Luttinger liquids to investigate how it can affect the properties of Luttinger liquids and hence to enable comparisons with experiments. A good review of coupled Luttinger liquids can be found in Ref. [4]. Nevertheless, the realization of Luttinger liquids is not restricted to anisotropic bulk sys-



tems, there are other experimental realizations such as single-wall carbon nanotubes, edge states in quantum Hall effect, metallic nanowires on semiconducting substrates, etc.

The motivation of this thesis is the search for appropriate models to describe the correlation effects in metallic nanowires deposited on semiconducting substrates. These materials can not be represented as anisotropic bulk materials but they constitute a coupling between one-dimensional chains and a reservoir and they will be discussed in the next section. However, it is relevant to discuss briefly the effect of such 2 and/or three dimensional coupling on Luttinger liquids.

The inter-chain coupling between Luttinger liquids can be classified between direct interaction coupling, e.g. density-density or spin-spin couplings, and the single-particle tunneling between chains [4]. The former could be approximated using mean field approximation due to the existence of classical limits for spin and density operators which is valid at least for coupling between infinite number of chains. This kind of coupling derives the system to an ordered state and hence destroy the Luttinger liquids. It should be emphasized that this discussion is valid if all other energy scales are set to zero. The single-particle coupling does not have a classical limit due to its fermionic nature making its treatment more complicated. It is appropriate to start the treatment of such a system of coupled chains by introducing a small single-particle coupling comparing to the intra-chains energy scale. By neglecting the electron-electron interactions and considering only a two-dimensional tight-binding lattice the energy dispersion can take the form

$$\epsilon(k_{\parallel}, k_{\perp}) = -2t_{\parallel} \cos(k_{\parallel}a) - 2t_{\perp} \cos(k_{\perp}b) \quad (1.1)$$

where  $t_{\parallel}$  and  $t_{\perp}$  are the parallel and perpendicular hopping terms,  $a$  and  $b$  are the lattice constants in the parallel and perpendicular directions, respectively. The dispersion in Fig. 1.1 shows undulation in the  $k_{\perp}$  direction for  $t_{\perp} \ll t_{\parallel}$  which become a straight line for  $t_{\perp} = 0$ . If an energy scale, such as the thermal energy at finite temperature, is larger than the band width of the undulation then the system is effectively indistinguishable from uncoupled 1D chains. By reducing this energy scale smaller than the undulation width the system will recover the 2D or 3D features. This describes the dimensional crossover in the noninteracting case with an onset of the order of the perpendicular hopping. Similar behavior is expected for the density-density and spin-spin couplings. From the other side, the presence of interaction makes the treatment of the inter-chain hopping harder due to the deference between the bosonic excitations existing in the chain and the fermionic nature of the hopping. In general, the one-dimensional nature will be preserved for energy scales smaller than the onset in the noninteracting case. However, in such smaller scales there are other relevant tunneling processes which could take place such as density-density, spin-spin couplings and pair hopping which derive the system to an ordered state (at zero temperature). Thus, the problem will depend on whether the dimensional crossover takes place before the system becomes in ordered state or not. If the dimensional crossover takes place first then the system will be a two-dimensional system derived from a non-Fermi liquid phase. The other case will introduce an ordered phase and destroy the Luttinger liquid features. If the coupled infinite chains are made of Mott insulating chains the inter-chain coupling will require enough energy to overcome the chain gap. Once the inter-chain coupling reaches this point the electrons are deconfined from single chains and they turn the coupled chains into a metallic 2 or 3 dimensional system. Thus, this effect is named the deconfinement transition. In the confined electron phase

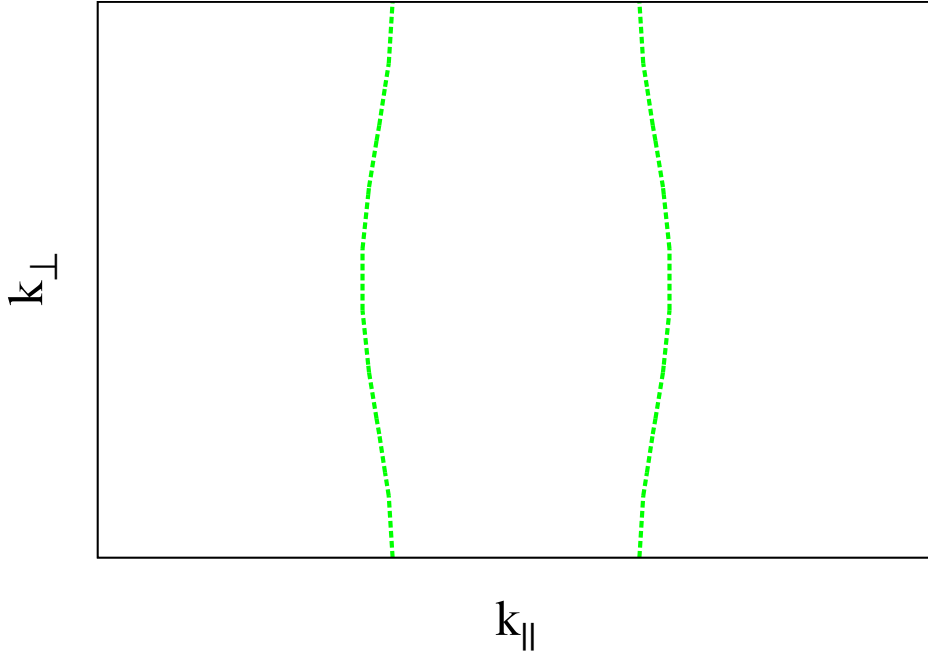


Figure 1.1: Dispersion of two-dimensional tight-binding lattice with weak coupling in the  $y$ -direction. This dispersion demonstrates the undulation of weakly coupled chains of noninteracting electrons.

the system undergoes a crossover from Mott insulator at low temperatures to Luttinger liquid at high temperatures. In the deconfined phase the system experience dimensional crossover between Luttinger liquid at high temperature and 2 or 3 dimensional metallic phase.

An other approach to investigate the coupled interacting chains is to consider just systems of few coupled chains. This has stimulated lots of investigations which are too large to be all covered here. However, some main findings could be represented by spin- $\frac{1}{2}$  ladder systems. For instance, a strong ferromagnetic coupling between legs restricts each rung in a polarized state with spin  $S = n/2$  where  $n$  is the number of legs. If this system of rungs are then coupled with intra-chain antiferromagnetic coupling, the ladder system becomes equivalent to an antiferromagnetic spin chain with  $S = n/2$ . According to Haldane [13], any integer spin chain has gapped excitations from the ground state while any half integer spin chain has gapless excitations from the ground state. Therefore, these spin-ladder systems have ground states with gap to excitations if they constructed from even number of legs while the have gapless excitations from ground states if they are constructed from odd number of legs. An other example is for spin- $\frac{1}{2}$  ladders with strong inter-chain antiferromagnetic coupling. By taking a two-leg spin-ladder, each rung has a singlet ground state with a gap to triplet excitation. Then, series of singlet rungs are formed by the intra-chain coupling without changing the gapped nature of the ground

state. This picture changes if the spin-ladder system contains three legs. In this case, the strong antiferromagnetic inter-chain coupling can not make a singlet out of three spin- $\frac{1}{2}$  sites. Therefore, each rung represents a spin- $\frac{1}{2}$  site and the antiferromagnetic intra-chain coupling construct a 3-leg spin-ladder system which is equivalent to a spin- $\frac{1}{2}$  chain. Thus, the same Haldane "conjecture" can be applied for such ladder systems. This picture is also preserved to in the weak coupling limit between legs, thanks to the bosonization analysis [4]. The behavior for  $n \rightarrow \infty$  remains an open problem. The spin- $\frac{1}{2}$  fermion ladders consist of Mott insulating chains behave similar to the spin ladders discussed before but with gapped charge excitations. The doped spin- $\frac{1}{2}$  fermion ladders exhibit rich physics connected to pairing in high-temperature superconductors and other phases which will not be discussed here [14, 15].

## Experiments

The first experimental realization of Luttinger liquids has been observed in anisotropic materials of organic conductors [16]. These materials can be modeled by tight binding models with hopping term in one direction larger by one and two order of magnitudes than the hopping terms in the other two dimensions respectively. This means that if the dynamical properties of these materials (e.g. optical response) are probed for energy scale larger than the smallest hopping terms but smaller than the largest one they behave as one-dimensional electrons. In such a case, they reveal hallmarks of Luttinger liquid namely the power-law decay in the dynamical response. Similar behavior is applicable by setting the thermal energy scale to be larger than the smallest hopping [17]. Other kind of methods such as scanning tunneling microscopy and spectroscopy (STM/S) are used to investigate the power-law decay. Other materials such as purple bronze and carbon nanotubes as well as systems of cold atoms are reported to show Luttinger liquid properties (see Ref. [18] and references therein).

The spin-charge separation feature is much harder to observe in experiments. The photoemission experiments have been used to observe it [19] by revealing the two different excitation dispersions that correspond to holons and spinons. However, this way lead to controversial interpretations. One source for this controversy come from the non-universality of these holon and spinon dispersions [20], i.e. they are model dependent. An other way to investigate spin-charge separation is done by tunneling between two nanowires [21, 22] controlled by gate voltage and magnetic field to adjust the energy momentum differences, respectively, between the two quantum wires. The tunneling spectrum reveals different branches which are assigned to independent spin and charge modes. In reality these experimental systems are not only pure one-dimensional systems, i.e. there is a coupling to other dimension, except for cold atoms prepared as 1D systems. For instance as it was shown for coupled Luttinger liquids, the anisotropic bulk systems have been described using coupling between one-dimensional electron systems. The strength of such coupling in addition to electron-electron Coulomb interactions play an essential role in the presence of Luttinger liquid features [1, 4, 5].

Recently, experimental realizations of 1D properties on reconstructions of metallic nanowires on semiconducting substrates have been reported. Nevertheless, these systems lack theoretical understanding of the apparent Luttinger liquid features due to poor theoretical knowledge about the influence of the wire-substrate hybridization on one-

dimensional features. The understanding of this influence gives the motivation for this thesis. Therefore, a separate discussion about experimental realizations of some reconstructions of metallic nanowires on semiconducting substrates which have been reported to host Luttinger liquid hallmarks will be presented in the next section.

## 1.2 1D metal on a semiconducting substrate: experimental realization

### Pt/Ge(001)

A self organized Pt/Ge(001) structure at room temperature has been reported by Gurlu et al. [23]. Using scanning tunneling microscopy/spectroscopy (STM/S) they were able to show that this structure consists of 1D nanowires of 0.4 nm thickness, 1.6 nm interwire distance and about 380 nm length. The nanowires are defect-free and cover an area on the Ge(001) surface called  $\beta$ -terrace. Other parts of the Ge(001) surface called  $\alpha$ -terrace are not covered by nanowires. Gurlu et al. [23] proposed a structural model for  $\beta$ -terraces called quasi-dimer-rows where one of the Ge atoms of every second dimer is replaced by Pt atom along the Ge(001) dimer rows. The nanowires, according to their model, are metallic and formed from Pt dimers on the first layer in between the quasi-dimer-rows.

In an other report [24], N. Oncil. et al. used STS measurements to show confined states between the nanowires. They successfully used a model of quantum particles trapped on a finite well to interpret the results. These confined states are found only at low temperature (77 K).

On the other hand, it has been shown by ab-initio calculations based on density functional theory (DFT) that the proposed model of top Pt atoms does not reproduce the observed STM images. However, a model proposed by A. A. Stekolnikov et al. [25] shows a good agreement between the calculated and measured STM images in the case of 0.25 ML Pt coverage proposed by Gurlu et al. [23]. This model called the tetramer-dimer-chain (TDC) model and characterized by top chains of Ge pairs connected to fourfold Pt atoms on one side of the ridge and Ge tetramer atoms on the other side.

However, according to D. Vanpoucke and G. Brocks[26] this model is not stable energetically due to its larger formation energy compared to the bare Ge(001) surface. Therefore, they proposed an other model based on larger Pt coverage. The main feature of this model is the nanowires consisting of Ge dimers while mixed Pt-Ge dimer rows are lined in the troughs.

Concerning the 1D peculiarity, there is a consensus about the metallic phase of the Pt/Ge(001) nanowires at room temperature according to my knowledge. However, there is a debate about a Peierls instability at low temperature. A. van Houselt et al. [27] reported that the system undergoes a Peierls transition at low temperature (about 4.7 K) but they assume that the nanowires consist of Pt chains on the first layer of the Pt/Ge(001) surface which contradicts the much more stable model proposed by D. Vanpoucke and G. Brocks [26] or even the TDC model.

On the other hand, I. Mochizuki et al. [28] performed a study using STM, reflection high-energy positron diffraction (RHEPD) and angle-resolved photoemission spectroscopy (ARPES) supporting D. Vanpoucke and G. Brocks [26] model. They rule out

Peierls instability due to difference in the value of the nesting vector between the measured and calculated ones, although they confirmed structural displacement of the topmost Ge dimers.

In an other investigation, K. Yaji et al. [29] also rule out Peierls instability and show, using ARPES, two metallic bands, one has 2D feature and one shows 1D feature and both of them are in each side of  $\bar{\Gamma}$ . The 1D metallic band is shown on a density plot of spectral function against  $k_x$  and  $k_y$  axis by straight line along  $k_y$  with very weak undulation around this straight line direction (1% of the surface Brillouin zone size). They confirmed the one-dimensionality by recording the binding energy against  $k_x$  at different points of  $k_y$  and showing the same parabolic shape within 0.2 eV below Fermi level. They excluded a Peierls instability due to the difference between Fermi wave vectors of both metallic bands and the nesting vector corresponding to the observed structural transition. They integrated the ARPES intensity over  $k_x$  for the 1D band and plot it against the binding energy but they did not find any suppression around the Fermi energy. Therefore, they concluded that there is no realization of Luttinger liquid in this system.

Nevertheless, these findings of noninteracting one-dimensional electrons have been verified in an other study by K. Yaji et. al. [30] where they found evidences for Luttinger liquid power-law decay of density of states in the one-dimensional band. The power-law decay has been revealed using much more precise ARPES measurements. They estimated a power-law exponent  $\alpha = 0.25$  much smaller than those found in carbon nanotubes or purple bronze indicating weaker electron-electron interactions. Despite that, they did not exclude the possibility of disorder-driven power-law decay in theses ARPES results instead of Luttinger liquid. Moreover, they found an other band showing undulation of weakly coupled chains and spin-splitting due to Rashba effect. This additional band is metallic and they did not found evidence for a Peierls transition despite the structural transition found in the system. They stated that the current structural models are not sufficient to describe their experimental results.

## Au/Ge(001)

An other self-organized metallic wire on G(001) substrate is the Au/Ge(001) reconstruction. This system has been reported by J. Wang et al. [31] using STM experiments at room temperature. With estimated coverage of 0.5 ML, they showed images of several hundreds nanometers long Au-induced chains. This reconstruction has a metallic behavior on the nanowires according to possibility of using on-chain bias down to 0.2 V which is not possible on the neighbor Ge patches. However, this reconstruction differs from the Pt/Ge(001) by a high defect density. Nevertheless, by increasing the coverage to 1.5 ML they observed a fully covered surface with well ordered chains. From a  $(4 \times 2)$  LEED pattern, they proposed a model of Au-Au dimers on the top level parallel to Au-Ge dimers on the second level.

J. Schäfer et al. [16] performed an other STM investigation for the same system. They reported 0.5 ML coverage for several 1000 Å length nanowires and a different LEED pattern of  $c(8 \times 2)$ . They emphasized the 1D features by showing a spread of metallic charge along the nanowires with a one atom width. Furthermore, by scanning laterally to the nanowires the tunneling conductivity decline considerably. They also performed an ARPES investigation where a 1D band referred to the nanowires is shown.

However, these findings were controversial as they are seen from the comment of A. van Houselt et al. [32] where they rule out the one-dimensionality of the Au/Ge(001) reconstruction.

A structural model called giant missing row (GMR) reconstruction is proposed by A. van Houselt et al. [33] based on STM investigations. They reported 0.2-0.3 ML coverage at room temperature with a similar structure to J. Wang et al. [31] proposal with much deeper troughs. This model consists of well ordered (111) faceted nanogrooves decorated with Au atoms into  $\sqrt{3} \times \sqrt{3}R30^\circ$  pattern. The top of the ridges consist of buckled Ge dimers[33].

The disputation about the one-dimensionality has been raised again by K. Nakatsuji et al. [34]. They did ARPES accompanied with STM and LEED investigations to address the Au/Ge(001) reconstruction. The LEED measurements is done at 130 K while ARPES and STM experiments are done at room temperature. They estimated 1.1-1.2 ML coverage and reported  $8\times$  periodicity both parallel and perpendicular to the chains with dispersion along  $\langle 110 \rangle$  direction showing metallic surface state consistent with  $8\times$  periodicity. The metallic bands close to Fermi surface show ellipsoidal form. They concluded that an anisotropic 2D metallic surface is the reason for these observations.

From the other side, S. Meyer et al[35] emphasized on the one-dimensionality of the Au/Ge(001) reconstruction and criticized K. Nakatsuji et al. [34] for not using enough accurate results on their report of anisotropy. They also performed ARPES at 15 K accompanied with STM and LEED down to 10 K. They observed a Fermi surface with parallel lines and two electron pockets on the two sides of  $\bar{\Gamma}$ . They rule out Peierls or CDW scenarios and interpreted these ARPES results as a 1D metallic electron band. In this study, they estimated 0.15 band filling for each pocket.

A DFT investigation have been performed by S. Sauer et al. [36] for the Au/Ge(001) reconstruction. They did not find a model with lowest surface formation energy and good agreement with STM images. The GMR model is found to have a good agreement with STM details, however it has a quite large surface formation energy. Furthermore, 1D metallic band is found in the GMR model but with weaker band dispersion and larger band filling compared to experiments reported by S. Meyer et al[35]. They reported a modification of the GMR model to the so called ATSGR model which reduces the formation energy. This model is described by rearrangement of Ge ridges, formation of Au trimers on the side facets and additional Ge atoms in the trenches. An other model showed by them, called the bridging dimer row model, has low surface formation energy and produces good STM image but it can not explain the differences between filled and empty states in the experiments. This model described by two dimer rows bridged by perpendicular dimers with removing every second dimer row in the clean Ge(001).

A feature of Luttinger liquids, namely the power law dependence of local DOS in the vicinity of Fermi points, has been reported by C. Blumenstein et al. [37]. They measured STM and STS for an Au/Ge(001) reconstruction with estimated 0.5 ML coverage at 4.7 K. They did also ARPES measurements for the same system at 10 K. The differential tunneling conductivity (DTC) which measured in STS has been recorded which corresponds to the on-wire local DOS (LDOS). It shows a power law decay of the LDOS around Fermi energy with a non-universal exponent  $\alpha = 0.53$ . They confirmed these results by integrating the 1D metallic band found by ARPES over the wave vector  $k$ . The same decay for the integrated intensity in the vicinity of Fermi energy with the same exponent

is observed. They measured the DTC for several temperatures and plotted them against renormalized energy scale  $eV/k_B T$  to find a power law dependence with the same exponent. The effect of disorders and dynamical Coulomb blockade are ruled out as reasons for such observations. These observations agree well with Luttinger liquid predictions from which they estimated the charge stiffness constant  $K_\rho = 0.26$  for this system.

Nevertheless, K. Nakatsuji et. al. [38] reported ARPES study that show stronger Au-band dispersion perpendicular to the wires than parallel to them.

Moreover, J. Park et al. [39] opposed the report of Luttinger liquid to be found on the Au/Ge(001) reconstruction. They used STM and STS investigations done at 78 and 5.5 K and estimated 0.75 ML coverage. The analysis of their results led to a conclusion of 2D electronic state near Fermi energy and they refer the Luttinger liquid behavior seen by C. Blumenstein et al. [37] to be a result of disorders.

Furthermore, an other study by N. de Jong et. al. [40] emphasized the 2D nature of the Au/Ge(001) reconstruction and supported the counterintuitive finding of stronger Au-band dispersion perpendicular to the wires. They performed experimental and theoretical investigations using ARPES, STM, STS, LEED and analysis of a minimal tight-binding model.

Addressing the debate of the dimensionality, an other recent study by K. Seino and F. Bechstedt[41] focused on structural models for the Au/Ge(001) reconstruction. They proposed several models derived from the ATSGR model with large coverage ranging between 1.25 and 1.75 ML. They reported that, due to similar formation energy, different structures may be realized by different experimental research groups. They were able to explain the STM experiments with lower formation energy than ATSGR model. However, although the electron and hole wave functions are found to distribute along the wire ridges and/or sides, there are weak band dispersions perpendicular to the wire direction which depend on the wave function overlap between the adjacent unit cells.

Using DFT method, K. Seino et. al. [42] studied the stability of various structural models while changing the temperature. They found that the surface structure is sensitive to temperature changing. They showed that some structural models that are compatible with experimental results stabilize by rising the temperature. On the other hand, some stable models at 0 K lose their stability by rising the temperature.

L. Dudy et. al. [43] published a review on the Au/Ge(001) reconstruction. They highlighted the difficulty of coverage estimation. They also supported the counterintuitive finding that the Au-band dispersions are more pronounced perpendicular to wires direction K. Nakatsuji et. al. [38] and de Jong et. al. [40].

## **Bi/InSb(001)**

A reconstruction of Bi/InSb(001) has been reported to show a power law dependence of LDOS in the vicinity of Fermi points by Y. Ohtsubo [44]. They concluded that a surface Luttinger liquid exists in this system. They prepared a Bi/InSb(001) reconstruction by 3 ML Bi evaporation on clean InSb(001) surface. They measured the band structure using ARPES at room temperature and reported a linear Fermi contour along  $k_y$  indicating one 1D metallic state. A measurement along  $k_x$  at 8 K has been done for the metallic band revealing a parabolic shape with minimum at  $k_x = 0 \text{ \AA}^{-1}$ . They integrated the spectral intensity over  $k_x$  for  $k_y = 0.25 \pm 0.05 \text{ \AA}^{-1}$  at 35 K and show a power law scaling

of the intensity below 0.1 eV. The power law exponent was  $0.65 \pm 0.05$ . They found the same scaling of the intensity at Fermi energy as a function of temperature with a power law exponent  $0.71 \pm 0.1$ . They measured the momentum distribution curves along  $k_x$  for several binding energy values below and above Fermi energy. They got the peak distribution position at each binding energy and estimated the Fermi wave vector to be  $0.05 \pm 0.02 \text{ \AA}^{-1}$ . By this way they reported the ability to scan above and below Fermi energy and showed suppression of intensity around Fermi energy without gap opening or breaking discontinuity. Nevertheless, there are no detail about the formation of nanowires neither from STM/S measurements nor DFT calculations.

In an other publication, Y. Ohtsubo [45] showed possible spin-charge separation in the Bi/InSb(001) reconstruction using ARPES measurements. They reported two energy distribution curves with separate spectral features. The two features disperse with different Fermi velocities. One dispersive feature could be assigned to charge excitation and the other to spin excitation. Nevertheless, they did not exclude the possibility of two surface states causing these two features but without affecting the validity of the Luttinger liquid power-law decay in this system.

### 1.3 Theoretical approaches for a 1D metal on a substrate

The existence of Luttinger liquid properties in the three systems discussed before is highly debated. The actual structures of the Pt/Ge(001) Au/Ge(001) systems are not, yet, settled. However, much more consensus is reached for the Pt/Ge(001) system than for the Au/Ge(001). The Bi/InSb(001) system lacks systematic structural investigations. Moreover, if we agree for the moment that these systems show 1D correlated features, the understanding of the impact of the substrate is entirely unknown. Therefore, more general new approaches are needed to fill this gap. Solving a model for a metallic wire on semiconducting substrate including complex structure and full electron interactions is not possible with current analytical or numerical methods. As it is discussed before, Luttinger liquids emerge from electron-electron interaction in 1D metals which means that mean-field approximations can not give correct solutions. However, lattice models, such as the 1D Hubbard model, have been used widely to describe correlated electrons qualitatively in 1D including Luttinger liquids[4, 11]. These models are solved by some analytical methods such as bosonization or numerical methods such as density matrix renormalization group (DMRG) [4, 46].

For this thesis the 1D Hubbard model is adopted to describe a 1D correlated wire accompanied with two different approaches to describe the substrate. The first approach considers a 1D tight binding chain as a substrate which is coupled to the 1D Hubbard chain using single-particle hopping. By this way the model will be an asymmetric 2-leg ladder [47]. This model lacks systematic investigations, which is not the case for similar asymmetric ladder models [14, 15]. Only investigation in Ref. [48] has been found by the thesis author. The second approach is to describe the substrate using a tight binding 3D square lattice with a hybridization using a single-particle hopping to the 1D Hubbard chain. However, this model is still difficult to solve using state-of-the-art methods in 1D such as DMRG due to its three dimensionality. Therefore, a mapping from 3D to 2D



ladder system is proposed [49]. Then, an approximation by taking just few legs out of the 2D ladder to form a quasi-one-dimensional system is investigated to understand the possibilities and limitations of this approximation [49, 50]. The main method used for these two approaches is DMRG which is briefly discussed in the following section.

## 1.4 Density matrix renormalization group: a numerical method for 1D systems

DMRG is a numerical method developed by Steven White [51] while trying to overcome the failure of the numerical renormalization group method in solving 1D electron systems in real-space lattice. DMRG represents, probably, the best numerical method to treat quasi-1D correlated electrons with short range interactions. Many extensions have been developed which make it competitive with state-of-the-art methods for correlated electrons in fields such as dynamical response, quantum chemistry, 2D-electron systems, etc. A major breakthrough on DMRG came from the possibility to represent the ground state of 1D electron systems with local interaction using so called matrix product states (MPS). It has been shown that DMRG gives an accurate approximation to the ground state in the MPS form for such 1D system [52]. This has led to large progress in time evolution, finite temperature and other problems as well as establishing quantum information and other fields. These advancements lead to the large effort in developing methods based on the more general class of MPS, the so called tensor network states (TNS)[53].

### Wave function approximation using reduced density matrix

The description of DMRG starts by considering a quantum lattice in which the aim is to find any quantum mechanical state (usually the ground state). The local basis of site  $l$  in this quantum lattice is given by a set  $\{|\sigma_l\rangle; \sigma_l = 1, \dots, d\}$  of orthonormal basis where  $d$  is the dimension of the local basis set. If such a quantum lattice has a total number of sites  $L$ , then, a complete many-body basis set of the full lattice Hilbert space is given by the tensor product of the local basis such that  $\{ |(\sigma_1, \dots, \sigma_L)\rangle = |\sigma_1\rangle \otimes \dots \otimes |\sigma_L\rangle; \sigma_l = 1, \dots, d; l = 1, \dots, L\}$ . The dimension  $d$  of the local basis is chosen to be equal for each site  $l$ , and hence, the dimension of the full lattice Hilbert space  $\mathcal{D}_L$  grows exponentially with the total number of sites, i.e.  $\mathcal{D}_L = d^L$ . Any pure quantum mechanical state  $|\psi\rangle$  at  $T = 0$  of such a lattice can be expanded using the complete many-body basis set as

$$|\psi\rangle = \sum_{(\sigma_1, \dots, \sigma_L)} C_{(\sigma_1, \dots, \sigma_L)} |(\sigma_1, \dots, \sigma_L)\rangle \quad (1.2)$$

where the sum is running over all possible configurations of the many-body basis states and  $|\psi\rangle$  is assumed to be normalized. However, the determination of such a state, e.g. by the full diagonalization of the lattice Hamiltonian, is not possible for large number of sites  $L$  due to the very large dimension of the Hilbert space. This exponential growth of Hilbert space is a major problem for computational calculations of strongly correlated electron systems. DMRG provides an efficient way to reduce the size of basis states in order to give a good approximation for the state  $|\psi\rangle$  and observables measured for it.

To illustrate the ideas behind DMRG one should introduce a bipartition of the full lattice into two parts  $A$  (the system block in DMRG terminology) with size  $L_A$  and  $B$  (the environment block in DMRG terminology) with size  $L_B = L - L_A$ . The full system-environment lattice is denoted the super-block in DMRG terminology. Thus, two sets of many-body basis states  $\{|a\rangle\}$  and  $\{|b\rangle\}$  are defined for  $A$  and  $B$ , respectively, such that  $\{|a\rangle = |(\sigma_1, \dots, \sigma_{L_A})\rangle = |\sigma_1\rangle \otimes \dots \otimes |\sigma_{L_A}\rangle; \sigma_l = 1, \dots, d; l = 1, \dots, L_A\}$  with dimension  $\mathcal{D}_A$  and  $\{|b\rangle = |(\sigma_{L_A+1}, \dots, \sigma_L)\rangle = |\sigma_{L_A+1}\rangle \otimes \dots \otimes |\sigma_L\rangle; \sigma_l = 1, \dots, d; l = L_A + 1, \dots, L\}$  with dimension  $\mathcal{D}_B$ . Thus,  $|\psi\rangle$  can be expressed in terms of  $\{|a\rangle\}$  and  $\{|b\rangle\}$  as

$$|\psi\rangle = \sum_{a,b} \psi_{a,b} |a\rangle \otimes |b\rangle. \quad (1.3)$$

while assuming  $\langle\psi|\psi\rangle = 1$ . The reduced density matrix (RDM) of the system block is defined by tracing out the environment states  $\{|b\rangle\}$  such that

$$\rho_{aa'} = \sum_b \psi_{a,b} \psi_{a',b}^* \quad (1.4)$$

where

$$\psi_{a,b} = \langle ab|\psi\rangle \quad (1.5)$$

which give the elements of the operator  $\hat{\rho}$  that is subjected to the normalization condition  $\text{Tr}\hat{\rho} = 1$ . Thus, any observable  $\hat{O}$  can be measured on the system block  $A$  using the relation

$$\langle\psi|\hat{O}|\psi\rangle = \text{Tr}\hat{\rho}\hat{O} = \sum_{\alpha} \omega_{\alpha} \langle u^{\alpha}|\hat{O}|u^{\alpha}\rangle \quad (1.6)$$

where  $\omega_{\alpha}$  and  $|u^{\alpha}\rangle$  are the eigenvalues and eigenstates of  $\hat{\rho}$  with  $\alpha = 1, \dots, \mathcal{D}_A$ . Due to the normalization condition of  $\hat{\rho}$  its eigenvalues obey the relation  $\sum_{\alpha}^{\mathcal{D}_A} \omega_{\alpha} = 1$  and each  $\omega_{\alpha}$  gives the weight of the correspondent eigenvalue  $|u^{\alpha}\rangle$ .

The basis states of the system block can be expanded using the RDM eigenstates, i.e.  $|a\rangle = \sum_{\alpha} C_{\alpha,a} |u^{\alpha}\rangle$ . This will allow to write Eq.(1.3) using the RDM eigenstates in the form

$$|\psi\rangle = \sum_b \sum_{\alpha} C_{\alpha,b} |u^{\alpha}\rangle \otimes |b\rangle. \quad (1.7)$$

Notice that  $\langle u^{\alpha}|u^{\alpha'}\rangle = \delta_{\alpha,\alpha'}$ . Then, using the basis states of the environment block, one can define states  $|\nu^{\alpha}\rangle = \sum_b C_{\alpha,b} |b\rangle$  which allow to write Eq.(1.3) in a much more compact form, i.e.

$$|\psi\rangle = \sum_{\alpha} C_{\alpha} |u^{\alpha}\rangle \otimes |\nu^{\alpha}\rangle \quad (1.8)$$

where  $|\nu^{\alpha}\rangle$  are constrained by normalization condition, i.e.  $\langle\nu^{\alpha}|\nu^{\alpha}\rangle = 1$ . This offer a way to reduce the number of the required coefficients to expand  $|\psi\rangle$  in the bipartite super-block to be equal to the number of the system block basis states.

Moreover, if most of the total weight is concentrated only in limited number  $m < \mathcal{D}_A$  of the density matrix eigenstates, the quantum mechanical state  $|\psi\rangle$  can be represented with a good approximation by the expansion

$$|\psi'\rangle = \sum_{\alpha}^m C_{\alpha} |u^{\alpha}\rangle \otimes |\nu^{\alpha}\rangle \quad (1.9)$$

Hence, a good approximation of the measurement of the observable  $\hat{O}$  can be done using the same limited number of RDM eigenstates, i.e.

$$\langle \psi' | \hat{O} | \psi' \rangle = \sum_{\alpha}^m \omega_{\alpha} \langle u^{\alpha} | \hat{O} | u^{\alpha} \rangle. \quad (1.10)$$

Thus, an estimation of the error  $\epsilon_{\rho}$  due to the truncation of the RDM eigenstates, i.e. the truncation error, on both  $|\psi\rangle$  and the measurement of the observable  $\hat{O}$  can be done using

$$\epsilon_{\rho} = 1 - \sum_{\alpha=1}^m \omega_{\alpha} \quad (1.11)$$

Therefore, by constructing and diagonalizing the RDM in Eq.(1.4) one can estimate the accuracy of the approximation on  $|\psi\rangle$  and the measurements done using it.

The problem can be formulated, in an other way, as a minimization problem of

$$\epsilon_{\rho} = \| |\psi\rangle - |\psi'\rangle \|^2 \quad (1.12)$$

by varying over all  $C_{\alpha}$ ,  $|u^{\alpha}\rangle$  and  $|\nu^{\alpha}\rangle$ . For this purpose,  $|u^{\alpha}\rangle$  can be expanded using the basis states of the system block, i.e.  $|u^{\alpha}\rangle = \sum_a c_a^{\alpha} |a\rangle$  and  $|\nu^{\alpha}\rangle$  can be expanded using the basis states of the environment block, i.e.  $|\nu^{\alpha}\rangle = \sum_b c_b^{\alpha} |b\rangle$ . Thus, the minimization problem of  $\epsilon_{\rho}$  becomes

$$\epsilon_{\rho} = \sum_{a,b} \left( \psi_{a,b} - \sum_{\alpha=1}^m C_{\alpha} c_a^{\alpha} c_b^{\alpha} \right)^2 \quad (1.13)$$

by minimizing over all  $C_{\alpha}$ ,  $c_a^{\alpha}$  and  $c_b^{\alpha}$  for a given number  $m$ .

An other way to handle the expansion in Eq.(1.3) can be done using the so called singular value decomposition (SVD). SVD is a useful tool in the description of DMRG theory and its MPS formulation. It states that for any rectangular matrix  $\Psi$  that has the dimension  $(\mathcal{D}_A \times \mathcal{D}_B)$  there is a possibility to write it in the form

$$\Psi = USV^{\dagger}. \quad (1.14)$$

Here  $U$  has the dimension  $(\mathcal{D}_A \times \min(\mathcal{D}_A, \mathcal{D}_B))$  with orthonormal columns that fulfill the relation  $U^{\dagger}U = I$ . For  $\mathcal{D}_A \leq \mathcal{D}_B$  this satisfies  $UU^{\dagger} = I$  as well, i.e. it is a unitary matrix.  $S$  is a diagonal matrix with the dimension  $(\min(\mathcal{D}_A, \mathcal{D}_B) \times \min(\mathcal{D}_A, \mathcal{D}_B))$ . The non-negative diagonal values are called the singular values.  $V^{\dagger}$  has the dimension  $(\min(\mathcal{D}_A, \mathcal{D}_B) \times \mathcal{D}_B)$  with orthonormal rows that fulfill the relation  $V^{\dagger}V = I$  and for  $\mathcal{D}_B \leq \mathcal{D}_A$  this also satisfies  $VV^{\dagger} = I$ .

For the current case one can choose  $U$  with size  $\mathcal{D}_A \times \mathcal{D}_A$  which gives entries  $c_a^{\alpha}$ ,  $V$  with size  $\mathcal{D}_B \times \mathcal{D}_A$  which gives entries  $c_b^{\alpha}$  and  $D$  is a diagonal matrix with size  $\mathcal{D}_A \times \mathcal{D}_A$  which gives entries  $C_{\alpha}$ . This decomposition gives  $\psi_{a,b}$  in a similar form as  $\sum_{\alpha=1}^m C_{\alpha} c_a^{\alpha} c_b^{\alpha}$  in Eq.(1.13). One can see from Eq.(1.4) that  $\hat{\rho}$  can be diagonalized as

$$U \hat{\rho} U^{\dagger} = D^2 \quad (1.15)$$

which gives the eigenvalues of the RDM by the relation  $\sqrt{\omega_{\alpha}} = C_{\alpha}$  and, hence, the truncation error is obtained according to Eq.(1.11).

The SVD confirms that the required number of basis states to represent the quantum mechanical state  $|\psi\rangle$ , as in Eq. (1.3), can be reduced significantly using the eigenstates of the reduced density matrix and then can be approximated by considering only those states with the largest weights. Nevertheless, this efficient representation needs the knowledge of  $|\psi\rangle$  a priori which seems that nothing has been gained for systems with large number of sites. However, DMRG provides efficient ways to construct Eq. (1.9) which will be described later. From the other side, Eq. (1.9) gives the connection between such a representation and the entanglement through the so called Schmidt decomposition which will be described next.

## Reduced density matrix and entanglement

Entanglement is a purely quantum feature which implies that a quantum state can not be written as a simple product of its constituent states. The entanglement for a bipartite system-environment lattice (the super-block) described above can be studied by representing the state  $|\psi\rangle$  using the so called Schmidt decomposition. The form of Schmidt decomposition is equivalent to represent  $|\psi\rangle$  in the form of Eq.(1.9) but by summing up to the total number  $\mathcal{D}_{\text{Schmidt}}$  of all non-zero values  $\sqrt{\omega_\alpha}$ , i.e.

$$|\psi\rangle = \sum_{\alpha}^{\mathcal{D}_{\text{Schmidt}}} \sqrt{\omega_\alpha} |u^\alpha\rangle \otimes |\nu^\alpha\rangle. \quad (1.16)$$

where  $\mathcal{D}_{\text{Schmidt}} \leq \mathcal{D}_A$ .

One can observe that the total number of coefficients  $\psi_{a,b}$  is reduced to the number of Schmidt non-zero coefficients  $\mathcal{D}_{\text{Schmidt}} \leq \min(\mathcal{D}_A, \mathcal{D}_B)$ . From the quantum information theory one can use the eigenvalue spectrum of the RDM to calculate an entanglement measure, the so-called von Neumann entropy

$$S = -\text{Tr}(\hat{\rho} \ln \hat{\rho}) = - \sum_{\alpha=1}^{\mathcal{D}_{\text{Schmidt}}} \omega_\alpha \ln(\omega_\alpha). \quad (1.17)$$

Clearly, for an approximated state such as in Eq.(1.9) the smaller the truncation error  $\epsilon_\rho$  is the more  $|\psi'\rangle$  preserves the entanglement. In general, quantum information theory provides information about the entanglement scaling which can be used to estimate the possibility for efficient approximation of  $|\psi\rangle$ . For a bipartite super-block in thermodynamic limit of size  $L^{\text{Dim}}$ , where  $\text{Dim}$  is the number of spacial dimensions, the entanglement obeys the so-called area law if the Hamiltonian of the lattice is restricted to short range interaction with a gap to excitations. In such a case the von Neumann entropy scales as  $S \sim L^{\text{Dim}-1}$ . Therefore, the von Neumann entropy saturates to a fixed value for one-dimensional systems and the number of RDM eigenstates required to represent  $|\psi\rangle$  is limited and does not extend with system length. For two-dimensional systems  $S \sim L$  which make an efficient approximation limited, in general, to small system sizes. Conformal field theory provides  $S \sim \ln L$  for one-dimensional systems at criticality meaning that the required RDM eigenstates extend with system length and, hence, properties at the thermodynamic limit can not be efficiently approximated.

At this point, descriptions will be presented of how DMRG provides algorithms to efficiently give the approximated state  $|\psi'\rangle$  (1.9) by starting from fully diagonalizable system size and successively building  $|\psi'\rangle$  for larger system sizes.

## DMRG algorithms

The main two algorithms for DMRG are the infinite-system and the finite-system algorithms. Both are described for one-dimensional lattice with open boundary conditions. The infinite-system algorithm can be illustrated by the following steps

1. A Hamiltonian  $H_l$  for a system block of length  $l$  and a Hamiltonian  $H_{l'}$  for an environment block of length  $l'$  are formed with  $l = l'$ .
2. Both Hamiltonians are enlarged by adding one more site to the system block to be  $H_{l+1}$  as well as to the environment block to be  $H_{l'+1}$ . This gives a construction of super-block Hamiltonian  $H_{l+1, l'+1}$ . The initial super-block Hamiltonian must be exactly diagonalizable.
3. Using sparse matrix exact diagonalization, an eigenstate (denoted the target state in DMRG terminology) of the super-block Hamiltonian and its eigenvalue are obtained. Usually this state is the ground state of the Hamiltonian or one of the lowest excited states.
4. RDM is obtained using Eq.(1.4) for the enlarged system block and similarly for the enlarged environment block.
5. Using dense matrix exact diagonalization the eigenvalues as well as the eigenstates of the system block RDM are obtained and then ordered by descending eigenvalues. Similar process is done for the environment block to obtain its RDM eigenstates (RDM eigenvalues are similar to those obtained for the system block).
6. The RDM eigenstates with large "enough" eigenvalues are used to construct the columns of a matrix which is used to transform the enlarged system block Hamiltonian  $H_{l+1}$  to new basis in order to form a new system block, i.e.  $H_{l+1} \rightarrow H_l$ . Similar process is done for the environment block.
7. A repetition from step 2. is proceeded until a desired super-block length  $L = l + l'$  is obtained.

These steps are sketched in Fig. 1.2. One can notice that the environment in the infinite-system algorithm is approximated and enlarged successively. This leads to an additional source of error beside the truncation error. Furthermore, the size of the full 1D lattice changes until the end of the calculations while the total number of particles may changes leading to change in the filling during the calculations. This makes the infinite-system algorithm contradict with the canonical ensemble nature of DMRG described so far and the final results are usually not satisfactory.

To overcome these problems a finite-system algorithm is used which is described as follow

0. The infinite-system algorithm is performed until a desired length  $L$  is reached. At each iteration all Hamiltonians  $H_l$  and  $H_{l'}$  and operators which connect blocks are stored.



Figure 1.2: Schematic representation of the infinite-system algorithm of the DMRG method. The black squares represent the enlarged system and environment blocks while the red circles represent the added sites.

1. The system block is enlarged by connecting to the nearest site, i.e.  $H_{l+1}$  is formed. An environment block is constructed from the nearest site to the enlarged system block and  $H_{l-2}$ , i.e.  $H_{l-1}$  is formed.
2. A new super-block is constructed and it consists of the new system block  $H_{l+1}$ , and the environment block  $H_{l-1}$ . The target state is calculated for this new super-block.
3. Similar to steps 4. to 6. in the infinite-system algorithm, the new enlarged system block  $H_{l+1}$  is transformed to the basis of RDM to form and store new system block  $H_l$  and other required operators.
4. The environment block is relabeled  $H_{l-1} \rightarrow H_l$  and steps 1. to 4. are repeated until  $H_{l=1}$  or a full diagonalizable environment is reached.
5. The procedure is reversed by constructing an enlarged environment block consists of  $H_l$  and the nearest site, i.e.  $H_{l+1}$  is formed. A system block is constructed from the nearest site to the enlarged environment block and  $H_{l-2}$ , i.e.  $H_{l-1}$  is formed.
6. A new super-block is constructed consists of the new environment block  $H_{l+1}$ , and the system block  $H_{l-1}$ . The target state is calculated for this new super-block.
7. Similar to steps 4. to 6. in the infinite-system algorithm, the new enlarged environment block  $H_{l+1}$  is transformed to the basis of RDM to form and store new environment block  $H_l$  and other required operators.
8. The system block is relabeled  $H_{l-1} \rightarrow H_l$  and steps 5. to 7. are repeated until  $H_{l=1}$  or a full diagonalizable environment is reached.
9. A repetition from step 1 is performed until reaching energy convergence.

These procedures are depicted in Fig. 1.3. The enlargement of the system block from left to right and of the environment block from right to left are called left and right sweeps, respectively. After finishing step 0 (a warm-up step) the length and the total number of

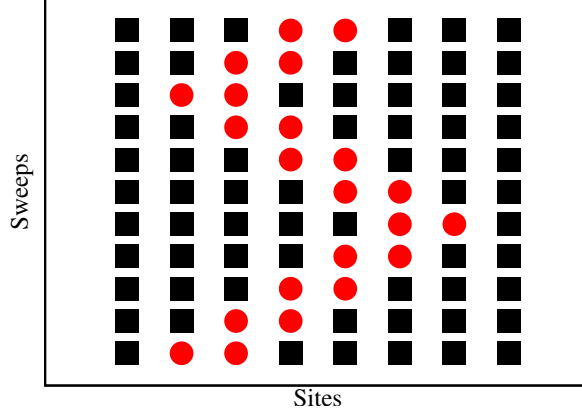


Figure 1.3: Schematic representation of the finite-system algorithm of the DMRG method after constructing the lattice using the infinite-system algorithm described in Fig. 1.2. The red circles represent the added sites and the black squares represents the enlargement or shrinking of the system or the environment blocks during sweeps.

particles remains constant. Thus, the remaining steps will be performed on a canonical system. Updating system and environment blocks within sweeps while adding two full sites between them improve the calculated target state and its eigenenergy.

Any local operator must be constructed and transformed to new RDM in each updating step of the system and environment blocks. However, the measurements could be done using the final target state or during the iterations.

## Matrix Product States representation

Major advancements in DMRG are achieved by utilizing the fact that the target state produced by DMRG is in the form of matrix product states (MPS), cf. [52]. This can be explained by successive applications of the SVD on a matrix of the coefficients of the many body wavefunction Eq.(1.2). In the first step, the coefficients  $C_{(\sigma_1, \dots, \sigma_L)}$  are reshaped in a form of a matrix of dimension  $(d \times d^{L-1})$ , i.e.

$$C_{(\sigma_1, \dots, \sigma_L)} = \Psi_{\sigma_1, (\sigma_2, \dots, \sigma_L)}. \quad (1.18)$$

Then, by performing the SVD on  $\Psi_{\sigma_1, (\sigma_2, \dots, \sigma_L)}$  the results will be

$$\Psi_{\sigma_1, (\sigma_2, \dots, \sigma_L)} = \sum_{a_1}^{r_1} U_{\sigma_1, a_1} S_{a_1, a_1} (V^\dagger)_{a_1, (\sigma_2 \dots \sigma_L)}. \quad (1.19)$$

$S$  and  $V^\dagger$  can be multiplied to get

$$\Psi_{\sigma_1, (\sigma_2, \dots, \sigma_L)} = \sum_{a_1}^{r_1} U_{\sigma_1, a_1} C_{(a_1, \sigma_2, \dots, \sigma_L)}. \quad (1.20)$$

Here,  $r_1$  is equivalent to  $\mathcal{D}_{\text{Schmidt}}$  in the Schmidt decomposition described before, which, in the current case, satisfies the relation  $r_1 \leq d$ . The matrix  $U$  represents a set of  $d$  row vectors  $A^{\sigma_1}$  with elements  $A_{a_1}^{\sigma_1} = U_{\sigma_1, a_1}$ . The coefficients,  $C_{(a_1, \sigma_2, \dots, \sigma_L)}$  can be reshaped as

$$C_{(a_1, \dots, \sigma_L)} = \Psi_{(a_1 \sigma_2), (\sigma_3 \dots \sigma_L)} \quad (1.21)$$

to form a matrix with dimension  $r_1 d \times d^{L-2}$ . Then, the SVD can be applied, again, to obtain

$$\Psi_{(a_1\sigma_2),(\sigma_3\dots\sigma_L)} = \sum_{a_2}^{r_2} U_{(a_1\sigma_2),a_2} S_{a_2,a_2} (V^\dagger)_{a_2,(\sigma_3\dots\sigma_L)} \quad (1.22)$$

with  $r_2 \leq r_1 d \leq d^2$ . The entries of matrix  $U$  can be given as  $A_{a_1,a_2}^{\sigma_2}$  which mean that  $U$  consists of a set of matrices  $A^{\sigma_2}$  each has the dimension  $r_1 \times r_2$ . The total number of these  $A^{\sigma_2}$  matrices is  $d$ . The multiplication of  $S$  and  $V^\dagger$  results in  $C_{a_2,(\sigma_3\dots\sigma_L)}$  which gives

$$\Psi_{(a_1\sigma_2),(\sigma_3\dots\sigma_L)} = \sum_{a_2}^{r_2} A_{a_1,a_2}^{\sigma_2} C_{a_2,(\sigma_3\dots\sigma_L)}. \quad (1.23)$$

The reshaping and the SVD can be repeated until a matrix  $A^{\sigma_L}$  is reached. Then, by combining the full set of the  $A$  matrices,  $C_{(\sigma_1,\dots,\sigma_L)}$  can be written as

$$C_{(\sigma_1,\dots,\sigma_L)} = \sum_{a_1,a_2,\dots,a_{L-1}} A_{a_1}^{\sigma_1} A_{a_1,a_2}^{\sigma_2} \dots A_{a_{L-2},a_{L-1}}^{\sigma_{L-1}} A_{a_{L-1}}^{\sigma_L}. \quad (1.24)$$

The sum over  $a_1, a_2, \dots, a_{L-1}$  represents matrix multiplications which offer the possibility to write the compact form

$$C_{(\sigma_1,\dots,\sigma_L)} = A^{\sigma_1} A^{\sigma_2} \dots A^{\sigma_{L-1}} A^{\sigma_L} \quad (1.25)$$

and, hence, the many body state in Eq.(1.2) can be written as

$$|\psi\rangle = \sum_{(\sigma_1,\dots,\sigma_L)} A^{\sigma_1} A^{\sigma_2} \dots A^{\sigma_{L-1}} A^{\sigma_L} |(\sigma_1, \dots, \sigma_L)\rangle \quad (1.26)$$

which is a MPS form. The maximum dimensions of the  $A^{\sigma_l}$  matrices are given by the sequence  $(1 \times d), (d \times d^2), \dots, (d^{L/2-1} \times d^{L/2}), (d^{L/2} \times d^{L/2-1}), \dots, (d^2 \times d), (d \times 1)$ . However, this maximum is reduced if the number of non-zero Schmidt values is less than  $d$ . The matrices  $A^{\sigma_l}$  are left normalized, i.e.

$$\sum_{\sigma_l} A^{\sigma_l \dagger} A^{\sigma_l} = I \quad (1.27)$$

which produce left-canonical MPS. The right canonical condition is not necessarily satisfied for the  $A^{\sigma_l}$  matrices, i.e.  $\sum_{\sigma_l} A^{\sigma_l} A^{\sigma_l \dagger} \neq I$ .

Similar construction of MPS can be done using left normalized matrices to produce left-canonical MPS. In this case the SVD can be carried out successively but each time a matrix,  $B^\sigma$ , is constructed out of  $V^\dagger$ . This can be done by first reshaping  $C_{(\sigma_1,\dots,\sigma_L)}$  in the form

$$C_{(\sigma_1,\dots,\sigma_L)} = \Psi_{(\sigma_1,\dots,\sigma_{L-1}),\sigma_L}. \quad (1.28)$$

Then, by performing the SVD one gets

$$\begin{aligned} \Psi_{(\sigma_1,\dots,\sigma_{L-1}),\sigma_L} &= \sum_{a_{L-1}} U_{(\sigma_1,\dots,\sigma_{L-1}),a_{L-1}} S_{a_{L-1},a_{L-1}} (V^\dagger)_{a_{L-1},\sigma_L} \\ &= \sum_{a_{L-1}} \Psi_{(\sigma_1,\dots,\sigma_{L-2}),(\sigma_{L-1}a_{L-1})} B_{a_{L-1}}^{\sigma_L}. \end{aligned} \quad (1.29)$$



and

$$\begin{aligned}\Psi_{(\sigma_1, \dots, \sigma_{L-2}), (\sigma_{L-1} a_{L-1})} &= \sum_{a_{L-2}} U_{(\sigma_1, \dots, \sigma_{L-2}), a_{L-2}} S_{a_{L-2}, a_{L-2}} (V^\dagger)_{a_{L-2}, (\sigma_{L-1} a_{L-1})} \\ &= \sum_{a_{L-1}} \Psi_{(\sigma_1, \dots, \sigma_{L-3}), (\sigma_{L-2} a_{L-2})} B_{a_{L-2}, a_{L-1}}^{\sigma_{L-1}}.\end{aligned}$$

until it reaches the form

$$C_{(\sigma_1, \dots, \sigma_L)} = \sum_{a_1, a_2, \dots, a_{L-1}} B_{a_1}^{\sigma_1} B_{a_1, a_2}^{\sigma_2} \dots B_{a_{L-2}, a_{L-1}}^{\sigma_{L-1}} B_{a_{L-1}}^{\sigma_L}. \quad (1.30)$$

Then, similar to Eq.(1.26), the many body state can take the compact form

$$|\psi\rangle = \sum_{(\sigma_1, \dots, \sigma_L)} B^{\sigma_1} B^{\sigma_2} \dots B^{\sigma_{L-1}} B^{\sigma_L} |(\sigma_1, \dots, \sigma_L)\rangle. \quad (1.31)$$

A combination of the left and the right canonical forms can also be constructed which gives

$$|\psi\rangle = \sum_{(\sigma_1, \dots, \sigma_L)} A^{\sigma_1} A^{\sigma_2} \dots A^{\sigma_{l-1}} A^{\sigma_l} S B^{\sigma_{l+1}} \dots B^{\sigma_{L-1}} B^{\sigma_L} |(\sigma_1, \dots, \sigma_L)\rangle \quad (1.32)$$

where  $S$  is a diagonal matrix of the singular values. This mixed canonical form is equivalent to the Schmidt decomposition

$$|\psi\rangle = \sum_{\alpha} s_{\alpha\alpha} |u^\alpha\rangle_A \otimes |\nu^\alpha\rangle_B. \quad (1.33)$$

where  $s_{\alpha\alpha}$  are the entries of  $S$ ,

$$|u^\alpha\rangle_A = \sum_{(\sigma_1, \dots, \sigma_l)} A^{\sigma_1} A^{\sigma_2} \dots A^{\sigma_{l-1}} A^{\sigma_l} |(\sigma_1, \dots, \sigma_l)\rangle \quad (1.34)$$

and

$$|\nu^\alpha\rangle_B = \sum_{(\sigma_{l+1}, \dots, \sigma_L)} B^{\sigma_{l+1}} \dots B^{\sigma_{L-1}} B^{\sigma_L} |(\sigma_1, \dots, \sigma_L)\rangle. \quad (1.35)$$

The DMRG algorithms described before give the target state in the form of a MPS. Actually, the finite-system DMRG can be seen as an iterative update of the target state in the form of Eq.(1.32) by sweeping the position of the matrix  $S$  back and forth.

## Some computational considerations

To enhance the accuracy of the calculated eigenenergy and target state one should increase systematically the number of retained RDM states in several sets of left and right sweeps. This leads to a reduction in the truncation error which can be used to extrapolate the eigenenergy to the limit of vanishing error. The infinite and finite system algorithms are implemented for strictly one-dimensional lattice with open boundary conditions which have a well defined order of sites. To perform DMRG for a lattice with ladder-like structure it is important to define an appropriate way to order the sites in a 1D-like

structure while reducing the long-range coupling which arose by such a reordering. The calculations of the ground state of a 1D lattice with short range interaction give accurate results. However, the two-site correlations such as density-density correlations do not converge as the ground state, which makes the investigation of correlations that decay in power-law much more demanding.

DMRG is the main method used to study ladder models of metallic wire on a substrate. It will be assisted by Quantum Monte Carlo (QMC) calculations done by Martin Hohenadler. Moreover, analysis of limiting cases, Hartree-Fock calculations and noninteracting cases will be used to support DMRG calculations.

# Chapter 2

## Asymmetric 2-leg ladder system

Asymmetric ladder systems, i.e. ladders made of two inequivalent legs, have been proposed as models for linear atomic wires deposited on the surface of a substrate in order to investigate the influence of the substrate on hallmarks of one-dimensional physics such as the Peierls instability [54] and the Luttinger liquid behavior [55, 56]. However, this approach has not been pursued systematically so far. Nevertheless, the one-dimensional Kondo-Heisenberg model has been the most studied asymmetric ladder system but in other context. It was used to investigate exotic superconducting correlations in striped-ordered high-temperature superconductors [57, 58, 59, 60] as well as quantum phase transitions in heavy-fermion materials [61]. From an other side, a two-band Hubbard model on a ladder lattice was the starting point of an investigation of pairing mechanisms in strongly repulsive fermion systems [62].

The first approach chosen in this thesis is to consider an asymmetric 2-leg ladder consisting of a correlated 1D chain, namely the 1D Hubbard model [11], and a 1D tight binding chain. The correlated chain represents a wire and the noninteracting chain represents a substrate. Up to my knowledge, the only work on this model is done in Ref. [48] in the context of proximity effect in high-temperature-superconductors. Most of the investigations presented here are published in Ref. [47] and [63]

### 2.1 The model

The asymmetric ladder is displayed in Fig. 2.1. The Hamiltonian of the asymmetric ladder model is

$$\begin{aligned} H = & -t_{\parallel} \sum_{x,y,\sigma} \left( c_{x+1,y,\sigma}^{\dagger} c_{x,y,\sigma} + c_{x,y,\sigma}^{\dagger} c_{x+1,y,\sigma} \right) \\ & - t_{\perp} \sum_{x,\sigma} \left( c_{x,F,\sigma}^{\dagger} c_{x,H,\sigma} + c_{x,H,\sigma}^{\dagger} c_{x,F,\sigma} \right) \\ & + U \sum_x \left( n_{x,H,\uparrow} - \frac{1}{2} \right) \left( n_{x,H,\downarrow} - \frac{1}{2} \right). \end{aligned} \quad (2.1)$$

Here  $c_{x,y,\sigma}$  ( $c_{x,y,\sigma}^{\dagger}$ ) represents an annihilation (creation) operator for an electron with spin  $\sigma$  on a site with coordinates  $(x, y)$  where  $y = H$  (Hubbard leg) or  $y = F$  (Fermi leg). The rung index  $x$  runs from 1 to the ladder length  $L$ . The corresponding electron number

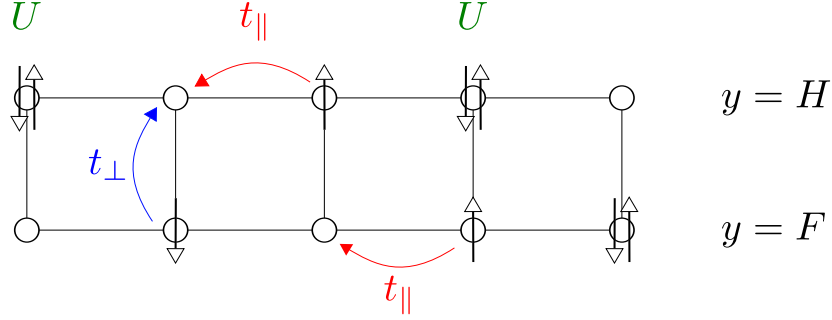


Figure 2.1: A schematic representation of the asymmetric 2-leg Hubbard ladder described by Hamiltonian 2.1. This figure is adapted from Ref [47].

operator is  $n_{x,y,\sigma} = c_{x,y,\sigma}^\dagger c_{x,y,\sigma}$ . Each site has the possibility to be occupied by two electrons with opposite spin direction, thus, the half filling corresponds to the number of electrons  $N = 2L$ . The Hamiltonian is invariant under the particle-hole transformation  $c_{xy\sigma} \rightarrow (-1)^x c_{xy\sigma}^\dagger$ . Therefore, at half filling the Fermi energy is always equal to 0 and it is sufficient to investigate the cases corresponding to  $N \geq 2L$ . The investigations are restricted to repulsive interactions ( $U \geq 0$ ) only. The canonical gauge transformation  $c_{xH\sigma} \rightarrow -c_{xH\sigma}, c_{xF\sigma} \rightarrow c_{xF\sigma}$  merely changes the sign of the hopping term  $t_\perp$  and another canonical gauge transformation  $c_{xy\sigma} \rightarrow (-1)^x c_{xy\sigma}$  simply changes the sign of  $t_\parallel$ , therefore, only the cases  $t_\parallel \geq 0$  and  $t_\perp \geq 0$  will be considered. The energy unit is  $t_\parallel = 1$ . In general, this Hamiltonian is not exactly solvable, but, by analyzing limiting cases which are amenable to analytical calculations one can get some ideas about its properties.

### 2.1.1 Weak interactions

The first limit is the limit of vanishing interaction  $U$ . The non-interacting system with ( $U = 0$ ) resembles the well-known symmetric tight-binding ladder [4]. The Hamiltonian is diagonalized using the bonding and anti-bonding rung states defined by operators

$$b_{k,\sigma} = \frac{1}{2L} \sum_x e^{ikx} (c_{x,H,\sigma} + c_{x,F,\sigma}) \quad (2.2)$$

and

$$a_{k,\sigma} = \frac{1}{2L} \sum_x e^{ikx} (c_{x,H,\sigma} - c_{x,F,\sigma}), \quad (2.3)$$

respectively. Hence, the diagonal form is

$$H = \sum_{k\sigma} E_b(k) b_{k,\sigma}^\dagger b_{k,\sigma} + \sum_{k\sigma} E_{ab}(k) a_{k,\sigma}^\dagger a_{k,\sigma} \quad (2.4)$$

with the bonding band dispersion

$$E_b(k) = -t_\perp - 2t_\parallel \cos(k) \quad (2.5)$$

and the anti-bonding band dispersion

$$E_{ab}(k) = +t_\perp - 2t_\parallel \cos(k). \quad (2.6)$$

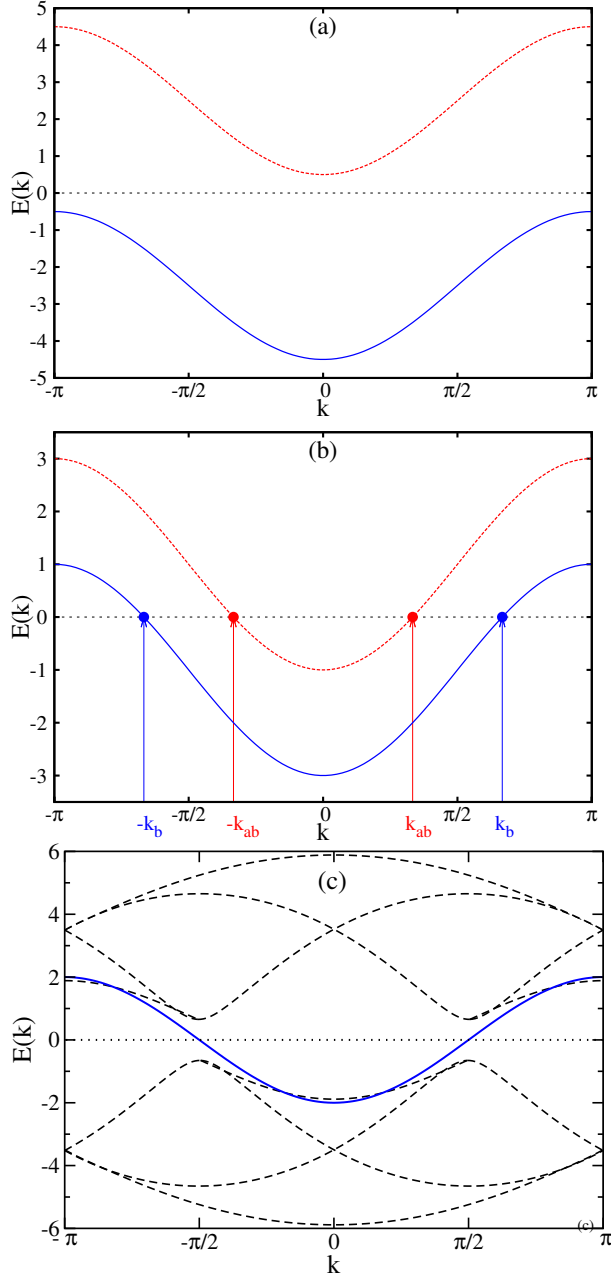


Figure 2.2: Single-particle dispersions of the noninteracting ladder for (a)  $t_{\perp} = 2.5$ , (b)  $t_{\perp} = 1$ . The four Fermi points,  $\pm k_{ab}$  and  $\pm k_b$  defined by Eq. (2.8), are shown in (b). Single holon-spinon continuum is shown in (c) within the area included by dashed lines resulting from the Bethe ansatz solution of the half-filled Hubbard chain with  $U = 4$ . Single-particle dispersion of the tight-binding chain is shown in (c) as a solid blue line. A horizontal dotted line shows the Fermi energy at half-filling in all three figures. These figures are adapted from Ref [47].

The wave numbers  $k$  in the first Brillouin zone  $[-\pi, \pi]$  are given by  $k = \frac{2\pi}{L}z$  with integers  $-\frac{L}{2} < z \leq \frac{L}{2}$  for periodic boundary conditions. For  $t_{\perp} > 2$  the ladder spectrum has an indirect gap

$$E_{\text{band}} = 2t_{\perp} - 4t_{\parallel} \quad (2.7)$$

between the wave numbers  $k_b = \pm\pi$  in the bonding band and  $k_{ab} = 0$  in the anti-bonding band, see Fig. 2.2(a). This leads to a band insulating ladder at half filling, but it is metallic with two Fermi points at other band fillings. The case of weak on-site interaction  $U \ll E_{\text{gap}}$  is much more easier to analyze in the dimer limit (see Sec. 2.1.4). For  $t_{\perp} < 2$  at or close to half filling the ladder spectrum is gapless with two pairs of perfectly nested Fermi points,  $\pm k_b$  ( $\frac{\pi}{2} < k_b < \pi$ ) and  $\pm k_{ab}$  ( $0 < k_{ab} < \frac{\pi}{2}$ ) given by the equations

$$t_{\perp} = -2t_{\parallel} \cos(k_b) = 2t_{\parallel} \cos(k_{ab}), \quad (2.8)$$

see Fig. 2.2(b). The nesting wave number is  $\pi = k_b + k_{ab}$ . For finite weak on-site interaction, i.e.  $U \ll t_{\perp}, t_{\parallel}$ , the ladder symmetry is lowered making investigations using sophisticated field-theoretical approaches such as bosonization and renormalization group methods (as it has been done for symmetric ladders [4, 64, 65, 66, 67, 68]) harder than in the case of symmetric ladders. However, such an investigation has not been performed so far. Therefore, based on the known results for symmetric ladders [4, 64, 65, 66, 67, 68], the excitation spectrum of the half-filled asymmetric ladder is expected to become fully gapped as soon as  $U > 0$  due to the umklapp scattering allowed by the perfect nesting of the Fermi points with a nesting wave number  $\pi$ . Thus, the system is expected to be a spin-gapped Mott insulator with lowest single-particle excitations characterized by four incommensurate wave numbers  $\pm k_g$  and  $\pm k'_g$  with  $k_g \approx k_b$  and  $k'_g \approx k_{ab}$ .

## 2.1.2 Strong interactions

This limit is distinguished by a very large on-site interaction  $U$  which corresponds to  $t_{\perp} = t_{\parallel} = 0$ . In this case the electrons are highly site-localized and the ladder system has a highly degenerate ground state. At or close to half filling, the Hubbard leg has exactly one electron in each site and the other electrons distribute arbitrarily on the Fermi leg. For small but finite hopping terms ( $t_{\perp}, t_{\parallel} \ll U$ ) a clear similarity can be seen between the asymmetric 2-leg ladder Eq.(2.1) and the periodic Anderson model. Therefore, it is convenient to start the analysis by assuming  $t_{\parallel} = 0$  only in the Hubbard leg and  $t_{\perp} \ll U$ . Hence, the so called Schrieffer-Wolff transformation [69] could be applied. This leads to the Kondo lattice model [70] with an antiferromagnetic exchange interaction  $J_{\perp} = 8t_{\perp}^2/U$ . Two additional second-order interaction terms appear if the hopping term  $t_{\parallel} \neq 0$  is considered in both ladder legs. The first interaction is an intra-chain antiferromagnetic exchange coupling  $J_{\parallel} = 4t_{\parallel}^2/U$  in the Hubbard leg. The second one is a next-nearest-neighbor correlated hopping term  $t_{\parallel}t_{\perp}/U$  between Hubbard and Fermi legs. The elimination of the of the next-nearest-neighbor terms makes the system a Kondo-Heisenberg model [57, 58, 59, 60, 61]. However, as long as  $t_{\parallel}$  has the same value for both legs, the asymmetric 2-leg ladder Eq.(2.1) in the strong-coupling limit is not exactly equivalent to the Kondo-Heisenberg model. This case shows the importance of the next-nearest-hopping [71, 15] and generalizes the Kondo-Heisenberg model to a finite-charge-gap Mott insulator. Therefore, this phase is named Kondo-Mott insulator.

Nevertheless, Hamiltonian (2.1) at half filling should show low-energy gapped excitations with  $J_{\perp} = 8t_{\perp}^2/U$  at strong interaction  $U$ .

### 2.1.3 Chain limit

This limit corresponds to decoupled legs in the asymmetric ladder i.e.  $t_{\perp} = 0$ . The noninteracting Fermi leg is described by a nearest-neighbor tight-binding Hamiltonian in one dimension which can be diagonalized using a transformation to momentum space. The second leg is a one-dimensional Hubbard chain which is exactly solvable by the Bethe Ansatz [11]. At half filling, electronic states of the Fermi leg are filled up to the Fermi level and the Hubbard leg is a one-dimensional Mott insulator with charge gap  $E_H$  and gapless spin excitations. Any added or removed electrons close to half filling are distributed entirely on the Fermi leg with a wave vector close to  $k_F \approx \pm \frac{\pi}{2}$  and an energy close to the Fermi energy  $E_F = 0$ . Therefore, charge excitations will localize on the Fermi leg. On the other hand, both legs will have gapless spin excitations but the spin velocity in the Hubbard leg is smaller than  $2t_{\parallel}$  and decreases with increasing  $U/t_{\parallel}$ . This makes the asymmetric ladder system metallic with independent low energy excitations. By introducing small inter-chain hopping  $t_{\perp}$ , an electron can move from one leg to the other and creates an excitation with an energy larger than or equal to  $E_H/2$ . Thus, there are two possibilities to treat the asymmetric 2-leg ladder in this case. One possibility is to use the perturbation theory which just gives small corrections to eigenenergies due to the non-degenerate ground state. Thus, the ladder has gapless independent charge and spin excitations meaning that it is a Luttinger liquid. The other possibility is due to an expected effective interaction on the Fermi leg induced by the interplay between the Hubbard interaction  $U$  and the inter-chain hopping  $t_{\perp}$ . This interaction should cause an umklapp scattering which opens spin and charge gaps due to the perfect nesting of the Fermi points  $k_F = \pm \frac{\pi}{2}$ . It is known that the 1D Hubbard model has the same low-energy spin correlations as the spin- $\frac{1}{2}$  1D Heisenberg model. Thus, the low-energy physics in the limit of weakly coupled chains could be investigated using field theoretical methods similar to what have been done for the Kondo-Heisenberg model [58, 59, 66, 67].

### 2.1.4 Dimer limit

The dimer limit is the asymmetric 2-leg ladder with  $t_{\parallel} = 0$ . In this case, the system consists of independent subsystems of two sites, a dimer on each ladder rung. Each independent dimer is described by the Hamiltonian

$$H_x = U \left( n_{x,H,\uparrow} - \frac{1}{2} \right) \left( n_{x,H,\downarrow} - \frac{1}{2} \right) - t_{\perp} \sum_{\sigma} \left( c_{x,H,\sigma}^{\dagger} c_{x,F,\sigma} + c_{x,F,\sigma}^{\dagger} c_{x,H,\sigma} \right). \quad (2.9)$$

The Hilbert space of each rung has the dimension 16. However, the spin  $S_z^x$  and the particle number  $N^x$  operators of each rung  $x$  commute with the rung Hamiltonian

$$[H_x, N^x] = [H_x, S_z^x] = 0 \quad (2.10)$$

Thus, the Hilbert space can be decomposed into subspaces depending on the possible choices of  $N^x$  and  $S_z^x$ . Therefore, the possible ground state energies  $E_x(N^x, S_z^x)$  are

$$E_x(4, 0) = E_x(0, 0) = \frac{U}{4}, \quad (2.11)$$

$$E_x \left( 3, \pm \frac{\hbar}{2} \right) = \pm \sqrt{\left( \frac{U}{4} \right)^2 + t_{\perp}^2}, \quad (2.12)$$

$$E_x \left( 1, \pm \frac{\hbar}{2} \right) = \pm \sqrt{\left( \frac{U}{4} \right)^2 + t_{\perp}^2}, \quad (2.13)$$

$$E_x(2, \pm \hbar) = -\frac{U}{4}, \quad (2.14)$$

and

$$E_x(2, 0) = \pm \sqrt{\left( \frac{U}{4} \right)^2 + 4t_{\perp}^2}. \quad (2.15)$$

Eq.(2.15) is the lowest ground state which corresponds to a singlet formed by two electrons in each rung. This means that the lowest spin excitation corresponds to forming a triplet out of the singlet ground state with the spin gap given by

$$E_s = -\frac{U}{4} + \sqrt{\left( \frac{U}{4} \right)^2 + 4t_{\perp}^2}. \quad (2.16)$$

Using Taylor expansion, one gets

$$E_s \simeq 2t_{\perp} - \frac{U}{4} + \frac{U^2}{64t_{\perp}} \quad \text{for } t_{\perp} \gg U \quad (2.17)$$

and

$$E_s \simeq \frac{8t_{\perp}^2}{U} \quad \text{for } t_{\perp} \ll U. \quad (2.18)$$

Charge excitations can be made by two ways. One way is by removing one particle from one rung and adding it to another rung. This could be seen as a delocalized excitation which has the charge gap

$$E_c = -2\sqrt{\left( \frac{U}{4} \right)^2 + t_{\perp}^2} + 2\sqrt{\left( \frac{U}{4} \right)^2 + 4t_{\perp}^2}. \quad (2.19)$$

The other way of excitation is by adding an electron to one rung from outside the ladder system. This can be seen as a localized excitation which is characterized by the charge gap

$$E_c = \frac{U}{4} + \sqrt{\left( \frac{U}{4} \right)^2 + 4t_{\perp}^2}. \quad (2.20)$$

The lowest charge excitation corresponds to the delocalized one which has the charge excitation energy

$$E_c \simeq 2t_{\perp} \quad \text{for } t_{\perp} \gg U \quad (2.21)$$

and

$$E_c \simeq \frac{12t_{\perp}^2}{U} \quad \text{for } t_{\perp} \ll U. \quad (2.22)$$

Therefore, the ground state at half filling for  $t_{\perp} = 0$  is an insulator. By doping the dimer system the charge and spin gaps are closed turning the system to a gapless state. If  $t_{\parallel} \ll E_c, E_s$  is introduced it is possible to use perturbation theory treatment. However, this will not change the scaling of gaps with  $\sim 2t_{\perp}$  for  $U \ll t_{\perp}$  and with  $\sim \frac{t_{\perp}^2}{U}$  for  $U \gg t_{\perp}$ .



## 2.2 Hartree-Fock approximation at half filling

The Hartree-Fock approximation is used to gain more qualitative description of the asymmetric 2-leg ladder at half-filling. It is usually a method for weak interactions  $U$  [10]. In general this method approximates the ground state of many-electron system using single-particle states and the antisymmetric nature of fermions. For the asymmetric ladder, this method is applied by formulating the ground state  $|\phi\rangle$  of the ladder as a product of two states, one represents spin-up electrons and the other represents spin-down electrons, i.e.

$$|\phi\rangle = |\phi_\uparrow\rangle|\phi_\downarrow\rangle. \quad (2.23)$$

This yields the ground state energy

$$E(\phi) = \langle\phi|H|\phi\rangle = E(\phi_\uparrow, \phi_\downarrow) \quad (2.24)$$

with the interaction energy term approximated as

$$\langle\phi|U\sum_x n_{x,H,\uparrow}n_{x,H,\downarrow}|\phi\rangle = U\sum_x \langle\phi_\uparrow|n_{x,H,\uparrow}|\phi_\uparrow\rangle\langle\phi_\downarrow|n_{x,H,\downarrow}|\phi_\downarrow\rangle. \quad (2.25)$$

Applying this approximation to the Hamiltonian (2.1) produces two independent single-particle Hamiltonians

$$\begin{aligned} H_\sigma &= -t_\parallel \sum_{x,y} \left( c_{x,y,\sigma}^\dagger c_{x+1,y,\sigma} + c_{x+1,y,\sigma}^\dagger c_{x,y,\sigma} \right) \\ &\quad - t_\perp \sum_x \left( c_{x,H,\sigma}^\dagger c_{x,F,\sigma} + c_{x,F,\sigma}^\dagger c_{x,H,\sigma} \right) \\ &\quad + U \sum_x n_{x,H,\sigma} \left( \langle n_{x,H,-\sigma} \rangle - \frac{1}{2} \right). \end{aligned} \quad (2.26)$$

which have to be minimized with respect to  $|\phi_\uparrow\rangle$  and  $|\phi_\downarrow\rangle$ . The minimization problem takes the form of solving the equations

$$H_\sigma|\phi_\sigma\rangle = E_\sigma|\phi_\sigma\rangle \quad (2.27)$$

self-consistently where the self-consistence condition is determined by the expectation value of the density on the Hubbard leg, i.e.  $\langle n_{x,H,-\sigma} \rangle$  as following. From the discussion in Sec. 2.1.1, the Fermi points are perfectly nested by the inter-band wave number  $k = k_b + k_{ab} = \pi$  at half filling for  $t_\perp < 2$ . Therefore, a broken-symmetry antiferromagnetic spin density wave is assumed by introducing the average density in the form

$$\langle n_{x,H,\sigma} \rangle = \frac{1}{2} + \sigma(-1)^x \frac{m_H}{2} \quad (2.28)$$

with an order parameter  $m_H$  defined as the staggered magnetization per-site of the Hubbard leg. Due to the symmetry breaking the unit cell of the effective Hamiltonian (2.26) is two times larger (four sites) than the original Hamiltonian (2.1).

The diagonalization of the effective Hamiltonian (2.26) is done using the following canonical transformation defined from Bloch theorem as

$$d_{kn\sigma}^\dagger = \sum_{x,y} \psi_{kn\sigma}(x,y) c_{x,y,\sigma}^\dagger \quad (2.29)$$

where

$$\psi_{kn\sigma}(x, y) = \frac{e^{ikx}}{\sqrt{L}} \begin{cases} u_{kn\sigma}^H + (-1)^x v_{kn\sigma}^H & y = H \\ u_{kn\sigma}^F + (-1)^x v_{kn\sigma}^F & y = F \end{cases} \quad (2.30)$$

The superscripts  $H$  and  $F$  affiliate the components corresponding to the Hubbard and Fermi legs, respectively. The wave number  $k = \frac{2\pi}{L}z$  is set by an integer  $-\frac{L}{4} < z \leq \frac{L}{4}$  in a reduced Brillouin zone  $[-\frac{\pi}{2}, \frac{\pi}{2}]$  and the index  $n = 1, 2, 3, 4$  indicate four bands. To satisfy the normalization condition, i.e.

$$\sum_k |\psi_{kn\sigma}(x, y)|^2 = 1 \quad (2.31)$$

the four components fulfill the relation

$$(|u_{kn\sigma}^H|^2 + |v_{kn\sigma}^H|^2 + |u_{kn\sigma}^F|^2 + |v_{kn\sigma}^F|^2) = 1. \quad (2.32)$$

The determination of the four components  $u_{kn\sigma}^H, v_{kn\sigma}^H, u_{kn\sigma}^F,$  and  $v_{kn\sigma}^F$  is done by solving the four-dimensional eigenvalue problem

$$H_{k\sigma} \begin{pmatrix} u_{kn\sigma}^H \\ v_{kn\sigma}^H \\ u_{kn\sigma}^F \\ v_{kn\sigma}^F \end{pmatrix} = \epsilon_{n\sigma}(k) \begin{pmatrix} u_{kn\sigma}^H \\ v_{kn\sigma}^H \\ u_{kn\sigma}^F \\ v_{kn\sigma}^F \end{pmatrix} \quad (2.33)$$

where  $H_{k\sigma}$  is given by

$$\begin{pmatrix} -2t_{\parallel} \cos(k) & -\frac{1}{2}\sigma U m_H & -t_{\perp} & 0 \\ -\frac{1}{2}\sigma U m_H & +2t_{\parallel} \cos(k) & 0 & -t_{\perp} \\ -t_{\perp} & 0 & -2t_{\parallel} \cos(k) & 0 \\ 0 & -t_{\perp} & 0 & +2t_{\parallel} \cos(k) \end{pmatrix}$$

and  $\epsilon_{n\sigma}(k)$  is a single-particle (Hartree-Fock) eigenenergy. The Hartree-Fock density  $\langle n_{xH\sigma} \rangle$  can be expressed as

$$\langle n_{xH\sigma} \rangle = \frac{1}{L} \sum_{n=1}^2 \sum_k \begin{cases} |u_{kn\sigma}^H + v_{kn\sigma}^H|^2 & \text{for even } x \\ |u_{kn\sigma}^H - v_{kn\sigma}^H|^2 & \text{for odd } x, \end{cases} \quad (2.34)$$

or, in an other expression,

$$\langle n_{xH\sigma} \rangle = \frac{1}{L} \sum_{n=1}^2 \sum_k \left[ |u_{kn\sigma}^H|^2 + |v_{kn\sigma}^H|^2 + (-1)^x (u_{kn\sigma}^H v_{kn\sigma}^{*H} + u_{kn\sigma}^{*H} v_{kn\sigma}^H) \right] \quad (2.35)$$

Therefore, from Eq. (2.28), the staggered magnetization can be written as

$$m_H = \frac{2\sigma}{L} \sum_{n=1}^2 \sum_k (u_{kn\sigma}^H v_{kn\sigma}^{*H} + u_{kn\sigma}^{*H} v_{kn\sigma}^H) \quad (2.36)$$

where the first sum runs over the lowest two bands only. The self-consistency problem is formulated by equations Eq.(2.33) and Eq.(2.36) which can be easily solved numerically.

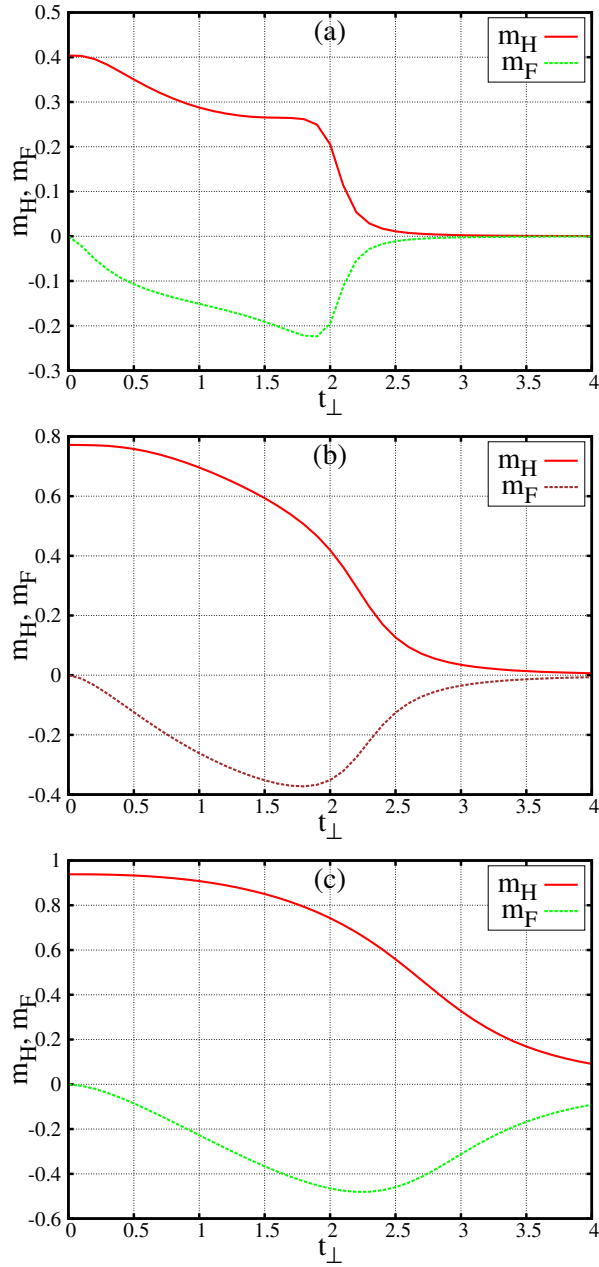


Figure 2.3: Staggered magnetization of the Hubbard leg ( $m_H$ ) and Fermi leg ( $m_F$ ) in the Hartree-Fock approximation as a function of the rung hopping  $t_\perp$  for (a)  $U = 2$ , (b)  $U = 4$  and (c)  $U = 8$ . Figure (b) is adapted from Ref [47].

Due to the perfect nesting of the Fermi points in the asymmetric ladder, there is a broken-symmetry solution  $m_H \neq 0$  for any  $U > 0$  if  $t_\perp < 2$ . Even for larger  $t_\perp$ , the results shown in Fig. 2.3, reveal small but finite values of staggered magnetizations for large  $U$  up to  $t_\perp = 4$ . The long-range antiferromagnetic order is a result of the introduced symmetry-breaking in the mean-field approximation, but it is known that the continuous  $SU(2)$  spin symmetry can not be spontaneously broken in one dimension [4, 10]. Therefore, the broken symmetry ground state in the Hartree-Fock approximation is an artifact. In Fig. 2.3 the self-consistent order parameter  $m_H$  is shown for  $U = 2, 4$  and  $8$  as a function of the rung hopping  $t_\perp$ . The value of  $m_H$  approaches the staggered magnetization obtained for the one-dimensional Hubbard model [10] when  $t_\perp \rightarrow 0$ . By increasing  $t_\perp$ ,  $m_H$  decreases monotonically especially for  $U = 8$ . A fast reduction in  $m_H$  is observed around  $t_\perp = 2$  and  $U = 2$ . This fast reduction becomes smoother for  $U = 4$ .

The coupling between Fermi and Hubbard legs induces an antiferromagnetic long range order in the Fermi leg too. The staggered magnetization of the Fermi leg can be obtained as

$$m_F = \frac{2\sigma}{L} \sum_{n=1}^2 \sum_k (u_{kn\sigma}^F v_{kn\sigma}^{*F} + u_{kn\sigma}^{*F} v_{kn\sigma}^F) \quad (2.37)$$

similarly to Eq.(2.36). The value of  $m_F$  is also shown in Fig. 2.3. Unlike the Hubbard leg, a separate Fermi leg has no staggered magnetization because it is just an independent electron gas (see Sec. 2.1.3). The antiferromagnetic order in the full system gives finite value for  $m_F$  with an opposite sign to  $m_H$ . By increasing  $t_\perp$  the absolute value  $|m_F|$  also increases due to the hybridization between electronic states in both legs. Then  $|m_F|$  decreases for large values of  $t_\perp$  which reflects a reduction of the long range order in the Hubbard leg.

The four Hartree-Fock bands can be calculated analytically for arbitrarily  $m_H$  which gives the dispersion

$$\epsilon_{n\sigma}(k) = \pm \sqrt{a(k) \pm \sqrt{b(k)}} \quad (2.38)$$

with

$$\begin{aligned} a(k) &= \frac{1}{2} \left( \frac{Um_H}{2} \right)^2 + [2t_\parallel \cos(k)]^2 + t_\perp^2 \\ b(k) &= \frac{1}{4} \left( \frac{Um_H}{2} \right)^4 + 4t_\perp^2 [2t_\parallel \cos(k)]^2 + \left( \frac{Um_H}{2} \right)^2 t_\perp^2. \end{aligned}$$

Each sign combination corresponds to one band in  $\epsilon_{n\sigma}(k)$ ,  $n = 1, 2, 3, 4$ . (Note that the bands are identical for  $\sigma = \pm 1$ ). At half filling the system is particle-hole symmetric. Thus, two Hartree-Fock bands are below the Fermi level and two are above it as it seen in Fig. 2.4. These figures show bands which correspond to a converged staggered magnetization at  $U = 5$ . The lowest single-particle excitation has the wave vector ( $k_{\text{HF}} = \pm \frac{\pi}{2}$ ) at the edge of the reduced Brillouin zone. By increasing  $t_\perp$  the lowest-energy single-particle excitation wave vector moves to an incommensurate values as shown in Fig. 2.4(b) for  $t_\perp = 1.5$ . These results are in consistence with the previous analysis in Sec. 2.1.3 for weakly coupled chains and Sec. 2.1.1 for weak interaction  $U$ . However, due to the folding of Brillouin zone in the Hartree-Fock approximation, the indirect gap in Fig. 2.2(a) becomes a direct gap. The on-site interaction  $U$  also changes  $k_{\text{HF}}$ . A clear view of the

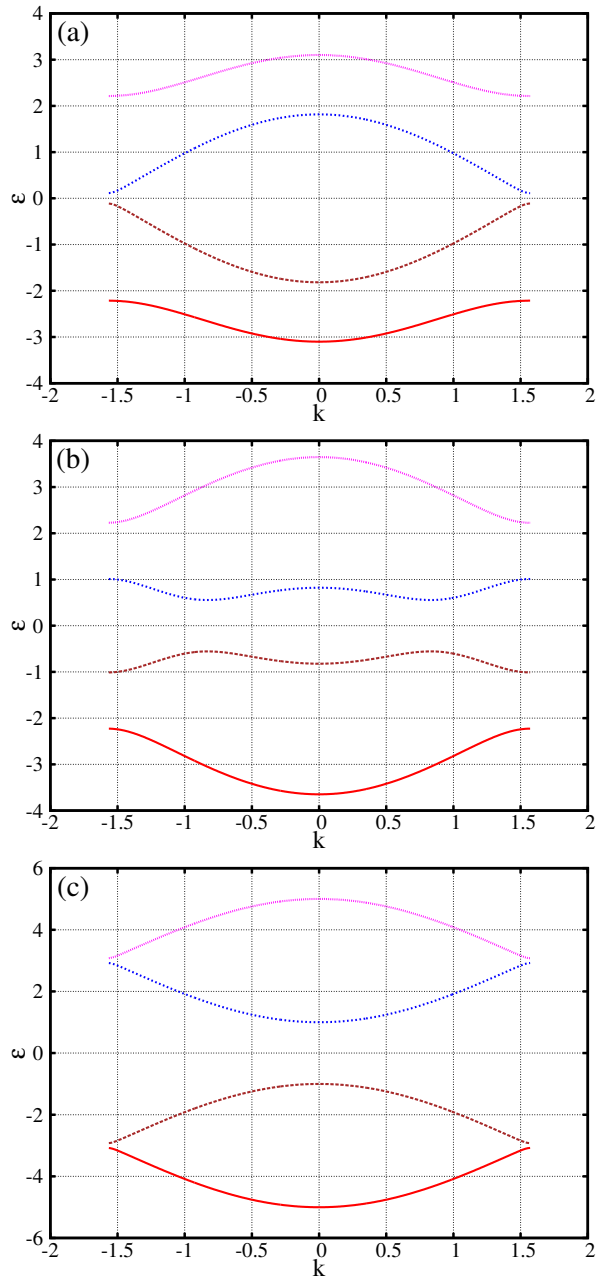


Figure 2.4: The four Hartree-Fock bands  $\epsilon_{n\sigma}(k)$  for  $U = 5$  with three values of rung hopping: (a) weak ( $t_{\perp} = 0.5$ ), (b) intermediate ( $t_{\perp} = 1.5$ ), and (c) strong ( $t_{\perp} = 3$ ). These figures are adapted from Ref [47].

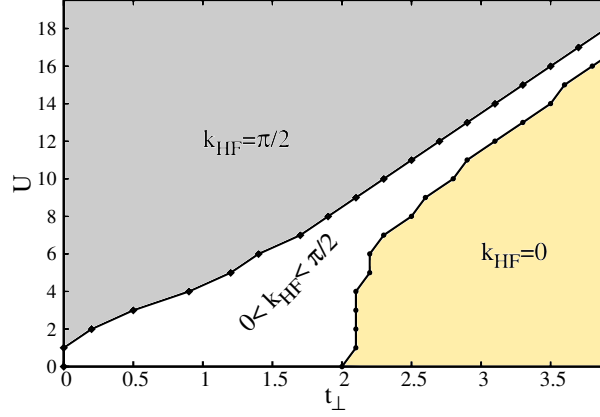


Figure 2.5: "Phase diagram" in  $(U, t_{\perp})$  resulting from the Hartree-Fock calculations. The lowest single-particle excitations distinguish three regions. Two regions with wave numbers  $k_{\text{HF}}$  at the edges of the reduced Brillouin zone, i.e.  $(k_{\text{HF}} = \pm \frac{\pi}{2})$  and  $(k_{\text{HF}} = 0)$ . One region with incommensurate values  $0 < |k_{\text{HF}}| < \frac{\pi}{2}$ . This figure is published in Ref. [47]. This figure is adapted from Ref [47].

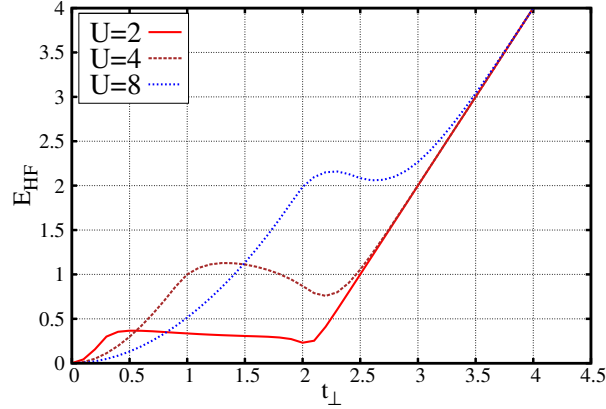


Figure 2.6: Hartree-Fock gap  $E_{\text{HF}}$  as a function of the rung hopping  $t_{\perp}$  for  $U/t_{\parallel} = 2, 4$  and 8. This figure is adapted from Ref [47].

progressive movement of single-particle excitation from  $k_{\text{HF}} = \frac{\pi}{2}$  to  $k_{\text{HF}} = 0$  through incommensurate values is given in Fig. 2.5 over a parameter range  $(U, t_{\perp})$ .

The Hartree-Fock gap at half filling is defined as the difference between the lowest state in the lowest band above the Fermi level and the highest state in the highest band below the Fermi level. If  $U = 0$  and  $t_{\perp} < 2$  or if  $t_{\perp} = 0$  the gap is zero. Any other finite values of both couplings give a finite Hartree-Fock gap. However, this gap exhibits an interestingly complex behavior as a function of the strength of the on-site interaction and rung hopping term. To describe this behavior, the Hartree-Fock gap has been calculated for different values of  $U$  and  $0 \leq t_{\perp} \leq 4$  as shown in Fig. 2.6. One can recognize three different regions by varying the rung hopping  $t_{\perp}$ . In the first region the gap increases in apparent quadratic behavior with respect to  $t_{\perp}$ , then it shows a non-monotonic form around a local maximum in the second region. A local minimum of the gap also exists at the end of the second region. The third region is characterized by a systematic increase

of the gap which then becomes a linear increase for large enough  $t_{\perp}$ . The linear behavior of the gap in the third region can be understood from the discussion in Sec. 2.1.4 for the dimer limit and Sec. 2.1.1 for the noninteracting case. In these cases, the system can be described as a band insulator with a Hartree-Fock gap that approaches the band gap in Eq. (2.7). Furthermore, this region is characterized by  $k_{\text{HF}} = 0$  for the single-particle excitation and by weak antiferromagnetic long-range orders. The antiferromagnetic order is large enough in the other two regions and is large enough to open the gap. Thus, they are described as an antiferromagnetic Mott insulator [10]. The differences between these two regions are the behavior of the gap as described before and the difference in the values of the lowest-energy single-particle excitation wave vectors which are  $k_{\text{HF}} = \frac{\pi}{2}$  in the first region and incommensurate in the second region.

## 2.3 Ground-state properties and excitation gaps

The Hartree-Fock approximation, as a mean-field approximation, can provide only qualitative descriptions for the 1D Hubbard-type models. Thus, it is important to have a method which treats explicitly the electron-electron correlation and gives, at least, a good approximation to the ground state. As it has been discussed in the introduction, DMRG has been proved to be a very good, or maybe the best, method for ground state properties of quasi-one-dimensional Hamiltonians with local interactions. It has been used for asymmetric ladders in other contexts [59], e.g. Kondo-Heisenberg models, but not for models for wire-substrate systems. The only work which addresses the asymmetric model used in this thesis [48] focused only on the spin-spin correlations at half-filling in the context of the proximity effect. The motivation was the coexistence of antiferromagnetic and pairing correlations in the multi-layered high- $T_c$  superconductors.

Here a much broader investigation is done using the DMRG to calculate ground state properties of Hamiltonian (2.1) for finite values of  $U$  and  $t_{\perp}$ . The finite-size algorithm is used with open boundary conditions. The ladder systems investigated here consist of up to 200 rungs (i.e. 400 sites). The discarded weight is kept smaller than  $10^{-6}$  by using up to  $m = 3072$  density-matrix eigenstates. The number of density-matrix eigenstates was varied systematically to extrapolate ground-state energies with discarded weights to the limit of vanishing truncation errors. The estimated errors for gaps are shown when they are larger than the symbol size in figures. The accuracy was sufficient except for weakly-coupled weakly-interacting chains with  $U \leq 4$  and  $t_{\perp} < 2$ .

### 2.3.1 Definitions of excitation gaps

To perform investigations on the asymmetric ladder model, three types of excitation gaps are calculated for Hamiltonian (2.1). The first gap is the charge gap defined as

$$E_c = \frac{1}{2} [E_0(N_{\uparrow} + 1, N_{\downarrow} + 1) + E_0(N_{\uparrow} - 1, N_{\downarrow} - 1) - 2E_0(N_{\uparrow}, N_{\downarrow})] \quad (2.39)$$

where  $E_0(N_{\uparrow}, N_{\downarrow})$  refers to the ground state energy for the asymmetric ladder with the number of electrons  $N_{\sigma}$  of spin  $\sigma$ . The half-filling corresponds to  $N_{\uparrow} = N_{\downarrow} = \frac{N}{2}$ . This

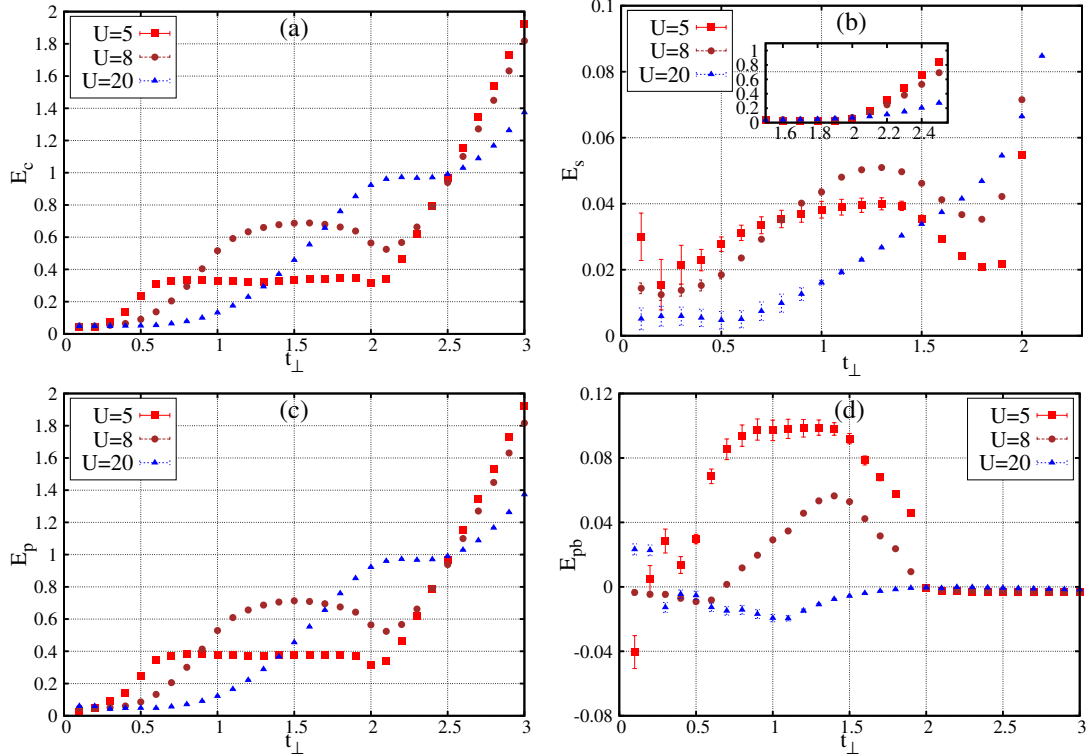


Figure 2.7: (a) Charge gap  $E_c$ , (b) spin gap  $E_s$ , (c) single-particle gap  $E_p$  and (d) pair binding energies  $E_{pb}$  as a function of the rung hopping  $t_{\perp}$  in the half-filled asymmetric Hubbard ladder (2.1) with  $L = 128$  rungs and several values of the interaction  $U$ . Figures (a), (b) and (d) are adapted from Ref. [47].

excitation varies the total number of charges while keeping the total spin unchanged. This gap is seen in the dynamical structure factor which is measured in experiments such as electron energy loss spectroscopy. The second gap is the spin gap defined as

$$E_s = E_0(N_{\uparrow} + 1, N_{\downarrow} - 1) - E_0(N_{\uparrow}, N_{\downarrow}). \quad (2.40)$$

In contrast to the charge gap the excitation here varies the total spin while keeping the total number of charges unchanged. This gap is seen in the dynamical spin structure factor which is probed in experiments such as inelastic neutron-scattering. The third gap is the single-particle gap defined as

$$E_p = E_0(N_{\uparrow} + 1, N_{\downarrow}) + E_0(N_{\uparrow} - 1, N_{\downarrow}) - 2E_0(N_{\uparrow}, N_{\downarrow}). \quad (2.41)$$

This excitation is characterized by changing both, total number of charges and total spin. This gap is seen in the single-particle spectral function probed in experiments such as angle resolved photoemission spectroscopy. These three gaps have been calculated for several values of the on-site interaction  $U$ , rung hopping  $t_{\perp}$  and system length  $L$ .

### 2.3.2 Excitation energies at half filling

The charge gap is plotted in Figure 2.7(a) as a function of the rung hopping  $t_{\perp}$  for finite length  $L = 128$  and three values of the on-site interaction  $U$ . Interestingly, the behavior



of the charge gap is qualitatively similar to the Hartree-Fock gap  $E_{\text{HF}}$  seen in Fig. 2.6. However, one can distinguish between four regions by increasing the rung hopping. At very small  $t_{\perp}$ , a small charge gap can be observed which scales as  $\propto 1/L$  due to finite-size effects. The finite-size scaling is performed by calculating the charge gap for ladder lengths from  $L = 20$  to  $L = 200$  and extrapolating the gaps to  $L \rightarrow \infty$ . As it is shown in Fig. 2.8(a), the extrapolation to the thermodynamic limit indicates a gapless phase for this region. Inside this region the charge gap seems to vanish as  $E_c \approx ct_{\perp}/L$  with a prefactor  $c \approx 6$ . As a comparison, the exact scaling for a half-filled tight-binding chain is  $E_c \approx 2\pi t_{\perp}/L$ . Thus this scaling also confirms that added charges (electrons or holes) go primarily to the Fermi leg and that the inter-chain hopping  $t_{\perp}$  barely affects low-energy charge excitations in the limit of weak  $t_{\perp}$ , see Sec. 2.1.3. The second region, is characterized by a quadratic increase of the charge gap with respect to  $t_{\perp}$ . The quadratic behavior suggests a fitting with a function of the form  $f(t_{\perp}) = a + b\frac{4t_{\perp}^2}{U}$ . The results agree well with such a fitting and give a slope  $b$  which increases from  $b \approx 1.1$  for  $U = 5$  to  $b \approx 1.5$  for  $U = 20$ . This quadratic scaling of the charge gap with  $t_{\perp}$  relates the gap opening to the effective rung exchange coupling  $J_{\perp} \propto t_{\perp}^2$  discussed in Sec. 2.1.2 and 2.1.3. According to the fitting, the intercept  $a$  is negative which indicates a possibility of gap closing at small but finite rung hopping. The critical coupling  $t_{\perp}^c(U)$  where the gap close fulfills the condition  $f(t_{\perp}^c) = 0$ . The results for the critical coupling are  $t_{\perp}^c(U = 20t_{\parallel}) \approx 0.8$ ,  $t_{\perp}^c(U = 8t_{\parallel}) \approx 0.3$ , and  $t_{\perp}^c(U = 5t_{\parallel}) \approx 0.1$ . The charge gap in the third region saturates or takes a non-monotonic behavior at intermediate values of  $t_{\perp}$ . In the fourth region the linear scaling of the charge gap with respect to  $t_{\perp}$  is clear and approaches the value of the band gap Eq.(2.7) for large enough  $t_{\perp}$  as expected from the limiting cases analysis in Sec. 2.1.1 and 2.1.4. In general, the results  $E_c$  confirm that it remains finite in the thermodynamic limit for all ( $U > 0, t_{\perp} > 0$ ) excepted for the previously mentioned small region of weak rung hopping which roughly corresponds to  $t_{\perp} < t_{\perp}^c(U)$ .

The single-particle gap is found to be equal to the charge gap for weak and strong rung hopping but enhances clearly, in comparison to the charge gap, for intermediate values of  $t_{\perp}$ . The difference

$$E_{\text{pb}} = 2(E_{\text{p}} - E_c) \quad (2.42)$$

is called the pair binding energy which is the energy needed to break a bound pair of electrons. In Fig. 2.7(d) significant enhancement of pair binding energy is observed in a region which corresponds roughly to the third region defined above, e.g. for moderate on-site interactions  $U = 8$  and rung hopping  $0.8t_{\parallel} < t_{\perp} < 2$ . The pair binding energy is very small or negative in the other three regions and vanishes in the thermodynamic limit while analysis of the finite-size effects confirm that this pair binding energy remains finite in the thermodynamic limit for the third region, see Fig. 2.9.

The spin gap behavior is shown as a function of the model parameters  $U$  and  $t_{\perp}$  in Fig. 2.7(b). It has roughly a similar qualitative behavior as the charge gap although the second and third regions show much less similarity. As expected in the fourth region with large enough  $t_{\perp}$ ,  $E_s$  approaches the value of the band gap Eq.(2.7) similar to the  $E_c$  discussed before. However, the spin gap is generally very small in comparison to the charge gap for smaller values of rung hopping.

The finite-size scaling analysis of the numerical results show finite values of the spin gaps in the thermodynamic limit for all ( $U > 0, t_{\perp} > 0$ ) except for the small region at weak rung hopping  $t_{\perp} = t_{\perp}^c(U)$  where the spin gap vanishes as  $E_s \approx c_s t_{\perp}/L$ , see Figs. 2.9

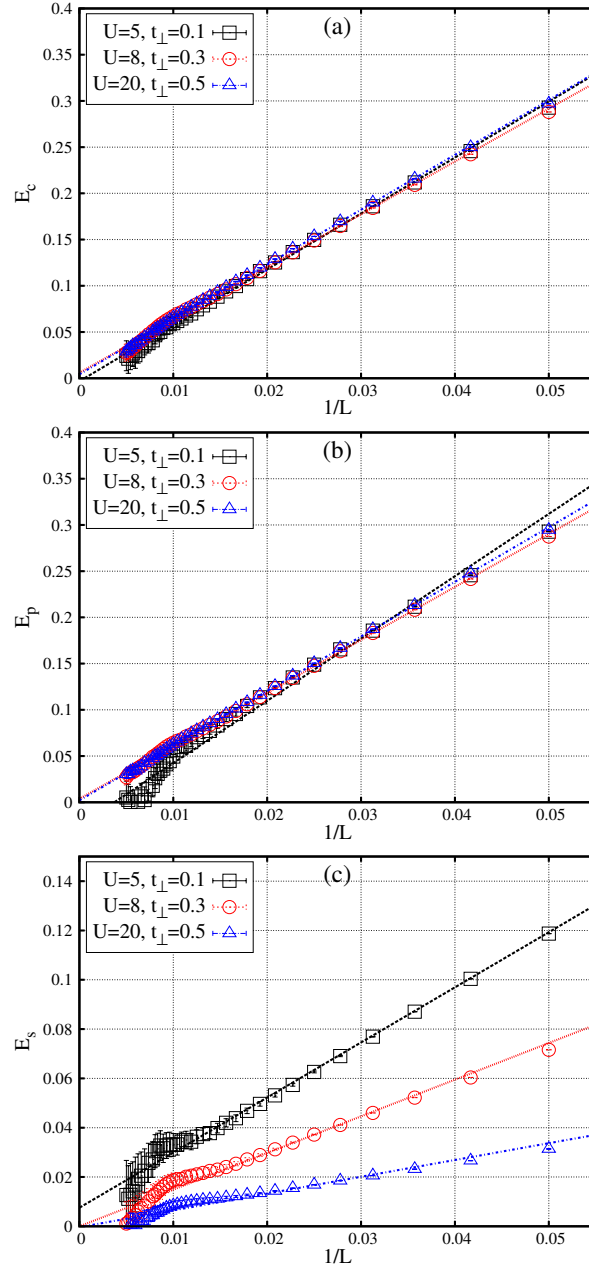


Figure 2.8: Gaps of the half-filled asymmetric Hubbard ladder (2.1) as a function of the inverse ladder length  $1/L$ : (a) charge gap ( $E_c$ ), (b) single-particle gap ( $E_p$ ), and (c) spin gap ( $E_s$ ).

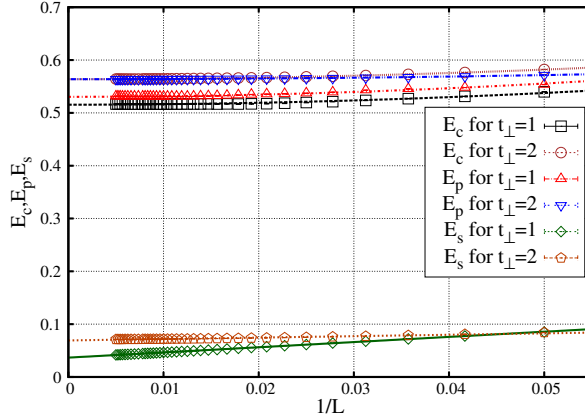


Figure 2.9: Charge gap ( $E_c$ ), single-particle gap ( $E_p$ ), and spin gap ( $E_s$ ) of the half-filled asymmetric Hubbard ladder (2.1) as a function of the inverse ladder length  $1/L$  for  $U = 8$ ,  $t_\perp = 1$  and 2.

and 2.8(c). The prefactor (the spin velocity)  $c_s$  extracted from the DMRG data, i.e.  $c_{\text{DMRG}}$ , agrees well with the exact results for the same prefactor calculated using the Bethe Ansatz (BA) method, i.e.  $c_{\text{BA}}$ , for the one-dimensional Hubbard model on an open chain [11]. For  $(U = 5, t_\perp = 0.1)$  one gets  $c_{\text{DMRG}} \approx c_{\text{BA}} \approx 2.23$ , and for  $(U = 8, t_\perp = 0.3)$  one gets  $c_{\text{DMRG}} \approx 1.49$  and  $c_{\text{BA}} \approx 1.51$ . For a strong on-site interaction  $(U = 20, t_\perp = 0.5)$  one gets  $c_{\text{DMRG}} \approx 0.681$  and  $c_{\text{BA}} \approx 0.637$ . This agreement between DMRG and BA results confirms that in the limit of weak  $t_\perp$  (i.e. the chain limit, see Sec. 2.1.3) the lowest triplet excitation is essentially a spin excitation in the Hubbard leg and it is barely affected by the inter-chain hopping  $t_\perp$ .

The difference in finite-size prefactors of charge and spin gaps indicates the dynamical spacial spin-charge separation, i.e., different charge and spin excitations in separate legs, in the infinite ladder system. In this gapless phase, the finite size extrapolation of the single-particle gap has strong uneven behavior. It scales very similar to the charge gap extrapolation as shown in Figs. 2.8(a), (b) and 2.10. This behavior contradicts the behavior of the one-dimensional Hubbard model in which the single-particle velocity is the average value of both charge and spin velocities. This indicates the localization of the single-particle excitation on the Fermi leg and, hence, the absence of electron-electron correlation in it. This behavior suggests an effective decoupling between the Hubbard and Fermi legs. The spacial spin-charge separation is characterized by this effective decoupling.

To summarize the study of excitation energies of the asymmetric ladder at half-filling, four different phases have been distinguished within the parameter space ( $U > 0, t_\perp > 0$ ). The first phase is for small enough  $t_\perp$  and has at least three gapless modes, one for charge excitations, one for spin excitations and one for single-particle excitations. This phase is classified within the Luttinger liquid universality due to the differences between the calculated charge and spin velocities. However, the behavior of the single-particle excitations reveals almost equal charge and single-particle velocities which imply an effective decoupling between the Hubbard and Fermi legs. In this case the Fermi leg behaves almost as a 1D tight-binding chain with gapless spin and charge excitations but the Hubbard leg behaves almost as a 1D Hubbard chain at half filling with gapped charge excitations and

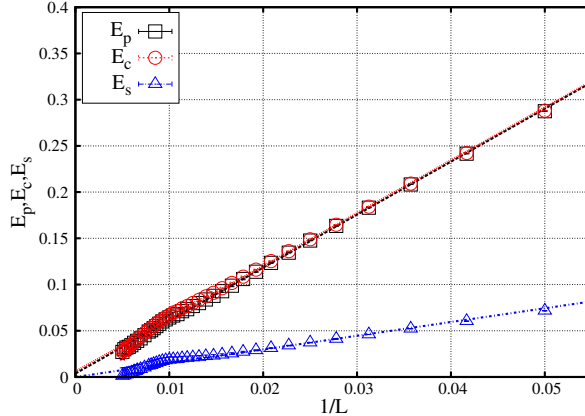


Figure 2.10: Charge gap ( $E_c$ ), single-particle gap ( $E_p$ ), and spin gap ( $E_s$ ) of the half-filled asymmetric Hubbard ladder (2.1) as a function of the inverse ladder length  $1/L$  for  $U = 8$  and  $t_\perp = 0.3$ . This figure is adapted from Ref. [63].

gapless spin excitations. The second phase corresponds to the aforementioned Kondo-Mott phase, (see Sec 2.1.2). This phase is characterized by gapped charge excitations with a gap that increases quadratically with  $t_\perp$  and linearly with an effective rung exchange coupling  $J_\perp$ . Much smaller spin gapped excitations exist as well. The scaling of the spin gap is less clear than the charge gap. The charge gap is much larger than the spin gap in the third phase. However, both of them have a non-monotonic behavior. The character of this phase is a finite pair binding energy with the same order of magnitude as the spin gap. Pair-binding energies have been found in the symmetric Hubbard two-leg ladders [14] which is classified as a spin-gapped paramagnetic Mott insulator. However, the spin gap of the asymmetric ladder in the third region is much smaller than it is in the symmetric ladder for the same Hubbard interaction  $U$ . However, the classification of the third phase as a spin-gapped Mott insulating phase is in consistence with the analysis in Sec.2.1.1. Finally, the fourth phase is a correlated band insulator for large enough  $t_\perp$ . Both charge and spin gaps are essentially given by the band gap Eq.(2.7). The onset of this phase is at  $t_\perp = 2$  in the weak-coupling limit (Sec. 2.1.1) and increases to larger rung hoppings for stronger interactions  $U$ . It is important to emphasize that DMRG results for excitation gaps distinguish only between gapless and gapped phases. The classification of the other phases is inspired, so far, by the analysis of limiting cases and the Hartree-Fock calculations.

### 2.3.3 Density profiles

DMRG offers the possibility to measure local observables using the calculated target state. Much more insights in the asymmetric ladder at half filling is gained by investigating the charge and spin densities. The definition of the charge density is

$$N(x, y) = \langle n_{x,y,\uparrow} + n_{x,y,\downarrow} \rangle, \quad (2.43)$$

and that of the spin density is

$$S(x, y) = \langle n_{x,y,\uparrow} - n_{x,y,\downarrow} \rangle. \quad (2.44)$$

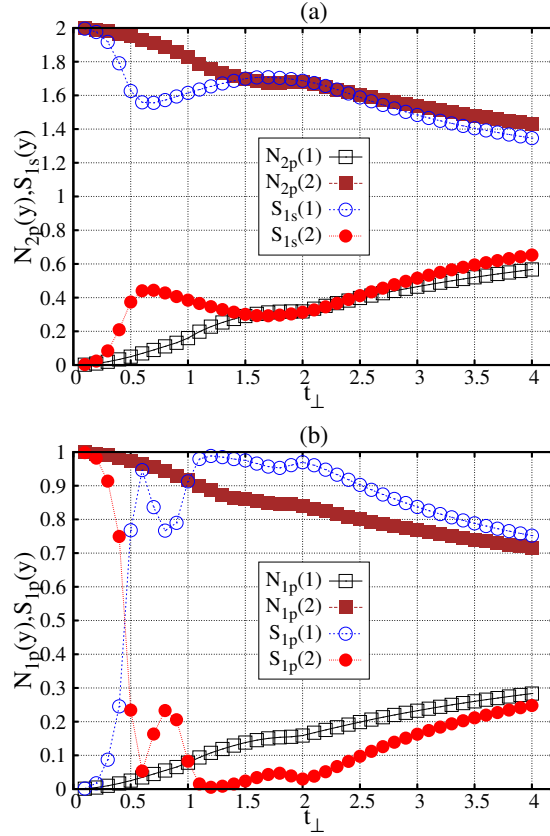


Figure 2.11: The total charge (2.45) and spin (2.46) density deviations on the Hubbard leg with  $U = 8$  (open symbols) and the Fermi leg (solid symbols) as a function of the inter-leg hopping  $t_{\perp}$ : (a)  $N_{2p}(y)$  for two added electrons (squares) and  $S_{1s}(y)$  for one spin triplet excitation (circles). (b)  $N_{1p}(y)$  (squares) and  $S_{1p}(y)$  (circles) for one added electron. These figures are adapted from Ref. [63].

Both of them exhibit a uniform structure at half filling with  $N(x, y) = 1$  and  $S(x, y) = 0$  for any value of  $U$  and  $t_{\perp}$ . However, more information could be inferred from the half filled asymmetric ladder with charge, spin or single-particle excitations. The excess charge density due to these excitations is calculated by

$$N_m(y) = \sum_x N(x, y) - L_x \quad (2.45)$$

and the excess spin density is calculated using

$$S_m(y) = \sum_x S(x, y) \quad (2.46)$$

where the subscript  $m$  refers to the two-particle ( $m = 2p$ ), spin-triplet ( $m = 1s$ ) and single-particle ( $m = 1p$ ) excitations.

Figure 2.11(a) shows the total density  $N_{2p}(y)$  of the excess charge due to the two-particle excitation and the total density  $S_{1s}(y)$  of the excess spin due to the triplet excitation in each leg separately with respect to  $t_{\perp}$  for  $U = 8$ . The distribution of  $N_{2p}(y)$  and  $S_{1s}(y)$  between the two legs indicates that the additional two charges go mostly to the Fermi leg but the spin triplet excitations go mostly to the Hubbard leg. However, for small  $t_{\perp}$  that corresponds to the Luttinger liquid phase the additional charge is almost entirely on the Fermi leg while the excess spin is almost entirely on the Hubbard leg. This an uneven behavior for the spin excitation is due to the existence of gapless spin excitation in both the Hubbard and the Fermi leg. This is explained by the smaller spin velocity in the 1D Hubbard model in comparison to single chain tight-binding model at half filling and due to the effective decoupling between the two legs which will be discussed next. The single-particle excitation reveals a different behavior in Fig 2.11(b). While the total density  $N_{1p}(y)$  of the excess charge goes mostly to the Fermi leg, the total density  $S_{1s}(y)$  of the excess spin shows unusual behavior. For small values of  $t_{\perp}$ , which corresponds to the Luttinger liquid phase,  $S_{1s}(y)$  goes primarily to the Fermi leg. Then it reduces but fluctuates on the Fermi leg for parameters corresponding to the Kondo-Mott phase. For the spin-gapped Mott insulating and the correlated band insulating phases it behaves similarly to  $S_{2s}(y)$ . These behaviors confirm the effective decoupling between the Hubbard leg and the Fermi leg in the Luttinger liquid phase making the single-particle excitation localized primarily in the Fermi leg.

Figures 2.12 - 2.15 show distributions of the charge  $N(x, y)$  and spin  $S(x, y)$  densities due to the charge, spin-triplet and single-particle excitations. In Fig. 2.12(a) one can see a strong oscillation in the charge density within the Fermi leg for parameters  $U = 8$  and  $t_{\perp} = 0.5$ , i.e. in the Kondo-Mott phase. For  $U = 8$  and  $t_{\perp} = 1$  that corresponds to the spin-gapped Mott insulator phase, the distribution of the charge density shows a single wave packet although the excitation is due to additional two particles. Although this single wave packet breaks the reflection symmetry around the center of chain, it confirms the tendency of pair binding that has been discussed in the spin-gapped Mott insulating phase. The breaking of reflection symmetry indicates a degeneracy of odd and even excitations given that the possibility of phase separation is excluded due to the uniform distribution for density profile by adding more charges to the ladder system, see Sec 2.3.4. This single wave packet breaks into two-peak wave packet, which preserves reflection symmetry around the center of chain, for  $U = 8$  and  $t_{\perp} = 2$ . This case corresponds to the

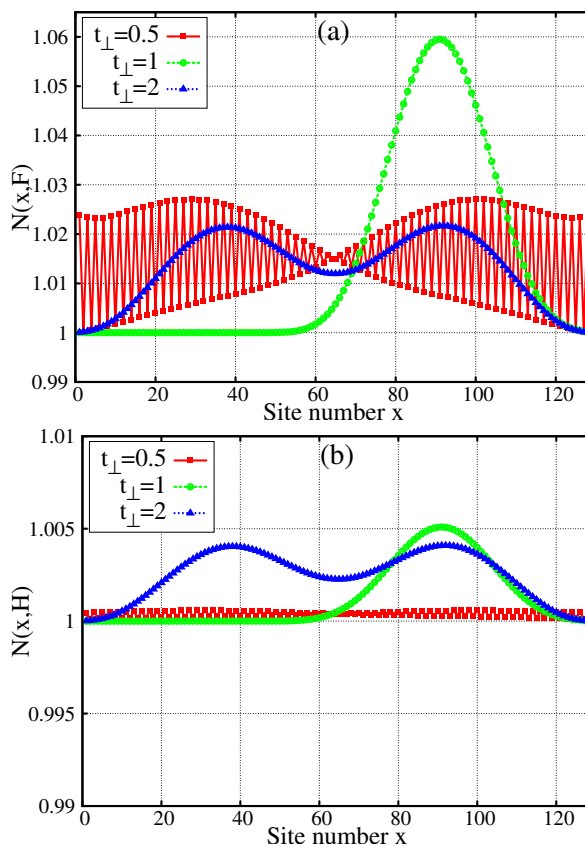


Figure 2.12: Distribution of the charge density (2.43) on (a) the Fermi leg and (b) the Hubbard leg, for two electrons added to the half-filled asymmetric ladder, Eq.(2.1), with  $U = 8$  and three values of  $t_{\perp}$ . Figure (a) is adapted from Ref. [47].

correlated band insulator phase. The same three different profiles are seen in Fig. 2.12(b) for the Hubbard leg but with smaller density amplitudes. Fig. 2.15 shows the spin density distribution of the spin excitation. Fig. 2.15(a) and (b) have the same profiles but with much more density on the Hubbard leg than in the Fermi leg. For  $t_{\perp} = 0.5$ , which is associated to the Kondo-Mott phase, one sees strong regular oscillations. For  $t_{\perp} = 1$  and 2, a single wave packet is observed for both cases, i.e. within the spin-gapped Mott insulating and correlated band insulating phases. Fig. 2.13 shows the charge density distribution of single-particle excitation. A strong oscillation in the density distribution is seen in Fig. 2.13(a) for  $t_{\perp} = 0.5$  but with an irregular profile on the Fermi leg. A single wave packet is seen for  $t_{\perp} = 1$  but with a modulated irregular oscillation in the density distribution. For  $t_{\perp} = 2$ , one sees a single wave packet in the density distribution. Again, similar density profiles to Fig. 2.13(a) are seen in Fig. 2.13(b) with weaker densities on the Hubbard leg. Fig. 2.14(b) shows the spin density distribution of the single-particle excitation on the Hubbard leg. The spin density profile reveals strong irregular density oscillations for  $t_{\perp} = 0.5$ . For  $t_{\perp} = 1$ , there are also irregular oscillations but with much more weaker density amplitudes distributed along the chain. For  $t_{\perp} = 2$ , a very weak single wave packet is revealed. The same is revealed in Fig. 2.14(a) for the measurements done on the Fermi leg except for  $t_{\perp} = 2$  where the density distribution is almost uniform. It is clear that the charge and spin density distributions of single-particle excitations are

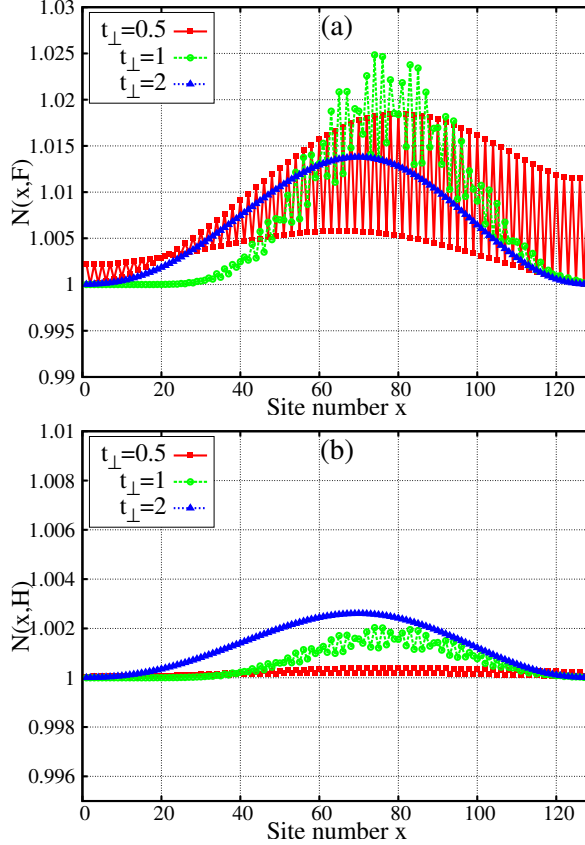


Figure 2.13: Distribution of the charge density (2.43) on (a) the Fermi leg and (b) the Hubbard leg, for one electron added to the half-filled asymmetric ladder, Eq.(2.1), with  $U = 8$  and three values of  $t_{\perp}$ .

different from their equivalent charge density distribution of the two particle excitation and spin density distribution of the spin triplet excitation. These results are reflected in the Fourier transform as following.

The Fourier transform of charge and spin density distributions can provide a closer insight into the aforementioned excitations. It is defined as

$$\tilde{O}(k, y) = \frac{1}{\sqrt{L}} \left| \sum_{x=1}^L O(x, y) \exp(-ikx) \right| \quad (2.47)$$

where  $k = 2\pi z/L$  with  $z$  is an integer governed by  $|z| < L/2$ .  $\tilde{O}(k, y) \equiv \tilde{N}(k, y)$  for the charge density measurements or  $\tilde{O}(k, y) \equiv \tilde{S}(k, y)$  for spin density measurements. The Fourier transform of the two-particle excitation added to the half-filled asymmetric ladder at  $U = 5$  are plotted for the Fermi leg in Fig. 2.16(a). They show strong peak at  $k = 0$  which is apparently due to the finite uniform density distribution at half-filling. The residual spectral weight corresponds to charge excitation which moves its highest peak by changing  $t_{\perp}$ . For  $t_{\perp} = 0.5$ , the maximum of the residual peak concentrates at  $k = \pi$ . Then it moves to  $0 < |k| < \pi$  for  $t_{\perp} = 1$  and  $1.5$  before it vanishes at  $t_{\perp} = 2$ . The implications of this behavior can be understood by assuming a wave number  $k_g$  for the lowest single-particle excitation, see Fig. 2.2(b). This wave number can be related



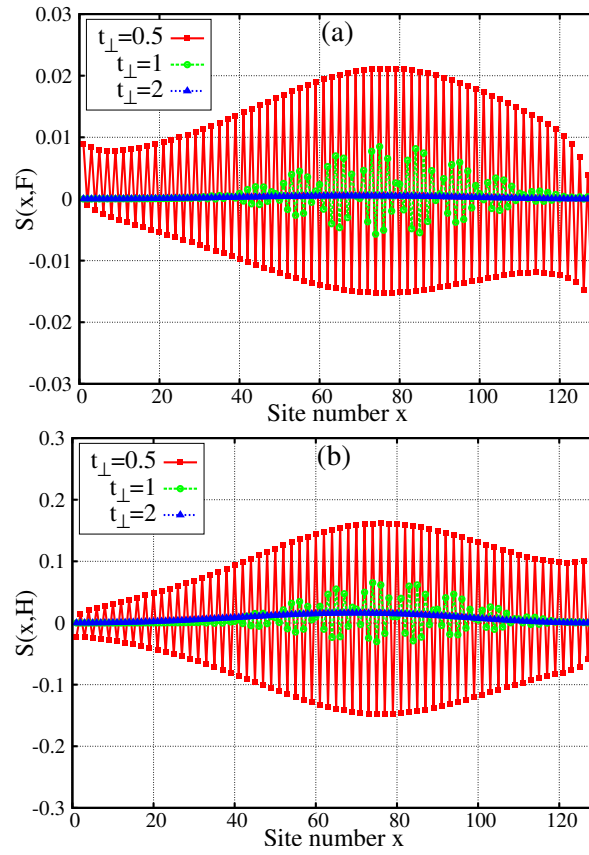


Figure 2.14: Distribution of the spin density (2.44) on (a) the Fermi leg and (b) the Hubbard leg, for one electron added to the half-filled asymmetric ladder, Eq.(2.1), with  $U = 8$  and three values of  $t_{\perp}$ .

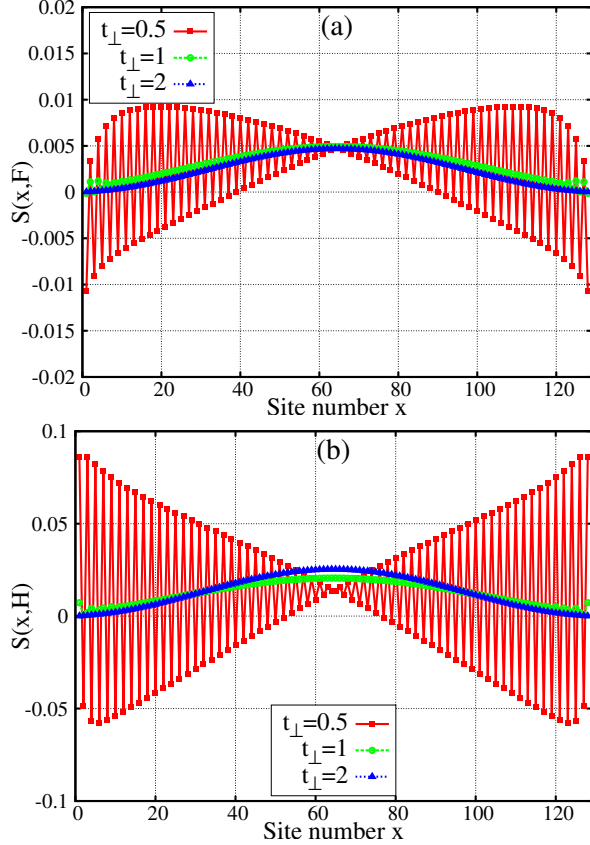


Figure 2.15: Distribution of the spin density (2.44) on (a) the Fermi leg and (b) the Hubbard leg, for a spin-triplet excitation on the half-filled asymmetric ladder, Eq.(2.1), for  $U = 8$  and three values of  $t_{\perp}$ .

to the wave vector of the two-particle excitation in Fig. 2.16(a) using  $k = \pm 2k_g \text{ mod } 2\pi$ . In this case,  $k_g = \pi/2$  in the second phase and  $k_g = 0$  or  $\pi$  in the fourth phase while it implies an incommensurate values of  $k_g$  in the third phase. The Fourier transforms of the spin density for the triplet excitation show similar behavior to the two-particle excitation [Fig. 2.16(c)]. The same is applied in the Fourier transforms of the spin density for the single-particle excitation [Fig. 2.16(d)]. Similar behaviors are revealed in the Fourier transforms of charge density for the single-particle excitation [Fig. 2.16(b)] except for  $t_{\perp} = 1$  where two residual peaks appear instead of one, which is apparently due to the modulated oscillation described in Fig. 2.13.

In general, these results agree with the analysis of the limiting cases in Sec. 2.1. In particular, DMRG calculations confirm the prediction of spin-gapped Mott insulator with incommensurate wave number excitations in the weak interaction limit. In the chain limit, DMRG calculations show that the gap opens due to the perfect nesting of Fermi points  $k_F = \pm \frac{\pi}{2}$  but for large enough  $t_{\perp}$  values that can destroy the gapless Luttinger liquid phase. However, as it has been mentioned before, these two limits need analytical investigations using field theoretical methods. For the dimer limit, DMRG shows a correlated band insulator for large inter-chain coupling with the excitation wave number  $k = 0$  or  $\pi$  in agreement with the limiting case analysis. More surprising is the presence of three gapped phases with low-energy excitations distinguished by lowest-energy

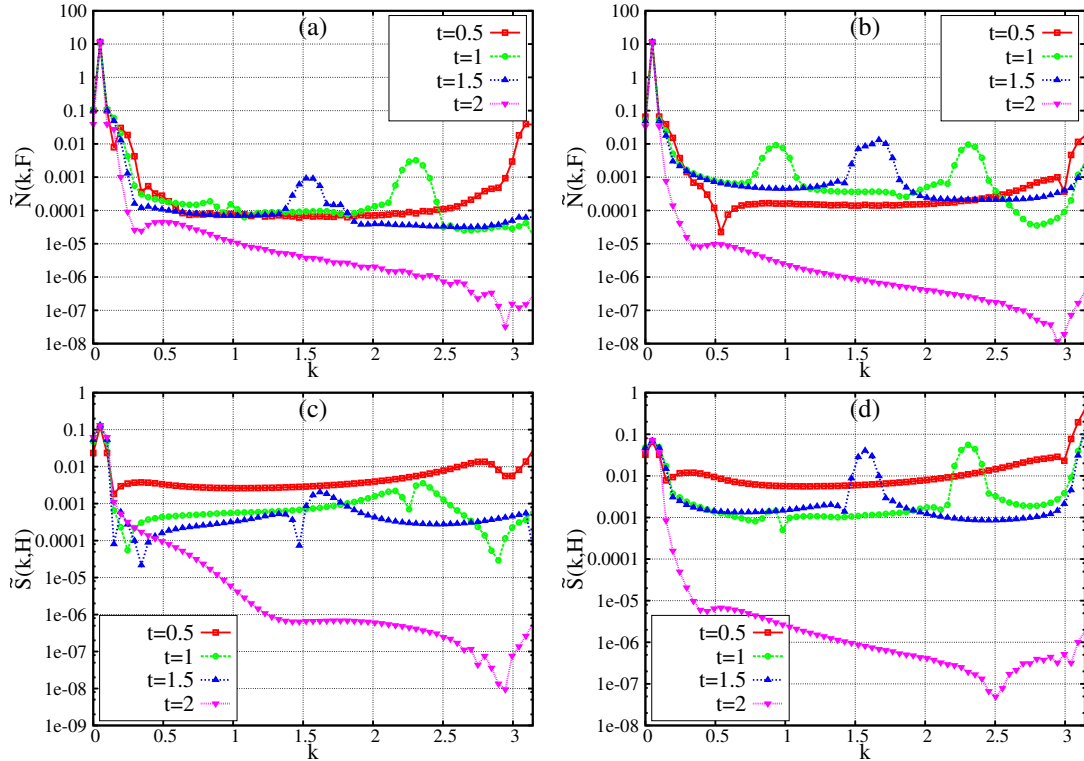


Figure 2.16: Fourier transform for the distribution of the charge density (2.43) on the Fermi leg: (a) with two additional electrons and (b) with one additional electron, both to the half-filled ladder Eq.(2.1). These two figures are adapted from Ref. [47]. Fourier transform for the spin density (2.44) on the Hubbard leg: (c) with spin triplet excitation and (d) with one additional electron. The calculations are done for  $U = 5$ .

excitation wave numbers that matches qualitatively the observation seen in the Hartree-Fock approximation as discussed in Sec. 2.2. However, it should be emphasized that the Hartree-Fock approximation is otherwise quite inaccurate as it predicts an antiferromagnetic Mott insulator or a band insulator with antiferromagnetic long-range order for all ( $U > 0, t_{\perp} > 0$ ), while the (almost exact) DMRG results confirm the absence of any antiferromagnetic long-range order and reveal the existence of a fourth gapless phase as well.

### 2.3.4 Correlation functions and ladder doping

Various correlation functions have been investigated including density-density, spin-spin and pair density wave (PDW) correlations in order to get more insight in the asymmetric ladder phases discussed before. The DMRG method calculate correlation functions accurately for finite lengths with open boundary conditions [14, 46, 72, 67]. However, the asymptotic behavior can not be inferred directly unless using a priori knowledge or hypothesis about the system. Density-density correlation functions are defined by

$$C_c^{\alpha}(m) = \langle N(x_0, y)N(x_0 + m, y') \rangle - \langle N(x_0, y) \rangle \langle N(x_0 + m, y') \rangle \quad (2.48)$$

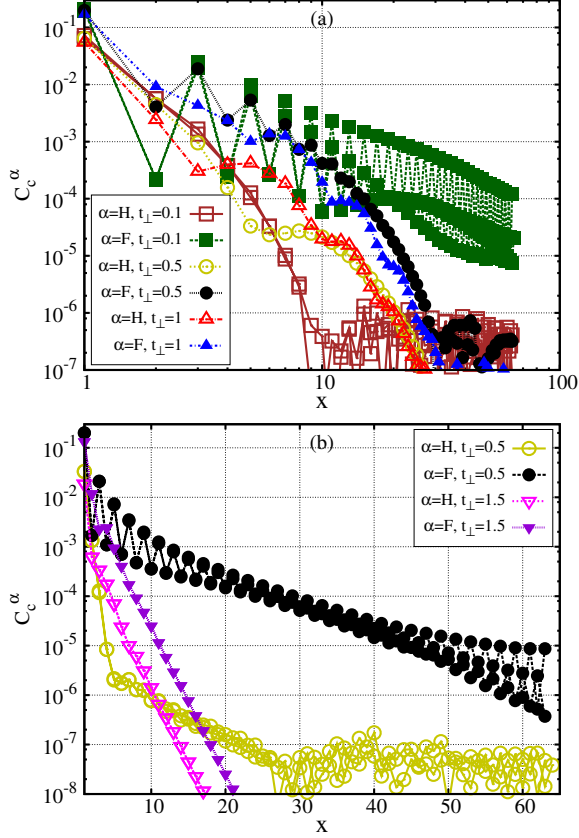


Figure 2.17: Absolute values of the intra-leg density-density correlations (2.48) in the asymmetric half-filled Hubbard ladder Eq.(2.1) at (a)  $U = 5$  and (b)  $U = 8$  for different values of the rung hopping  $t_{\perp}$ . Open symbols indicate correlations in the Hubbard leg and filled symbols in the Fermi leg. These figures are adapted from Ref. [63].

where  $x_0 = \frac{L}{2}$ . The intra-leg correlations in the Fermi leg are defined for  $y = y' = F$  and denoted by  $\alpha = F$ . Similarly, in the Hubbard leg they are defined for  $y = y' = H$  and denoted by  $\alpha = H$ . The inter-leg correlations are denoted by  $\alpha = \perp$  and defined for  $y \neq y'$  but they are found to be weaker than the intra-leg correlations and, hence, they are not discussed here. Similarly spin-spin correlation functions are defined by

$$C_s^{\alpha}(m) = \langle S(x_0, y)S(x_0 + m, y') \rangle. \quad (2.49)$$

Both correlation functions are depicted in Figs. 2.17 and 2.18. The double logarithmic scale is used for Figs. 2.17(a) and 2.18(a) while semilogarithmic scale is used for Figs. 2.17(b) and 2.18(b). For  $U = 5$  and  $t_{\perp} = 0.1$  in Figs. 2.17(a) and 2.18(a), both spin-spin and density-density correlations exhibit similar power-law decay in the Fermi leg. This parameter set corresponds to the Luttinger liquid phase. The Hubbard leg exhibits a power-law decay with an exponent close to -1 for the spin-spin correlations but exponential decay for the density-density correlations for the same parameter set. The Fermi leg shows correlations in the nature of the 1D tight-binding chain while the Hubbard leg displays correlations similar to the 1D Hubbard model at half filling. This supports the interpretations of the gap extrapolations and the distributions of excitation densities which reveal an effective decoupling between the two legs. The behavior of

correlation functions in this phase suggests that the single-particle excitations retain a Fermi liquid nature or almost uncorrelated features despite the finite inter-leg coupling. However, the other two intermediate phases, i.e. the Kondo-Mott and the incommensurate Mott insulating phases, show complex behaviors. The density-density correlations in Figs. 2.17(a) decay exponentially for  $U = 5$  and  $t_{\perp} = 0.5$  in both legs. This is in consistency with the gap opening in the charge sector of the Kondo-Mott phase. The spin-spin correlations show an apparent power-law decay for the same parameter set. Power-law decay is a feature of gapless excitations which contradicts the finite spin gaps found in this phase. Nevertheless, this contradiction can be explained by the small values of the spin gaps found for this phase. Gaped phases are characterized by exponential decay in the corresponding correlation functions. This means that the apparent power-law decay is in fact a slow exponential decay with a correlation length much larger than the ladder length. A long correlation length is seen in the density-density correlations on the Fermi leg in Fig. 2.17(b) for  $U = 8$  and  $t_{\perp} = 0.5$  which corresponds to the Kondo-Mott phase as well. This long correlation length is due to the reduction of the charge gap seen in Fig. 2.7(a) in comparison to  $U = 5$  and  $t_{\perp} = 0.5$ . The density-density correlations decay faster in the Hubbard leg for this case. This implies the existence of the lowest charge excitations in the Fermi leg. The influence of the gap on the correlation length is seen in the spin-gapped Mott insulating phase by comparing the spin correlations in Figs. 2.18(a) and (b). For  $U = 5$  and  $t_{\perp} = 1$  in Fig. 2.18(a) the spin-spin correlation has apparent power-law decay associated to the small spin gap seen in Fig. 2.7(b). The spin gap is enhanced for  $U = 8$  and  $t_{\perp} = 1.5$  in Fig. 2.7(b) which illustrates the slow exponential decay seen in Fig. 2.18(b). This indicates that the apparent power-law decay in Fig. 2.18(a) is in fact an exponential decay with correlation length larger than the ladder length. The density-density correlations decay exponentially in the spin-gapped Mott insulator as seen in Fig. 2.17(a) and (b) for  $U = 5$  and  $t_{\perp} = 1$  as well as for  $U = 8$  and  $t_{\perp} = 1.5$ . The amplitude of the correlation in this case is slightly larger in the Fermi leg. This is seen for the Kondo-Mott phase as well. Figs. 2.17 and 2.18 show that spin-spin correlations have weaker amplitudes in the Fermi leg for the Kondo-Mott phase and the spin-gapped Mott insulating phase. Both density-density and spin-spin correlations decay exponentially and similarly in the correlated band insulating phase.

The complex behavior of density-density and spin-spin correlations in the Kondo-Mott and the spin-gapped Mott insulating phases can be explained as an influence of an induced exchange coupling  $J \sim t_{\perp}^2/U$  between the two legs. This exchange coupling induces charge gap in the Fermi leg as well as spin-spin correlations. By increasing the Hubbard interaction  $U$  the exchange coupling  $J$  becomes smaller which reduces the influence on the Fermi leg and, hence, reduces the charge gap. Increasing the Hubbard interaction  $U$  also gives slower decay of the density-density correlations in the Fermi leg comparing to the Hubbard leg. The small exchange coupling  $J$  gives even smaller spin gaps. This illustrates the difference between this model and the Kondo-Heisenberg model studied in Ref. [59], where the authors used large values of exchange couplings that give substantial spin gap at half filling. However, the spin gap and correlations agree qualitatively with the half filled one-dimensional Kondo-Heisenberg model studied in Ref. [73] where for weak spin exchange parameter a long correlation length has been estimated for small spin gap. The spin-spin correlations were studied before in Ref. [48] for parameters correspond to the Kondo-Mott phase. The main findings were nonmonotonic

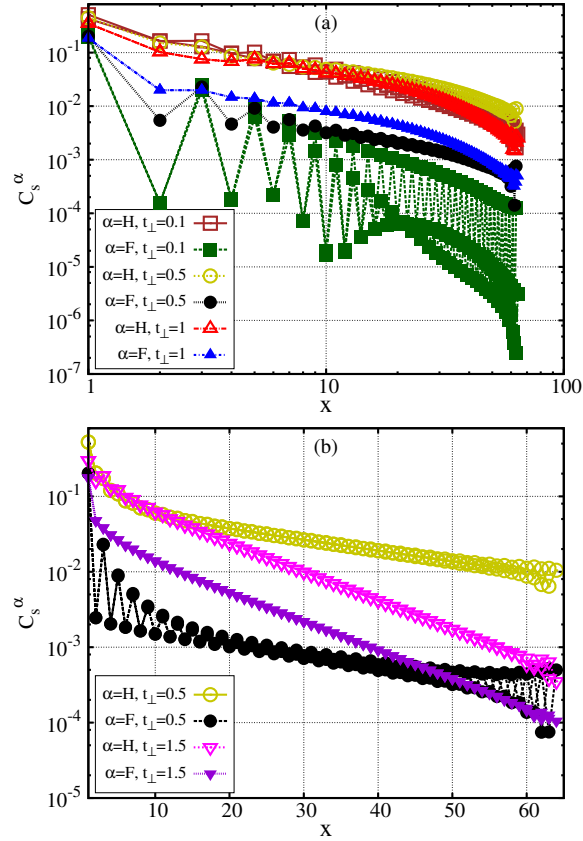


Figure 2.18: Absolute values of the intra-leg spin correlations (2.49) in the asymmetric half-filled Hubbard ladder Eq.(2.1) at (a)  $U = 5$  and (b)  $U = 8$  for different values of the rung hopping  $t_\perp$ . Open symbols indicate correlations in the Hubbard leg and filled symbols in the Fermi leg. These figures are adapted from Ref. [63].

behavior of the spin-spin correlations with respect to the Hubbard interaction  $U$ . These findings were explained there as a result of competition between the Hubbard interaction  $U$  and the induced rung exchange coupling. Nevertheless, the conclusion in Ref. [48] of gapless spin excitations is found to be wrong due to the long correlation length in the Kondo-Mott insulating phase. On the other hand, in comparison to the symmetric 2-leg Hubbard ladder [14], the asymmetric ladder has much more smaller spin gaps for similar values of  $U$  and  $t_{\perp}$  and the symmetric ladder shows clear exponential decay in the spin correlations.

Single-particle gap, spin gap and pair binding energies are calculated for low doped asymmetric ladders with intermediate values of on-site interaction and intermediate to strong chain coupling. The calculations of these gaps for doped ladders are motivated by questioning the fate of the pair binding energy upon doping. All these gaps tend to vanish for high doping as depicted in Fig. 2.19. In the same figure one can see an apparent monotonic increase of the single-particle and spin gaps versus doping as well as negative pair binding energies for strongly coupled chains. These non zero gaps in strongly coupled chains are due to finite size effects. For intermediate chain coupling, incommensurate single-particle excitation wave vectors appear in the Fourier transform profile but with more complex structure upon doping as seen in Fig. 2.20. For strong chain coupling, the asymmetric ladder shows one peak structure for  $k = 0$  for low and high doped ladders as seen in Fig 2.20 in consistence with the discussion of the dimer limit.

Several pair correlation functions have been calculated to clarify the structure of pairing in the incommensurate spin-gapped Mott-insulating phase. The asymmetric model (2.1) is related in some features to the symmetric 2-leg Hubbard ladder and in other features to the Kondo-Heisenberg model. These two models reveal tendency of pairing, in the form of the  $d$ -wave correlations for the symmetric 2-leg Hubbard model [14] and in the form of pair-density wave (PDW) in the Kondo-Heisenberg model [59]. The symmetric Hubbard model has dominant power-law  $d$ -wave correlations with exponent close to -2 [14], i.e. barely or without enhancement comparing to the  $U = 0$  case. The  $d$ -wave correlations are assumed to be less important in the asymmetric Hubbard ladder due to the bias of the charge excitation toward the Fermi leg. Other types of pair correlations (on-site, PDW, triplet-PDW, doublon-doublon, ...) were investigated for the half filled as well as for the lightly doped ladder. However, no enhancement in pair-correlations is found in the doped cases comparing to the noninteracting ladder. The most relevant pair correlation is the PDW correlation. The PDW correlations in two-leg ladder systems have attracted a lot of interest recently due to the observed anomalous properties in striped-order high-temperature superconductors which has been proposed to be illustrated using PDW correlations [59, 74, 67, 60]. This order parameter is motivated here by the general similarity between the asymmetric Hubbard ladder and the Kondo-Heisenberg model as it has been discussed in Sec. 2.1.2. This later model has been reported to have a spin-gapped phase with dominant quasi-long-range PDW pairing i.e., power-law with an exponent close to -1, in Ref. [59]. The definition of the PDW order parameter is

$$\Delta^{\dagger}(x, y) = \frac{1}{2} \left( c_{x,y,\uparrow}^{\dagger} c_{x+1,y,\downarrow}^{\dagger} - c_{x,y,\downarrow}^{\dagger} c_{x+1,y,\uparrow}^{\dagger} \right). \quad (2.50)$$

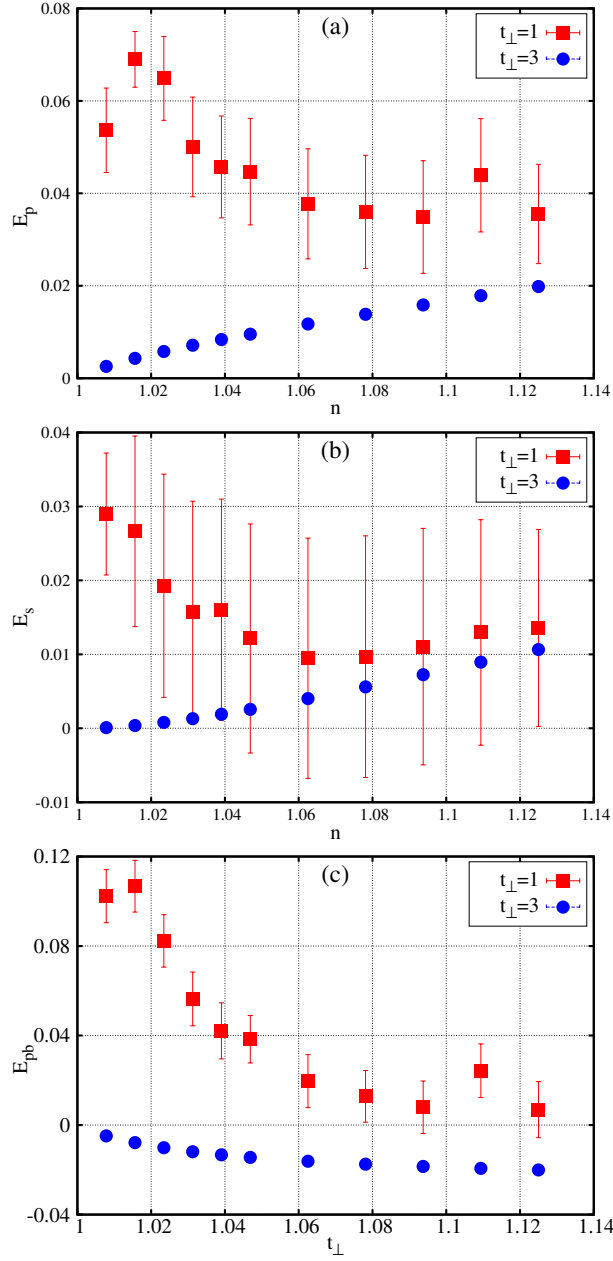


Figure 2.19: (a) Single-particle gap ( $E_p$ ), (b) spin gap ( $E_s$ ) and (c) pair-binding gap ( $E_{pb}$ ) as functions of the band filling,  $n = N/2L$ , for  $L = 128$ ,  $U = 5$  and two values of  $t_{\perp}$ . Figure (c) is adapted from Ref. [47].



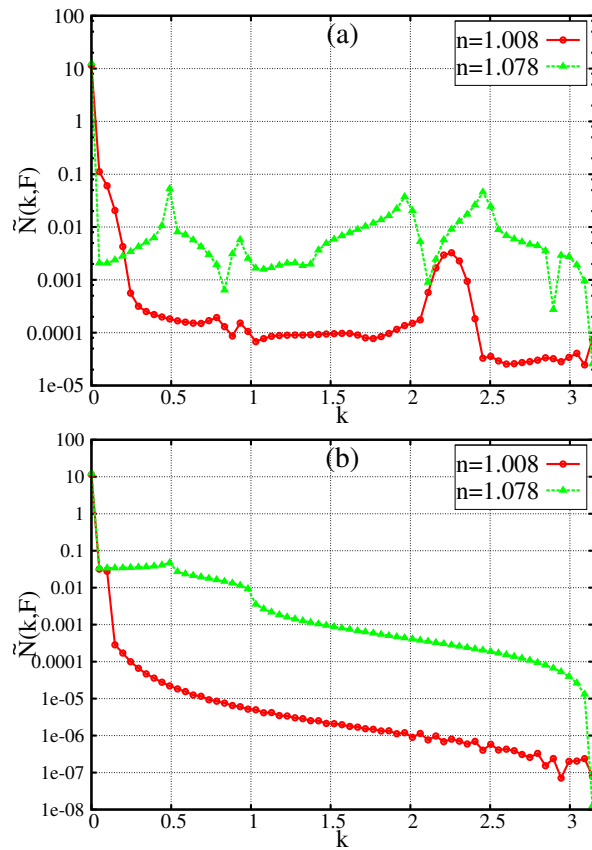


Figure 2.20: Fourier transform of the ground-state charge density on the Fermi leg for two different band fillings,  $n = N/2L$ , with  $U = 5$  and (a)  $t_{\perp} = 1$  and (b)  $t_{\perp} = 3$ .

Thus, the PDW correlation function is

$$C_{\text{PDW}}^\alpha(m) = \langle \Delta^\dagger(x_0, y) \Delta(x_0 + m, y') \rangle. \quad (2.51)$$

In contrast to the PDW in the Kondo-Heisenberg model [59], the measured PDW correlations in the low doped asymmetric ladder show power-law decay with exponents close to -2. This is demonstrated in Fig. 2.21 for the doped Mott insulating asymmetric phase. These results can not explain the finite pair-binding energy and the charge density profiles found in this phase. The dominant correlations is found to be power-law spin-spin correlations decaying with exponents close to -1 as seen in Fig. 2.21. The dominance of spin-spin correlations suggest that they compete with the PDW correlations. Nevertheless, it is difficult to decide if the power-law decay is real or apparent due difficulties in performing finite size analysis for the spin gap in the doped ladder. The density-density correlations decay similarly to the PDW correlations in the lightly doped asymmetric ladders. The discrepancy of these results with the Kondo-Heisenberg model can be explained by the discussion in Sec. 2.1.2 where the equivalence between the asymmetric Hubbard ladder and the Kondo-Heisenberg model is shown to be not exact unless the intra-chain hopping in the Hubbard leg is allowed to differ from its value in the Fermi leg. Furthermore, the spin exchange parameters used in Ref. [59] are of the order of  $t_{\parallel}$  and have no equivalent in the present study. For the half filled asymmetric ladder, the PDW correlations decay exponentially as depicted in Figs. 2.22(a) and (b) for the gapped Kondo-Mott and Mott insulating phases. However, the longest correlation length is found on the Fermi leg in the gapless phase while the shortest is in the gapless phase as well but on the Hubbard leg. The incommensurate spin gapped Mott insulating phase reveals similar correlation lengths on both Fermi and Hubbard legs but with a faster decay than in the Fermi leg in the gapless phase. The amplitude of correlations is weak in the Hubbard leg for the Kondo-Mott insulating phase.

The study of correlation functions support the effective decoupling between the Hubbard and Fermi legs in the gapless phase. On the other hand, the structure of pairing is not clarified despite the found finite pair-binding energy. The reason for this discrepancy is not known.

## 2.4 Comparison with Quantum Monte Carlo results

The three gapped phases are distinguished by elementary excitations with different wave vectors  $k_g$  using the analysis of the Hartree-Fock approximation in Sec. 2.2 and the profiles of excitation density calculated by DMRG in subsection. 2.3.3. These observations are further checked by calculating the momentum and energy-resolved single-particle spectral function which corresponds to the spectral functions probed by the angle-resolved photoemission spectroscopy experiment. The excitation wave vector  $k_g$  is determined by the sharp maxima of the spectrum [66, 75, 76]. The calculation of such spectral function using DMRG [75, 77, 76] has high computational cost. Therefore, a better way is to use the continuous-time interaction-expansion (CT-INT) quantum Monte Carlo (QMC) method [78]. The calculations presented here for the quantum Monte Carlo method were done by Martin Hohenadler. This method is based on a weak-coupling expansion in the interaction  $U$ , and gives exact results for finite systems and finite temperatures. A

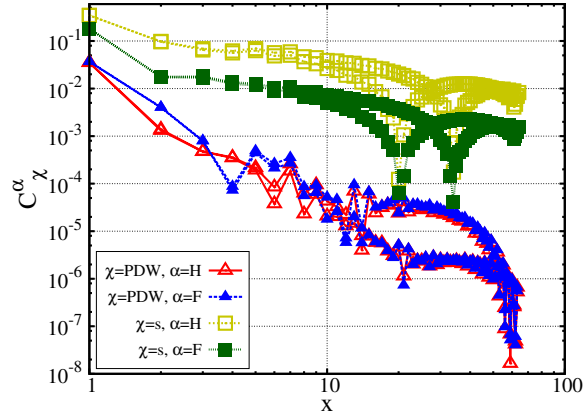


Figure 2.21: Absolute value of the intra-leg SDW and PDW correlation functions (2.49) and (2.51) in the asymmetric Hubbard ladder Eq.(2.1) doped away from half filling. The correlations are calculated for  $U = 5$  and  $t_{\perp} = 1$ . Open symbols display correlations in the Hubbard leg and filled symbols in the Fermi leg. This figure is adapted from Ref. [63].

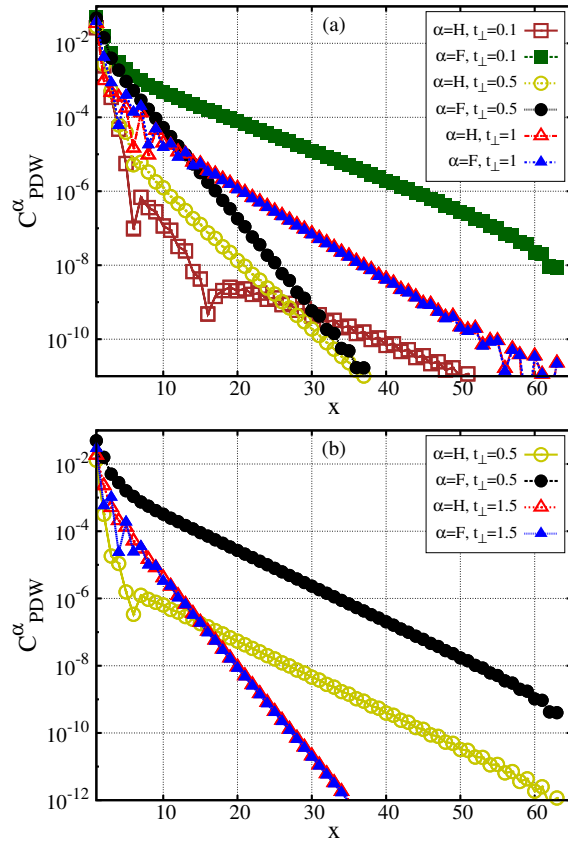


Figure 2.22: Absolute value of the intra-leg pair-density-wave correlation functions (2.51) in the half-filled asymmetric Hubbard ladder Eq.(2.1) for different values of  $t_{\perp}$  at (a)  $U = 5$  and (b)  $U = 8$ . Open symbols indicate correlations in the Hubbard leg and filled symbols in the Fermi leg. These figures are adapted from Ref. [63].

detailed review of the method can be found in Ref. [79]. For the present system, ladders with periodic boundary conditions along the legs are simulated. The calculations are done for  $L = 30$  and an inverse temperature  $\beta t_{\parallel} = 30$ . Thus, the single-particle spectral function

$$A(k, y, \omega) = \frac{1}{Z} \sum_{ij} |\langle i | c_{k,y,\sigma} | j \rangle|^2 (e^{-\beta E_i} + e^{-\beta E_j}) \times \delta(\Delta_{ji} - \omega). \quad (2.52)$$

is obtained. Here,  $c_{k,y,\sigma}$  is the Fourier transform of  $c_{x,y,\sigma}$  in the leg direction,  $Z$  is the grand-canonical partition function,  $|i\rangle$  is an eigenstate with energy  $E_i$ , and  $\Delta_{ji} = E_j - E_i$ . For the asymmetric ladder, the spectral function for the Hubbard leg is considered separately from that of the Fermi leg as indicated by  $y$  in Eq.(2.52). The Hamiltonian (2.1) is particle-hole symmetric, therefore,  $A(k, y, -\omega) = A(k + \pi, y, \omega)$  and the single-particle gap is symmetric around  $\omega = 0$ . Moreover, reflection symmetry in leg direction gives  $A(-k, y, \omega) = A(k, y, \omega)$ .

Fig. 2.23 demonstrates the spectral function for different parameter sets corresponding to the four different phases which have been discussed before. Figs. 2.23(a) and (b) correspond to a parameter set that belongs to the Luttinger liquid phase according to the DMRG results. Indeed, the spectrum on the Fermi leg reveals a free-particle like spectrum with a substantial weight at  $\omega = 0$  and  $k_F = \pi/2$  indicating a metallic phase. The spectrum on the Hubbard leg differs clearly from the spectral function of the Fermi leg and resembles the spectral function of the Hubbard chain [75, 76]. In the second parameter set shown by Figs. 2.23(c) and (d) the lowest excitation wave number is at  $k_g = \pi/2$  in both legs. Similar to Figs. 2.23(a) and (b), the spectral functions are different between Fermi and Hubbard legs. However, the expected gap appears as a pseudogap in both legs due to the finite temperature used in the quantum Monte Carlo simulations. For parameter sets in the spin-gapped Mott phase as in Figs. 2.23(e) and (f), the lowest excitations have incommensurate wave vectors  $k_g$  and  $k'_g$  located symmetrically around  $\pi/2$ . Incommensurate wave vectors for the lowest excitations have been reported before in a half-filled symmetric Hubbard ladder with moderate rung hopping [14], in a frustrated Kondo-Heisenberg model [61], and in various correlated 1D systems such as the bilinear biquadratic spin-1 chain [80] and a two-leg spin ladder with nearest and next-nearest coupling [81, 82]. The CT-INT method has the ability to calculate for weak on-site repulsion  $U$  ( $U = 3$  in the presented case). Thus, such excitations with incommensurate waver vectors are expected down to  $U \rightarrow 0$ . However, field-theoretical methods could be possible for such very weak on-site interaction. The findings of lowest excitations with incommensurate wave vector agree qualitatively with the weak interaction limit in Sec. 2.1.1, Hartree-Fock and DMRG results. Finally, Figs. 2.23(g) and (h) reveal almost identical spectra on the two legs. The lowest hole excitation (particle removal) has the wave vector  $k_g = \pi$  and the lowest particle addition excitation has the wave vector  $k_g = 0$ . These results agree with the analysis of the weak-interaction (Sec. 2.1.1) and the dimer (Sec. 2.1.4) limits. The spectral functions calculated by CT-INT in Fig. 2.23 confirm the existence of four different phases characterized by the wave number of the lowest excitation. One of the four phases is a metallic phase and the others are gapped. The spectrum of the metallic phase supports the idea of an effective decoupling between the Hubbard and Fermi legs.

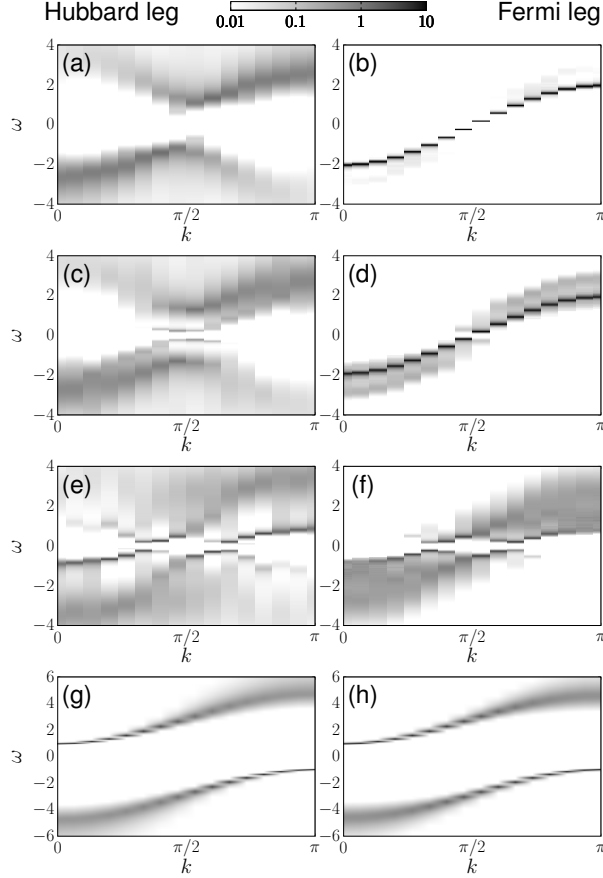


Figure 2.23: Calculations using the CT-INT method of spectral functions  $A(k, y, \omega)$  on the Hubbard leg (left column) and the Fermi leg (right column) with  $\beta t_{\parallel} = 30$ . A periodic ladder with  $L = 30$  rungs and  $U = 5t_{\perp}$  is used. (a) and (b) display Luttinger liquid phase at  $t_{\perp} = 0.1$ . (c) and (d) display Kondo-Mott insulator at  $t_{\perp} = 0.3$ . (e) and (f) display incommensurate spin-gapped Mott insulator at  $t_{\perp} = 1$ . (g) and (h) display correlated band insulator at  $t_{\perp} = 3$ . These calculations and figure are done by M. Hohenadler and published in Ref. [47].

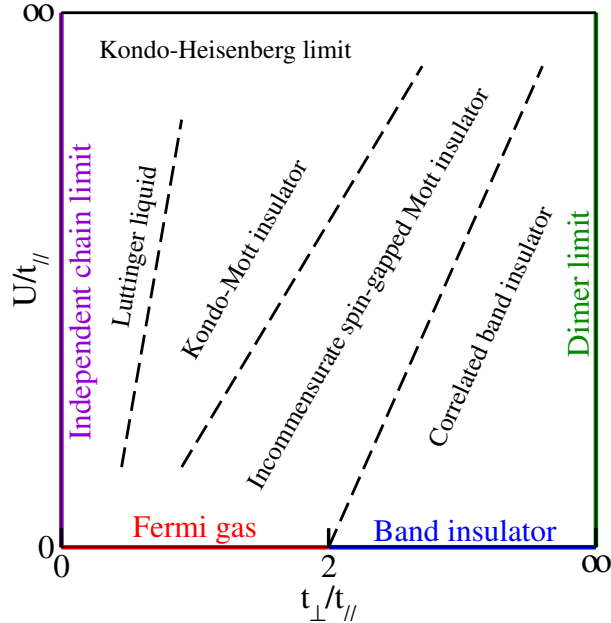


Figure 2.24: Schematic phase diagram of the half-filled asymmetric Hubbard ladder Eq.(2.1). The figure is published in Ref. [47].

## 2.5 Discussion

The asymmetric ladder model (2.1) revealed rich physics at half filling. This model has similarity to the Kondo-Heisenberg model for strong on-site interaction  $U$  or weak rung hopping  $t_{\perp}$ . On the other hand it is similar to the half-filled symmetric Hubbard ladder for weak on-site interaction  $U$  or strong rung hopping  $t_{\perp}$ . It is possible to distinguish three gapped phases by their single-particle excitation spectra but not by a broken symmetry. A Luttinger liquid phase is shown by the DMRG and the CT-INT calculations and is distinguished by different spin and charge velocities. However, the equal single-particle and charge velocities as well as the delocalization of spin and charge components of single-particle excitations on the Fermi leg indicate an effective decoupling between the Hubbard and Fermi legs in this phase. Despite the consistency of the presented analysis, the numerical methods used here are limited by numerical accuracy. Therefore, the existence of exponentially small gap in this phase can not be excluded. To overcome this limitation, field theoretical methods are highly recommended. On the other hand it is interesting that the overall qualitative picture is in consistence with Hartree-Fock phase diagram in Fig. 2.5 except for the presence of Luttinger liquid phase and the absence of long-range antiferromagnetic order. A schematic tentative phase diagram is shown in Fig. 2.24. A major missing information in the present study is the determination of phase boundaries between the three gapped phases. This difficulty is due to the absence of symmetry breaking or gap closing in these phases. However, investigations of entanglement measures could facilitate the search for phase boundaries. It has been used recently to investigate quantum phase transition [83, 84, 85, 86, 87]. The block entropy in the middle of the lattice is calculated for the asymmetric ladder using DMRG method. Nevertheless, no feature that can assist to locate the exact boundaries between the three gapped phases has been found as depicted in Fig. 2.25. Nevertheless, the overall scaling

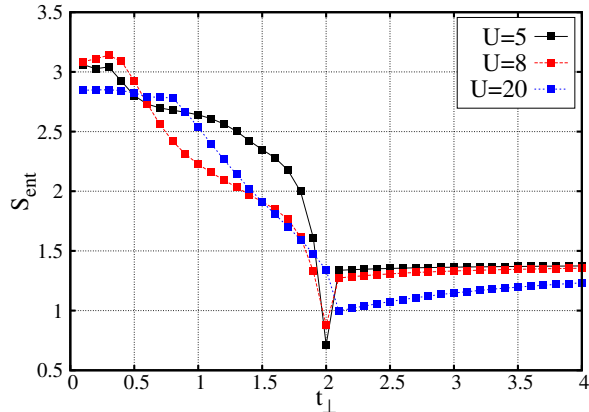


Figure 2.25: Block entanglement entropy  $S_{ent}$  measured at the middle of the ladder system as a function  $t_{\perp}$  for  $U = 5, 8$  and  $20$  and  $L = 128$ .

of the block entropy for different values of on-site interaction  $U$  as a function of  $t_{\perp}$  can reveal different behaviors for the different phases in the asymmetric ladder. One can distinguish a saturation of the block entropy in the correlated band insulating phase as well as a general reduction with respect to  $t_{\perp}$  of the block entropy in the spin-gapped Mott insulating phase. One can not report a specific trend for the other two phases. However, more detailed investigations using extrapolations to  $L_x = \infty$  may assist to distinguish the boundaries of the different phases. Furthermore, a suggestion from the current study is to use more sophisticated entanglement-based analysis, e.g. using the entanglement spectrum [88] and/or the Schmidt gap [89], combined with DMRG calculations to address the issue of phase boundaries. In general, it is important to understand the asymmetric Hubbard ladder by investigating systematically the limiting cases in Sec. 2.1 either by field theoretical methods for weak interacting ladders and weakly coupled chains or by deriving effective models in the strong interaction and dimer limits. Such effective models can be treated better using numerical methods or simple analytic approximations. It is interesting to further investigate the tendency of pairing, competition and coexistence of different long-ranged orders in this model. In this context, more careful calculations should be done for the doped ladder. It is also possible to vary the intra-leg hopping in the Hubbard chain to investigate the relevance to the Kondo-Heisenberg model. Despite the quasi-one-dimensional nature of the asymmetric 2-leg ladder it could facilitate the investigations of 2-dimensional version of the model. This is seen in the unidirectional nature of the PDW order [59] which also justifies investigations of the current asymmetric ladder. Moreover, "proximity effects" between different subsystems in asymmetric ladders, e.g. the Hubbard leg and the Fermi leg in the present study, can clarify similar effects in higher dimension versions [48]. Nevertheless, such comparisons must be taken carefully due to the fundamental differences between correlated electrons in one dimension and their counterparts in higher dimensions.

Viewing this model as a model of wire-substrate system it shows the high sensitivity of the correlated wire to its environment even for small coupling between the wire and the substrate in the gapped phases. In the metallic phase the two legs behave independently. However, some shortcomings affect this approach. It is not enough to represent the substrate by a 1D tight-binding chain because the overall behavior is dominated by the

wire interaction. Furthermore, a single band tight-binding chain can not represent the band insulator substrate in the real wire-substrate reconstructions. Therefore, extensions of the model to represent more degrees of freedoms and more orbitals per site in the substrate are required. This is the subject of the next two chapters.



# Chapter 3

## Ladder mapping and construction of quasi one-dimensional models

This chapter presents a systematic way to construct an effective quasi-1D ladder model for wire-substrate systems. This method starts by constructing a model for a single correlated wire coupled to a 3D noninteracting substrate. The wire-substrate coupling is chosen to be a one particle hopping. Real metallic nanowire reconstructions, as described in Sec.1.2, consist of multi-wire systems. However, if the focus is on Luttinger liquid features and instabilities then a single wire system offers a good approximation. After the construction of the wire-substrate model, we map onto an isotropic 2D ladder system as depicted in Fig. 3.1. This method generalizes the mapping of multi-orbital and multi-site quantum-impurity problems onto ladder systems which has been proposed in Refs. [90, 91]. However, the main difference is that the ladder length, in the present study, is fixed by the wire length while the ladder width is determined by the number of substrate single-particle states. In Refs. [90, 91] the ladder width is determined by the number of impurities and their orbitals while the ladder length is set by the number of single-particle host states. The resulting 2D anisotropic lattice is still not manageable by quasi-one-dimensional methods such as DMRG. Therefore, in this chapter we analyze the possibility of keeping just a few-leg ladder as an approximation of the original wire-substrate system.

Most of the investigations presented here were published in Refs. [49] and [50].

### 3.1 Wire-substrate model

The proposed model Hamiltonian for wire-substrate systems consists of three terms given by

$$H = H_s + H_w + H_{ws} \quad (3.1)$$

where  $H_s$  represents the substrate,  $H_w$  describes the wire, and  $H_{ws}$  corresponds to the interactions between the wire and the substrate. For the moment the focus will be on purely electronic models. Possible generalizations will be discussed later in this chapter. As a convention, there is no distinction between the momentum and the wave number. The reduced Planck constant is considered to be  $\hbar = 1$ .

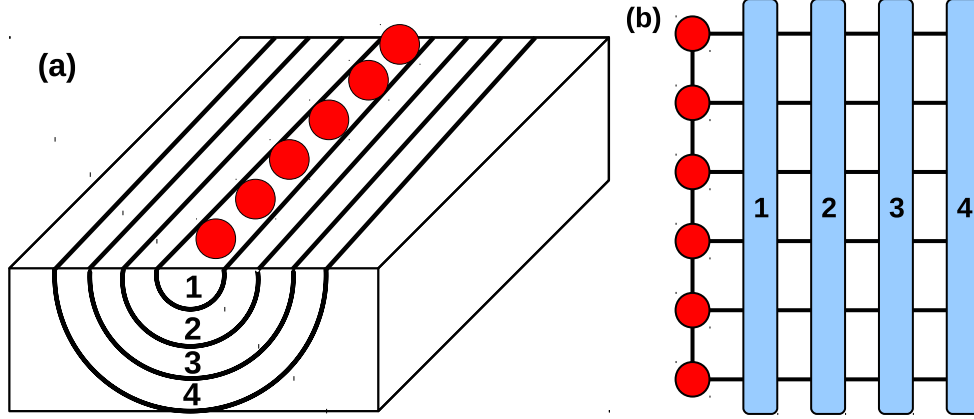


Figure 3.1: (a) Sketch of a wire-substrate model. The atomic wire is represented by red balls. Four numbered shells are displayed in the 3D substrate. (b) Ladder representation of the same system. The left-most leg with red circles corresponds to the atomic wire and the other legs represent the four shells. The figure is published in Ref. [49].

### 3.1.1 The substrate

The structure of the substrate is described by a simple cubic lattice. The unit cell is determined by the lattice constants  $a = b = c = 1$ . The lattice site positions are  $\mathbf{r} = (x, y, z)$  with  $x, y, z \in \mathbb{Z}$ . The coordinate axes are set by the lattice vectors. The substrate size is set by  $L_x, L_y$  and  $L_z$  in  $x, y$  and  $z$  directions, respectively. Periodic boundary conditions are chosen for the  $x$  and  $y$  directions while an open boundary condition is chosen for the  $z$  direction. The substrate surface layer is determined by the  $xy$ -plane which corresponds to  $z = 1$  and, hence, objects on top of the surface correspond to  $z = 0$ .

First, a metallic substrate will be presented, then followed by an extension to an insulating substrate. A metallic substrate is described using a tight-binding Hamiltonian with an on-site potential  $\epsilon_s$  and a nearest-neighbor hopping  $t_s$

$$H_s = \epsilon_s \sum_{\mathbf{r}, \sigma} n_{s\mathbf{r}\sigma} - t_s \sum_{\langle \mathbf{r}\mathbf{q} \rangle} \sum_{\sigma} (c_{s\mathbf{r}\sigma}^\dagger c_{s\mathbf{q}\sigma} + \text{H.c.}) \quad (3.2)$$

The first sum runs over all lattice sites and  $\langle \mathbf{r}\mathbf{q} \rangle$  denotes nearest-neighbor sites  $\mathbf{r}$  and  $\mathbf{q}$ .  $c_{s\mathbf{r}\sigma}^\dagger$  creates an electron with spin  $\sigma$  on the site with coordinates  $\mathbf{r} = (x, y, z)$ .  $n_{s\mathbf{r}\sigma} = c_{s\mathbf{r}\sigma}^\dagger c_{s\mathbf{r}\sigma}$  is the density operator for electrons with spin  $\sigma$ . The diagonalization of this Hamiltonian is carried out by the canonical transformation from the real space to the momentum space representation given by

$$d_{s\mathbf{k}\sigma}^\dagger = \sum_{\mathbf{r}} \psi_{\mathbf{k}}(\mathbf{r}) c_{s\mathbf{r}\sigma}^\dagger \quad (3.3)$$

where the single-particle eigenstates take the form

$$\psi_{\mathbf{k}}(\mathbf{r}) = \frac{1}{\sqrt{L_x}} e^{ik_x x} \frac{1}{\sqrt{L_y}} e^{ik_y y} \sqrt{\frac{2}{L_z + 1}} \sin(k_z z). \quad (3.4)$$

In order to transform back to the real space one uses

$$c_{s\mathbf{r}\sigma}^\dagger = \sum_{\mathbf{k}} \psi_{\mathbf{k}}^*(\mathbf{r}) d_{s\mathbf{k}\sigma}^\dagger \quad (3.5)$$

where the sum runs over all sites  $\mathbf{k} = (k_x, k_y, k_z)$  of the reciprocal lattice, i.e.

$$k_x = \frac{2\pi}{L_x}n_x, \quad n_x \in \mathbb{Z}, \quad -\frac{L_x}{2} < n_x \leq \frac{L_x}{2} \quad (3.6a)$$

$$k_y = \frac{2\pi}{L_y}n_y, \quad n_y \in \mathbb{Z}, \quad -\frac{L_y}{2} < n_y \leq \frac{L_y}{2} \quad (3.6b)$$

$$k_z = \frac{\pi}{L_z + 1}n_z, \quad n_z \in \mathbb{Z}, \quad 1 \leq n_z \leq L_z. \quad (3.6c)$$

The differences between the  $z$ -component and the other two components in Eq.(3.4) and Eq.(3.6) is due to the different boundary conditions. Therefore, Hamiltonian (3.2) becomes diagonal in the momentum-space representation

$$H_s = \sum_{\mathbf{k}, \sigma} \epsilon_s(\mathbf{k}) d_{s\mathbf{k}\sigma}^\dagger d_{s\mathbf{k}\sigma} \quad (3.7)$$

with the single-electron dispersion

$$\epsilon_s(\mathbf{k}) = \epsilon_s - 2t_s[\cos(k_x) + \cos(k_y) + \cos(k_z)]. \quad (3.8)$$

As it was mentioned before, realistic substrates are semiconductors [54, 92, 93]. Thus, it is appropriate to define two separate valence and conduction bands for the substrate. This is achieved using the above mentioned lattice but with two orbitals per site. Each orbital is subjected to two different potentials,  $\epsilon_v$  for the valence bands and  $\epsilon_c$  for the conduction band. Hence, the Hamiltonian takes the form

$$H_s = H_v + H_c. \quad (3.9)$$

The valence-band Hamiltonian is

$$H_v = \epsilon_v \sum_{\mathbf{r}, \sigma} n_{v\mathbf{r}\sigma} - t_v \sum_{\langle \mathbf{r}\mathbf{q} \rangle} \sum_{\sigma} (c_{v\mathbf{r}\sigma}^\dagger c_{v\mathbf{q}\sigma} + \text{H.c.}) \quad (3.10)$$

and the conduction-band Hamiltonian is

$$H_c = \epsilon_c \sum_{\mathbf{r}, \sigma} n_{c\mathbf{r}\sigma} - t_c \sum_{\langle \mathbf{r}\mathbf{q} \rangle} \sum_{\sigma} (c_{c\mathbf{r}\sigma}^\dagger c_{c\mathbf{q}\sigma} + \text{H.c.}). \quad (3.11)$$

$c_{v\mathbf{r}\sigma}^\dagger$  and  $c_{c\mathbf{r}\sigma}^\dagger$  create electrons with spin  $\sigma$  on site  $\mathbf{r}$  in the localized orbitals corresponding to the valence and conduction bands, respectively.  $n_{v\mathbf{r}\sigma}$  and  $n_{c\mathbf{r}\sigma}$  denote the corresponding density operators. Both, valence and conduction band Hamiltonians represent tight-binding Hamiltonians with corresponding nearest-neighbor hopping terms  $t_v$  and  $t_c$ . Similar canonical transformations as Eq.(3.3), i.e. from the real space to the momentum space, are carried out to obtain the diagonal Hamiltonians

$$H_v = \sum_{\mathbf{k}, \sigma} \epsilon_v(\mathbf{k}) d_{v\mathbf{k}\sigma}^\dagger d_{v\mathbf{k}\sigma} \quad (3.12)$$

and

$$H_c = \sum_{\mathbf{k}, \sigma} \epsilon_c(\mathbf{k}) d_{c\mathbf{k}\sigma}^\dagger d_{c\mathbf{k}\sigma}. \quad (3.13)$$

The single-electron dispersions  $\epsilon_v(\mathbf{k})$  for the valence band and  $\epsilon_c(\mathbf{k})$  for the conduction band are similar to Eq.(3.8). A finite gap  $\Delta_s$  opens between the bottom of the conduction band and the top of the valence band. This is fulfilled by choosing a positive non-zero value for  $\Delta_s$  in the relation  $\Delta_s = \epsilon_c - \epsilon_v - 6(|t_v| + |t_c|)$ .

### 3.1.2 The wire

A simple representation of the wire is achieved using a 1D chain with a length  $L_x$  in the  $x$ -direction. The wire sites have positions  $\mathbf{r} = (x, y_0, 0)$  with  $y_0 \in \{1, \dots, L_y\}$ . This means that every site of the wire is exactly on top of the corresponding substrate site. Thus, the lattice constant of the wire is equal to that of the substrate. Similar to chapter 2, the wire is described by the 1D Hubbard model [11] given by

$$H_w = \epsilon_w \sum_{x,\sigma} n_{wx\sigma} - t_w \sum_{x,\sigma} \left( c_{wx\sigma}^\dagger c_{w,x+1,\sigma} + \text{H.c.} \right) + U \sum_x n_{wx\uparrow} n_{wx\downarrow}. \quad (3.14)$$

The sums over  $x$  run over all wire sites. The operator  $c_{wx\sigma}^\dagger$  creates an electron with spin  $\sigma$  on the wire site  $\mathbf{r} = (x, y_0, 0)$ . The density operator for electrons with spin  $\sigma$  is denoted by  $n_{wx\sigma} = c_{wx\sigma}^\dagger c_{wx\sigma}$ .  $t_w$  is the usual hopping term between nearest-neighbor sites in the wire.  $\epsilon_w$  is a wire on-site potential. The representation of the 1D Hubbard model in momentum space is done by the canonical transformation

$$d_{wk\sigma}^\dagger = \frac{1}{\sqrt{L_x}} \sum_x e^{ikx} c_{wx\sigma}^\dagger \quad (3.15)$$

where the inverse transformation is given by

$$c_{wx\sigma}^\dagger = \frac{1}{\sqrt{L_x}} \sum_k e^{-ikx} d_{wk\sigma}^\dagger. \quad (3.16)$$

Thus, the wire Hamiltonian takes the form

$$H_w = \sum_{k,\sigma} \epsilon_w(k) d_{wk\sigma}^\dagger d_{wk\sigma} + \frac{U}{L_x} \sum_{k,p,k',p'} d_{wk\uparrow}^\dagger d_{wp\uparrow} d_{wk'\downarrow}^\dagger d_{wp'\downarrow} \delta_{k-p,p'-k'} \quad (3.17)$$

with the single-electron dispersion

$$\epsilon_w(k) = \epsilon_w - 2t_w \cos(k). \quad (3.18)$$

Here  $k, p, k'$ , and  $p'$  denote momenta in the  $x$ -direction, see Eq.(3.6a). It is important to remember that the transformation to the momentum space is done in the  $x$ -direction of the wire. This means that the other two dimensions are irrelevant for the wire and they can remain in the real-space representation for the substrate. This allows a mixed real-space/momentum-space representation for the full wire-substrate Hamiltonian.

### 3.1.3 The wire-substrate hybridization

Again, similar to the asymmetric 2-leg Hubbard ladder, the wire substrate coupling is modeled by a nearest-neighbor single-particle hopping between the wire sites and the adjacent substrate sites. This coupling hybridizes the wire and substrate electronic orbitals.

This results in a hybridization with the metallic substrate given by

$$H_{ws} = -t_{ws} \sum_{x,\sigma} (c_{sr\sigma}^\dagger c_{wx\sigma} + \text{H.c.}) \quad (3.19)$$

with  $\mathbf{r} = (x, y_0, 1)$ . The hybridization part becomes

$$H_{ws} = \sum_{\mathbf{k}\sigma} \left[ \Gamma_{ws}(\mathbf{k}) d_{s\mathbf{k}\sigma}^\dagger d_{wk_x\sigma} + \text{H.c.} \right] \quad (3.20)$$

in the momentum-space representation with the hybridization function

$$\Gamma_{ws}(\mathbf{k}) = -t_{ws} \sqrt{\frac{2}{L_y(L_z + 1)}} \exp(-ik_y y_0) \sin(k_z) \quad (3.21)$$

which is independent of the  $x$ -component of the wave vector.

In the insulating substrate, the hybridization between the wire and the valence band could be different from the hybridization with the conduction band. Nevertheless, the total hybridization is given by

$$H_{ws} = H_{wv} + H_{wc} \quad (3.22)$$

where

$$H_{wv} = -t_{wv} \sum_{x,\sigma} (c_{vr\sigma}^\dagger c_{wx\sigma} + \text{H.c.}) \quad (3.23)$$

represents the hybridization between the wire and the valence band while

$$H_{wc} = -t_{wc} \sum_{x,\sigma} (c_{cr\sigma}^\dagger c_{wx\sigma} + \text{H.c.}) \quad (3.24)$$

represents the hybridization between the wire and the conduction band. Similar to Eq.(3.20), the momentum-space representations for  $H_{wv}$  and  $H_{wc}$  are given by

$$H_{wv} = \sum_{\mathbf{k}\sigma} \left[ \Gamma_{wv}(\mathbf{k}) d_{v\mathbf{k}\sigma}^\dagger d_{wk_x\sigma} + \text{H.c.} \right] \quad (3.25)$$

and

$$H_{wc} = \sum_{\mathbf{k}\sigma} \left[ \Gamma_{wc}(\mathbf{k}) d_{c\mathbf{k}\sigma}^\dagger d_{wk_x\sigma} + \text{H.c.} \right] \quad (3.26)$$

with hybridization functions  $\Gamma_{wv}(\mathbf{k})$  and  $\Gamma_{wc}(\mathbf{k})$  similar to Eq.(3.21) but with  $t_{wv}$  and  $t_{wc}$  for valence and conduction bands, respectively, instead of  $t_{ws}$ .

### 3.1.4 Generalizations

There are several ways to generalize this wire-substrate model. One way is to use the ability of changing the substrate structure and the wire-substrate hybridization in the momentum space. This can be achieved by changing the substrate band structure to be different from the cosine bands described in Eq. (3.8). The wire-substrate hybridization could be defined using different hybridization function of the wave vector  $\mathbf{k}$ . Furthermore,

the wire could be described by different dispersion than the cosine one or by adding long-range interaction in the wire direction.

It is also possible to increase the number of bands or to use a different lattice structure in the substrate as long as there is no interaction in it. This leads to the possibility of using first-principle simulation results to construct the substrate and to obtain the wire-substrate hybridization [94]. Such a possibility allows, in principle, comparisons with experimental results.

An other possible way is to generalize the wire-substrate model by adding phonon degrees of freedom to the substrate but without electron-phonon coupling. The phonon degrees of freedom can be added to the wire with electron-phonon coupling. A hybridization between the wire and substrate degrees of freedom can be added as well.

## 3.2 Ladder representation

This section is devoted to explaining the mapping of the aforementioned wire-substrate model onto a 2D anisotropic lattice. The method consists of three steps. Firstly, the Hamiltonian is written in the momentum-space or in a mixed representation by choosing the momentum space in the wire direction and the real space in the other two directions. This gives the ability to slice the Hamiltonian in the wire direction onto independent impurity problems with 2D hosts. Secondly, each impurity problem is mapped onto a 1D chain using the Lanczos algorithm. Finally, the recovery to real space in the  $x$ -direction is performed using the inverse momentum space to real space transformation.

### 3.2.1 Impurity subsystems

Firstly, the Hamiltonian (3.1) is written assuming a noninteracting wire ( $U = 0$ ) to simplify the discussion. However, the process is applicable to the interacting wire as long as there is no interaction in the substrate as shown later. The Hamiltonian takes the form of a set of independent sub-Hamiltonians  $H_{k_x\sigma}$  in the momentum space. Therefore, this set fulfills the condition  $[H_{k_x\sigma}, H_{k'_x\sigma'}] = 0 \forall k_x, k'_x, \sigma, \sigma'$ . Thus, the full Hamiltonian is given by the summation

$$H = \sum_{k_x, \sigma} H_{k_x\sigma} \quad (3.27)$$

with

$$\begin{aligned} H_{k_x\sigma} = & \epsilon_w(k_x) d_{wk_x\sigma}^\dagger d_{wk_x\sigma} + \sum_{k_y, k_z, \sigma} \epsilon_s(\mathbf{k}) d_{sk\sigma}^\dagger d_{sk\sigma} \\ & + \sum_{k_y, k_z, \sigma} \left[ \Gamma_{ws}(\mathbf{k}) d_{sk\sigma}^\dagger d_{wk_x\sigma} + \text{H.c.} \right] \end{aligned} \quad (3.28)$$

for a metallic substrate, or

$$\begin{aligned}
H_{k_x\sigma} &= \epsilon_w(k_x) d_{wk_x\sigma}^\dagger d_{wk_x\sigma} \\
&+ \sum_{k_y, k_z, \sigma} \epsilon_c(\mathbf{k}) d_{ck\sigma}^\dagger d_{ck\sigma} + \sum_{k_y, k_z, \sigma} \epsilon_v(\mathbf{k}) d_{vk\sigma}^\dagger d_{vk\sigma} \\
&+ \sum_{k_y, k_z, \sigma} \left[ \Gamma_{wc}(\mathbf{k}) d_{ck\sigma}^\dagger d_{wk_x\sigma} + \text{H.c.} \right] \\
&+ \sum_{k_y, k_z, \sigma} \left[ \Gamma_{wv}(\mathbf{k}) d_{vk\sigma}^\dagger d_{wk_x\sigma} + \text{H.c.} \right]
\end{aligned} \tag{3.29}$$

for an insulating substrate with  $\mathbf{k} = (k_x, k_y, k_z)$ . Each Hamiltonian  $H_{k_x\sigma}$  has the dimension  $N_{\text{imp}} = L_y L_z + 1$  (for the metallic substrate) or  $N_{\text{imp}} = 2L_y L_z + 1$  (for the insulating substrate). For a noninteracting wire ( $U = 0$ ), each  $H_{k_x\sigma}$  is a single-particle problem and it is amenable to exact diagonalization.  $H_{k_x\sigma}$  represents a non-magnetic impurity with the energy level  $\epsilon_w(k_x)$  corresponding to the wire. This energy level is coupled by the hybridization functions  $\Gamma_b(\mathbf{k})$  to a 2D host determined by a substrate  $(k_y, k_z)$ -slice. Each  $(k_y, k_z)$ -slice corresponds only to the given wave vector  $k_x$  of the wire. The metallic host eigenenergies range from the minimum to the maximum of  $\epsilon_s(\mathbf{k})$  for the given  $k_x$  while for the insulating host they range between the minimum and the maximum of  $\epsilon_{c,v}(\mathbf{k})$  for the given  $k_x$ .

The impurity Hamiltonian with the 2D host,  $H_{k_x\sigma}$ , can be written as a Hamiltonian for an impurity coupled to a real space represented  $(yz)$ -slice for a given  $k_x$  momentum. This can be done by starting from a mixed real/momentum-space representation,  $(k_x, y, z)$  of the Hamiltonian. Fig. 3.2 shows a schematic representation of a  $k_x$ -impurity coupled to  $(yz)$ -slice. By taking the limit  $N_{\text{imp}} \rightarrow \infty$  in the impurity problem, the single-particle eigenenergies of each  $H_{k_x\sigma}$  constitute one continuum for the metallic substrate or two continua for the insulating substrate. It is known [95] that either an eigenenergy lies in a continuum and the corresponding eigenstate is delocalized in the impurity-host subsystem or the eigenenergy lies outside any continuum and the eigenstate is localized around the impurity. This means that single-electron eigenstates are delocalized in the full wire-substrate system if they have eigenenergies within the substrate bands, or are restricted to the wire or to the area around it if the eigenenergies are outside the substrate bands.

### 3.2.2 Chain representation

It is known, since the introduction of Wilson's renormalization group method [96, 97], that the impurity in a 2D host problem can be mapped onto a 1D chain with nearest-neighbor hopping and diagonal terms using the Lanczos algorithm. This method produces iteratively a tri-diagonal matrix from any general hermitian matrix. The procedure is described using the generation of the orthogonal single-particle states  $|k_x, n, \sigma\rangle$  for  $n = 1, \dots, N_{\text{imp}} - 1$  with

$$\begin{aligned}
|k_x, n + 1, \sigma\rangle &= H_{k_x\sigma} |k_x, n, \sigma\rangle - A_n(k_x, \sigma) |k_x, n, \sigma\rangle \\
&- B_n^2(k_x, \sigma) |k_x, n - 1, \sigma\rangle.
\end{aligned} \tag{3.30}$$

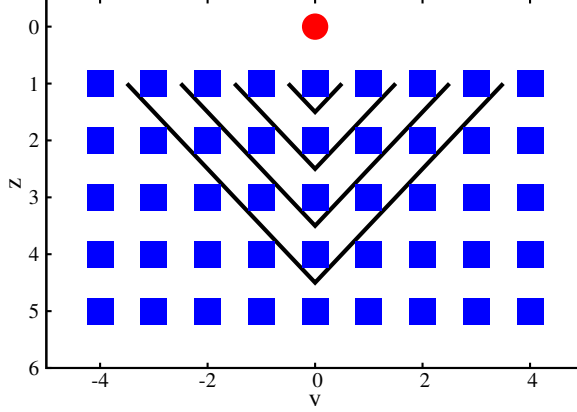


Figure 3.2: Sketch of the impurity-host subsystem in the mixed representation with  $L_y = 9$  and  $L_z = 5$ . The red circle at  $(y_0 = 0, z = 0)$  represents the wire site (impurity) while the blue squares represents the substrate sites (host). Black lines display the boundary of the first, second, third and fourth shells (from top to bottom) around the impurity. The figure is published in Ref. [49].

where  $A_n(k_x, \sigma)$  is given by

$$A_n(k_x, \sigma) = \frac{\langle k_x, n, \sigma | H | k_x, n, \sigma \rangle}{\langle k_x, n, \sigma | k_x, n, \sigma \rangle} \quad (3.31)$$

and  $B_n^2(k_x, \sigma)$  is given by

$$B_n^2(k_x, \sigma) = \frac{\langle k_x, n, \sigma | k_x, n, \sigma \rangle}{\langle k_x, n-1, \sigma | k_x, n-1, \sigma \rangle} \quad (3.32)$$

for  $n = 1, \dots, N_{\text{imp}} - 1$  and  $B_{0,\sigma}(k_x) = 0$ .  $H_{k_x\sigma}$  is the Hamiltonian of the impurity subsystem (3.28) for the metallic substrate or (3.29) for the insulating substrate. The initial single-electron states are  $|k_x, -1, \sigma\rangle = 0$  and  $|k_x, 0, \sigma\rangle = d_{wk_x\sigma}^\dagger |\emptyset\rangle$ , where  $|\emptyset\rangle$  denoted the vacuum state. The selection of the suitable initial state must be in a way that does not change the state which represents the wire. Therefore, the state  $d_{wk_x\sigma}^\dagger |\emptyset\rangle$  is chosen to start the procedure. However, in other contexts, the Lanczos algorithm can be used as a method for matrix diagonalization in which the initial state can be selected arbitrarily.

After the Lanczos transformation,  $H_{k_x\sigma}$  has a chain representation given by

$$\begin{aligned} H_{k_x\sigma} &= \sum_{n=0}^{N_{\text{imp}}-1} A_n(k_x, \sigma) f_{k_x n \sigma}^\dagger f_{k_x n \sigma} \\ &+ \sum_{n=0}^{N_{\text{imp}}-2} \left[ B_{n+1}(k_x, \sigma) f_{k_x n \sigma}^\dagger f_{k_x, n+1, \sigma} + \text{H.c.} \right] \end{aligned} \quad (3.33)$$

where the new fermion operators  $f_{k_x n \sigma}^\dagger$  create electrons in the states  $|k_x, n, \sigma\rangle$ . It is clear that this transformation does not change the wire states i.e.,  $f_{k_x, n=0, \sigma}^\dagger = d_{wk_x\sigma}^\dagger$ . Furthermore, due to the spin rotation symmetry of the wire-substrate model, this transformation and the coefficients  $A_n$  and  $B_n$  are independent of the spin  $\sigma$ . Moreover, the choice of



the initial state gives the first diagonal term  $A_0(k_x, \sigma) = \epsilon_w(k_x)$  which corresponds to the impurity on-site potential and the first nearest-neighbor hopping terms which correspond to the coupling between the impurity and the host, i.e.

$$B_1^2(k_x, \sigma) = \sum_{k_y, k_z} |\Gamma_{ws}(\mathbf{k})|^2 \quad (3.34)$$

for the metallic substrate and

$$B_1^2(k_x, \sigma) = \sum_{k_y, k_z} [|\Gamma_{wc}(\mathbf{k})|^2 + |\Gamma_{wv}(\mathbf{k})|^2] \quad (3.35)$$

for the insulating substrate.

The cosine dispersion Eq.(3.8) and the hybridization Eq.(3.21) make the mixed representation relatively simple for demonstration. In this case, the host sites are coupled by the nearest-neighbor hopping terms  $t_s$ . The impurity on-site potential  $\epsilon_w(k_x)$  sets on the first diagonal element and remains unchanged in the chain representation as it is stated before. For all host sites, the on-site potential is  $\epsilon_s - t_s \cos(k_x)$  which constitutes the rest of the diagonal elements in the chain representation, i.e.  $A_n(k_x, \sigma) = \epsilon_s - 2t_s \cos(k_x)$  for  $n \geq 1$ . The hopping term between the impurity and the adjacent host site is  $t_{ws}$  which determines the coupling between the impurity and its nearest-neighbor site in the chain representation (the first off-diagonal term), i.e.  $B_1^2(k_x, \sigma) = t_{ws}^2$ . Thus, by performing the Lanczos transformation, the state  $|k_x, n, \sigma\rangle$  is entirely localized in the nearest  $m$  neighbor host shell to the impurity. These shells are shown in Fig. 3.2. Then, the next few off-diagonal terms are given analytically by

$$B_2^2(k_x, \sigma) = 3t_s^2, \quad (3.36a)$$

$$B_3^2(k_x, \sigma) = \frac{11}{3}t_s^2, \quad (3.36b)$$

$$B_4^2(k_x, \sigma) = \frac{125}{33}t_s^2. \quad (3.36c)$$

Similar process is applied to the insulating substrate by assuming cosine dispersions for the valence and conduction bands to obtain

$$A_1(k_x, \sigma) = \frac{t_{wc}^2 [\epsilon_c - 2t_c \cos(k_x)] + t_{wv}^2 [\epsilon_v - 2t_v \cos(k_x)]}{t_{wc}^2 + t_{wv}^2},$$

$$B_1^2(k_x, \sigma) = \Gamma^2(k_x) = t_{wc}^2 + t_{wv}^2.$$

If the valence and conduction bands are similar, i.e.,  $t_v = t_c = t_s$  and  $t_{wc}^2 = t_{wv}^2 = t_{ws}^2$ , then  $A_n(k_x, \sigma) = \frac{\epsilon_c + \epsilon_v}{2} - 2t_s \cos(k_x)$  for  $n \geq 1$  and

$$B_1^2(k_x, \sigma) = 2t_{ws}^2, \quad (3.37a)$$

$$B_2^2(k_x, \sigma) = \sqrt{3t_s^2 + \left(\frac{\epsilon_c - \epsilon_v}{2}\right)^2}. \quad (3.37b)$$

The full Hamiltonian (3.1) can now be written using Eq.(3.27) by using the chain representations of  $H_{k_x\sigma}$ .

### 3.2.3 Real-space representation

The final step is the back transformation to real space in the wire direction. The performed Lanczos algorithm does not change the initial state in the impurity sub-systems. This guarantee that the wire Hamiltonian  $H_w$  remains unchanged after the inverse transformation to real space in the  $x$ -direction. A new fermion operator is defined to perform the inverse transformation for the substrate

$$g_{xn\sigma}^\dagger = \frac{1}{\sqrt{L_x}} \sum_{k_x} e^{-ik_x x} f_{k_x n \sigma}^\dagger. \quad (3.38)$$

This new operator creates an electron with spin  $\sigma$  at position  $x$  in the  $n$ -th shell. Thus the substrate Hamiltonian can be written as

$$\begin{aligned} H_s = & \sum_{n=1}^{N_{\text{imp}}-1} \sum_{x,x',\sigma} A_n(x-x') g_{xn\sigma}^\dagger g_{x'n\sigma} \\ & + \sum_{n=1}^{N_{\text{imp}}-2} \sum_{x,x',\sigma} \left[ B_{n+1}(x-x') g_{xn\sigma}^\dagger g_{x',n+1,\sigma} + \text{H.c.} \right]. \end{aligned} \quad (3.39)$$

The amplitude

$$A_n(x) = \frac{1}{L_x} \sum_{k_x} A_n(k_x, \sigma) \exp(ik_x x) \quad (3.40)$$

is the long range inter-shell hopping term in the wire direction for  $x \neq 0$ , but, for  $x = 0$  it denotes the on-site potential in the  $n$ -th shell. Similarly

$$B_{n+1}(x) = \frac{1}{L_x} \sum_{k_x} B_{n+1}(k_x, \sigma) \exp(ik_x x) \quad (3.41)$$

is the inter-shell long range hopping amplitude between the  $n$  and  $n+1$  shells. The wire-substrate hybridization becomes

$$H_{\text{ws}} = \sum_{x,x',\sigma} \left[ \Gamma(x-x') g_{x,n=1,\sigma}^\dagger c_{wx'\sigma} + \text{H.c.} \right] \quad (3.42)$$

where

$$\Gamma(x) = \frac{1}{L_x} \sum_{k_x} B_1(k_x, \sigma) \exp(ik_x x) \quad (3.43)$$

represents the long range hopping amplitudes between wire sites and sites in the first shell in the substrate. Therefore, the original wire-substrate Hamiltonian (3.1) is transformed onto a 2D lattice of size  $L_x \times N_{\text{imp}}$  with long-range hopping terms. This new representation can be simplified by assuming that the hybridization is independent from the  $x$ -component of the wave vector  $\mathbf{k}$ , i.e.

$$\Gamma_b(\mathbf{k}) = \Gamma_b(k_y, k_z) \quad (\text{b=ws,wc,wv}) \quad (3.44)$$

and that the dispersion takes the additive form

$$\epsilon_b(\mathbf{k}) = \nu(k_x) + \epsilon_b(k_y, k_z) \quad (\text{b=s, c, v}). \quad (3.45)$$

The tight-binding Hamiltonians defined in Sec. 3.1 fulfills these conditions but the insulating substrate must have  $t_c = t_v = t_s$ . The impurity on-site potential  $\epsilon_w(k_x)$  and the constant shift in the substrate dispersion  $\nu(k_x)$  are the only parts which depend on  $k_x$  in the impurity Hamiltonians  $H_{k_x\sigma}$ . Therefore, all  $k_x$  chain representations are identical up to an energy shift. Thus, the hybridization and the inter-shell hopping are restricted nearest neighbors and take the form

$$\Gamma(x) = \Gamma\delta_{x,0} \quad (3.46)$$

with  $\Gamma = B_1(k_x, \sigma)$  and

$$B_n(x) = -t_n^{\text{rung}}\delta_{x,0} \quad n \geq 2 \quad (3.47)$$

with  $t_n^{\text{rung}} = -B_n(k_x, \sigma)$ . Moreover, one can realize that

$$A_n(x) = -t_x^{\text{leg}} + \mu_n\delta_{x,0} \quad n \geq 1 \quad (3.48)$$

with

$$t_x^{\text{leg}} = -\frac{1}{L_x} \sum_{k_x} \nu(k_x) \exp(ik_x x) \quad (3.49)$$

and  $\mu_n = A_n(k_x, \sigma) - \nu(k_x)$ . Thus, the wire-substrate Hamiltonian (3.1) becomes a 2D ladder system with  $L_x$  rungs and  $N_{\text{imp}}$  legs, as shown in Fig. 3.1. The leg  $n = 0$  represents the the wire with  $g_{x,n=0,\sigma}^\dagger = c_{wx\sigma}^\dagger$ , while legs  $n = 1, \dots, N_{\text{imp}} - 1$  correspond to the successive shells that represent the substrate. One has again to remember that the transformation of the substrate dose not affect the wire sites. Therefore, general electron-electron interactions can be included in the wire Hamiltonian without affecting the validity of the mapping as long as the translation invariance in  $x$ -direction is preserved. Beside the translation invariance in the  $x$ -direction, Eqs.(3.44) and (3.45) are the main conditions for the mapping. The new representation of the Hamiltonian has a hopping term  $\Gamma$  (hybridization) between sites in the wire and sites with the same  $x$ -value in the first leg in addition to nearest-neighbor rung hopping terms  $t_n^{\text{rung}}$  between the substrate legs  $n-1$  and  $n$ . However, an on-site potential  $\mu_n - t_0^{\text{leg}}$  and a long-range intra-leg hopping terms  $t_x^{\text{leg}}$  in every substrate leg are also present. The restriction to the dispersion in the form of Eq.(3.8), i.e.  $\nu(k_x) = -2t_s \cos(k_x)$ , simplifies the ladder system and gives the hopping terms within the substrate legs as

$$t_x^{\text{leg}} = \begin{cases} t_s & \text{if } |x| = 1 \\ 0 & \text{otherwise.} \end{cases} \quad (3.50)$$

The resulting explicit form of the full Hamiltonian is

$$\begin{aligned} H &= H_w + \sum_{x,\sigma} \left( \Gamma g_{x,n=1,\sigma}^\dagger c_{wx\sigma} + \text{H.c.} \right) \\ &+ \sum_{n=1}^{N_{\text{imp}}-1} \sum_{x,\sigma} \mu_n g_{xn\sigma}^\dagger g_{xn\sigma} \\ &- t_s \sum_{n=1}^{N_{\text{imp}}-1} \sum_{x,\sigma} \left( g_{xn\sigma}^\dagger g_{x+1,n\sigma} + \text{H.c.} \right) \\ &- \sum_{n=1}^{N_{\text{imp}}-2} \sum_{x,\sigma} \left( t_{n+1}^{\text{rung}} g_{xn\sigma}^\dagger g_{x,n+1,\sigma} + \text{H.c.} \right). \end{aligned} \quad (3.51)$$

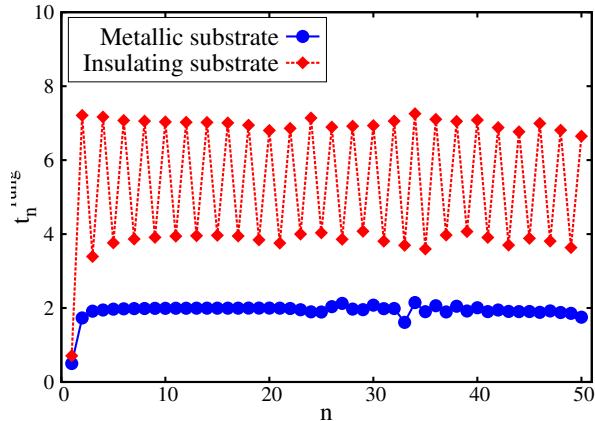


Figure 3.3: Hopping terms  $t_x^{\text{rung}}$  calculated numerically with the Lanczos algorithm between legs  $n - 1$  and  $n$ . The circles display results for a metallic substrate with  $t_s = 1$ ,  $t_{\text{ws}}^2 = 0.25$ ,  $L_y = 32$ , and  $L_z = 16$ . The diamonds display results for an insulating substrate with  $t_c = t_v = 1$ ,  $t_{\text{wc}}^2 = t_{\text{wv}}^2 = 0.25$ ,  $\epsilon_c = -\epsilon_v = 7$ ,  $L_y = 32$ , and  $L_z = 8$ . The figure is published in Ref. [49].

For the metallic substrate,  $\mu_n = \epsilon_s$  while  $\Gamma = -t_{\text{ws}}$  and the first few hopping terms  $t_n^{\text{rung}} = -B_n(k_x, \sigma)$  are given in Eq.(3.36). For the insulating substrate with  $t_c = t_v = t_s$  and  $t_{\text{wc}}^2 = t_{\text{wv}}^2 = t_{\text{ws}}^2$ , one gets  $\mu_n = \frac{\epsilon_c + \epsilon_v}{2}$  while  $\Gamma = -B_1(k_x, \sigma)$  and  $t_2^{\text{rung}} = -B_2(k_x, \sigma)$  are given in Eq.(3.37). The hopping terms  $t_n^{\text{rung}}$  for larger indices  $n$  can be computed numerically with the Lanczos algorithm as described in Sec. 3.2.2. Figure 3.3 shows the hopping terms calculated for a metallic and an insulating substrate. We see that they converge to  $\sim 2t_s$  for large  $n$  in the metallic case while they oscillate around  $\sim 5.5t_s$  for the insulating case. The alternation of the hopping terms is necessary to generate the gap between valence and conduction bands in the insulating substrate.

### 3.2.4 Alternate representation for the insulating substrate

Condition (3.45) is inconvenient for the insulating substrate because it imposes the same dispersion  $\nu(k_x)$  in the valence and conduction bands to obtain a ladder-like Hamiltonian. However, it is possible to overcome this difficulty with an alternate mapping. As the electronic states of the conduction and valence bands interact only through the impurity site, one can use a two-chain representation of the impurity problem with one chain representing the valence-band sites and the other chain representing the conduction-band sites. Both chains can be generated separately using the Lanczos algorithm as described in Sec. 3.2.2. This allows condition (3.45) to be satisfied separately for the conduction and valence bands, i.e. with two different forms of dispersions for  $\nu_c(k_x)$  and  $\nu_v(k_x)$ . Then, the wire chain is situated in the middle of the ladder between the legs representing the valence band and the other legs representing the conduction band. The Hamiltonian parameters  $A_n(k_x, \sigma)$ , and  $B_n(k_x, \sigma)$  are given by equations similar to those obtained for the metallic substrate, e.g., by Eq.(3.36), but with  $\{\epsilon_s, t_s\}$  replaced by  $\{\epsilon_v, t_v\}$  for the valence band legs and  $\{\epsilon_c, t_c\}$  for the conduction band legs.

Despite the necessity of the translation invariance symmetry to perform the aforementioned mapping, this symmetry can be relaxed by performing the mapping only on

the substrate and then connecting it to the wire. This allows the wire to include disorder, a nonuniform wire-substrate hybridization, an electron-electron interaction between the wire and the adjacent substrate sites or a modulated periodic potential. The initial step is to consider a decoupled wire from the substrate. Then the procedure can be described using a mixed representation  $(k_x, y, z)$  of the metallic substrate with the dispersion (3.8). The Lanczos iterations can be performed starting from site  $(k_x, y_0, z = 1)$ . The resulting chain representation of a metallic substrate gives  $A_n(k_x) = \epsilon_s - 2t_s \cos(k_x)$  for  $n \geq 0$  and

$$B_1^2(k_x) = 3t_s^2, \quad (3.52a)$$

$$B_2^2(k_x) = \frac{11}{3}t_s^2, \quad (3.52b)$$

$$B_3^2(k_x) = \frac{125}{33}t_s^2. \quad (3.52c)$$

Hence, by transforming back to the real-space representation along the  $x$ -direction a ladder representation for the substrate is obtained. Therefore, a general form of  $x$ -dependent hopping terms as well as electron-electron interaction terms between wire sites and their adjacent substrate sites can be introduced. This process can be applied for an insulating substrate by considering the conduction and valence bands separately as it is described above as an alternate representation.

### 3.3 Effective narrow ladder model (NLM)

So far, the mapping of the wire-substrate model onto a 2D anisotropic ladder system is exact. However, the problem remains highly complex at least if it is approached with methods for quasi-1D systems such as DMRG. Nevertheless, the reduction of the full 2D ladder system onto a quasi-1D system is a possible way to approximate the model. It is expected to be a good approximation because of two reasons. First, the 1D physics is expected to take place in the wire or close to it. This area corresponds to the wire and its few nearest neighbor legs. Second, the recently developed density matrix embedding theory shows that the environment of a quantum subsystem is not required to be larger than the subsystem itself [98]. Therefore, in principle, the minimal representation of the substrate is not required to be larger than the wire itself. However, the construction of such minimal environment needs the solution of the full wire-substrate problem. This means that one has to think about an other good approximation for the environment such as the proposed truncation of the mapped 2D ladder Hamiltonian (3.51) onto a few-leg ladder. From here on, the truncated few-leg ladder approximation of Hamiltonian (3.51) will be called the narrow ladder model (NLM). The number of legs in this NLM is denoted  $N_{\text{leg}}$ .

First, the noninteracting wire-substrate cases are analyzed followed by the interacting Hubbard-type wire cases. The spectral properties for noninteracting cases are investigated. This is achieved by calculating the single-particle spectral function (SPSF) and the density of states (DOS). The SPSF of the wire in momentum space is defined as

$$\begin{aligned} A_w(\omega, k_x) &= \sum_{\alpha} |\langle \alpha | d_{wk_x\sigma}^{\dagger} | 0 \rangle|^2 \delta(\omega - E_{\alpha} + E_0) \\ &+ \sum_{\alpha} |\langle \alpha | d_{wk_x\sigma} | 0 \rangle|^2 \delta(\omega + E_{\alpha} - E_0) \end{aligned} \quad (3.53)$$

where  $|\alpha\rangle$  and  $E_\alpha$  are the many-body eigenstates and eigenvalues of the wire-substrate Hamiltonian (3.51) but with  $N_{\text{leg}}$  substitute  $N_{\text{imp}}$ .  $|0\rangle$  and  $E_0$  are the ground state and its eigenenergy. The SPSF takes the same form for the substrate but averaged over the legs that represent the substrate, i.e.

$$(N_{\text{leg}} - 1)A_s(\omega, k_x) = \sum_{\alpha k_y k_z} |\langle \alpha | d_{\text{bk}\sigma}^\dagger | 0 \rangle|^2 \delta(\omega - E_\alpha + E_0) + \sum_{\alpha k_y k_z} |\langle \alpha | d_{\text{bk}\sigma} | 0 \rangle|^2 \delta(\omega + E_\alpha - E_0) \quad (3.54)$$

where  $b = s$  indicates the metallic substrate band while  $b = c$  or  $v$  indicate the conduction or valence band of the insulating substrate. By substituting  $d_{\text{wk}\sigma}^\dagger$  and  $d_{\text{bk}\sigma}^\dagger$  with  $f_{k_x n \sigma}^\dagger$  (similarly  $d_{\text{wk}\sigma}$  and  $d_{\text{bk}\sigma}$  with  $f_{k_x n \sigma}$ ) one can define the  $k_x$ -resolved spectral function  $A(\omega, k_x, n)$  for each leg  $n \geq 0$  where  $A(\omega, k_x, n = 0) = A_w(\omega, k_x)$  and the average over all  $n \geq 1$  provides the  $k_x$ -resolved spectral function of the substrate  $A_s(\omega, k_x)$ . Thus, the DOS of the wire or the substrate are defined as

$$D_{w,s}(\omega) = \frac{1}{L_x} \sum_{k_x} A_{w,s}(\omega, k_x). \quad (3.55)$$

By taking the normalized total DOS (i.e. calculated for the whole system) of the NLM

$$D(\omega) = \frac{D_w(\omega) + (N_{\text{leg}} - 1)D_s(\omega)}{N_{\text{leg}}} \quad (3.56)$$

one can see that the spectral weight of the wire is quite smaller than the substrate spectral weights and they become negligible for  $N_{\text{leg}} \gg 1$ .

### 3.3.1 Noninteracting wire

The possibilities and limitations of truncating the full 2D ladder system into a few-leg NLM ladder are analyzed here by comparing the SPSF and DOS of both cases. The subsystem Hamiltonians  $H_{k_x}$  in the chain representation (3.33) are truncated by projecting them onto the first  $N_{\text{leg}}$  Lanczos vectors subspace. This gives a way to define the SPSF and DOS for the NLM as

$$A_w(\omega, k_x) = \sum_{\lambda=1}^{N_{\text{leg}}} |\psi_{\lambda, k_x}(n=0)|^2 \delta(\omega - E_{\lambda, k_x}), \quad (3.57)$$

$$D_w(\omega) = \frac{1}{L_x} \sum_{k_x} A_w(\omega, k_x), \quad (3.58)$$

$$A_s(\omega, k_x) = \frac{1}{N_{\text{leg}} - 1} \sum_{\lambda=1}^{N_{\text{leg}}} \sum_{n=1}^{N_{\text{leg}}-1} |\psi_{\lambda, k_x}(n)|^2 \delta(\omega - E_{\lambda, k_x}) \quad (3.59)$$

and

$$D_s(\omega) = \frac{1}{L_x} \frac{1}{N_{\text{leg}} - 1} \sum_{k_x} \sum_{n=1}^{N_{\text{leg}}-1} A_s(\omega, k_x). \quad (3.60)$$

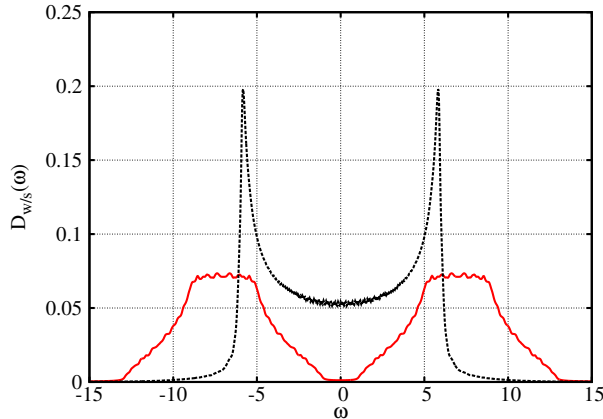


Figure 3.4: DOS of a noninteracting wire on an insulating 3D substrate with  $N_{\text{leg}} = N_{\text{imp}} = 513$ . The DOS in the wire [ $D_w(\omega)$ , dotted black line] and in the substrate [ $D_s(\omega)$ , solid red line]. The other parameters are given in the text. This figure is adapted from Ref [49].

$E_{\lambda,k_x}$  is the  $\lambda$ -th single-particle eigenenergy which corresponds to the wave vector  $k_x$  in the chain representation and  $\psi_{\lambda,k_x}(n)$  is the  $\lambda$ -th single-particle eigenstate which corresponds to the  $n$ -th shell of the same wave vector  $k_x$ . The substrate conduction and valence band hopping terms are chosen to be symmetric, i.e.  $t_c = t_v = t_s$ , for all cases discussed in the remaining parts of the thesis unless otherwise clearly mentioned. Moreover, they are chosen as the energy unit, i.e.  $t_s = 1$ . Similarly, the wire-substrate coupling is chosen to be symmetric i.e.  $t_{wc} = t_{wv}$ , and it is denoted  $t_{ws}$ . The potentials for substrate valence and conduction bands are chosen to satisfy the condition  $\epsilon_s = \epsilon_c = -\epsilon_v = 7$ , which opens an indirect gap  $\Delta_s = 2\epsilon_s - 12t_s = 2$  and a direct gap  $\Delta(k_x) = 2\epsilon_s - 8t_s = 6$  for vanishing wire-substrate hybridization. For  $N_{\text{leg}} = N_{\text{imp}}$ , i.e. for the full system,  $\psi_{\lambda,k_x}(n)$  is equivalent to  $\psi_{\lambda,k_x}(k_x, y, z)$  in a mixed representation where  $(k_x, 0, 0)$  corresponds to the wire and  $(k_x, y \neq 0, z > 0)$  corresponds to the substrate. In the present calculations the mixed representation is used to calculate the SPSF and DOS for the full noninteracting wire-substrate model. As mentioned before, for some model parameters there are eigenstates of the wire-substrate Hamiltonian which are restricted in the wire (or close to it) if they correspond to eigenenergies within the substrate band gap. This restriction results in finite spectral weights  $|\psi_{\lambda,k_x}(n)|^2$  for  $n = 0$  or small values of  $n$  when  $N_{\text{imp}} \rightarrow \infty$ . Therefore, these eigenstates form a 1D tight-binding subsystem which disperse in the wire direction ( $k_x$  direction) and crosses the Fermi level at two Fermi wave numbers. As discussed in the introduction, the construction of the Luttinger liquid rely on the dispersion linearization within the vicinity of the two Fermi wave vectors in the 1D metallic chain [4]. Therefore, it is expected that an effective one-dimensional wire coupled to a semiconducting substrate is possible as long as the Fermi level is situated within the substrate band gap. Hence, these considerations have been taken into account to select the intra-wire hopping  $t_w = 3$  and the wire-substrate hybridization  $t_{ws} = 0.5$ . The Fermi energy  $\epsilon_F = 0$  corresponds to half-filling and the chosen system sizes are  $L_x = 256, L_y = 32$  and  $L_z = 8$ . Parts of the wire dispersion away from the Fermi wave vectors, i.e.  $k_x \approx \pm\pi$  or  $k_x \approx 0$ , are allowed to mix with the valence or conduction bands of the full wire-substrate system.

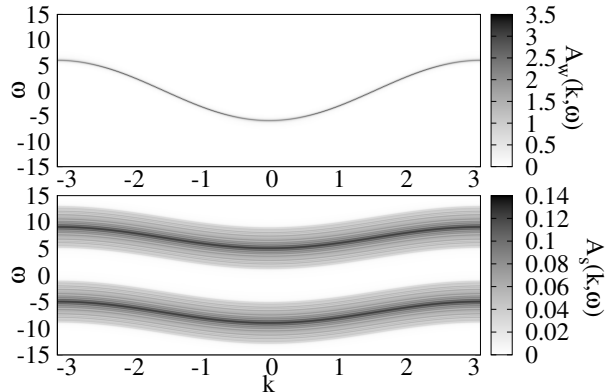


Figure 3.5: Spectral functions of a noninteracting wire on an insulating 3D substrate with  $N_{\text{leg}} = N_{\text{imp}} = 513$ . The spectral function in the wire [ $A_w(\omega, k_x)$ , top] and in the substrate [ $A_s(\omega, k_x)$ , bottom]. The other parameters are given in the text. This figure is published in Ref [49].

Fig. 3.4 displays the DOS profile for the wire (dotted black line) and for the substrate (red line). The DOS spectrum of the wire shows clear metallic 1D profile featured by square-root singularities close to  $\pm 2t_w$ . The substrate spectrum reveals a 3D profile with a gap between valence and conduction bands. This distinctive difference between the wire and substrate bands is clear despite of the overlap of both DOSs for wide range of energies. These results are confirmed in Fig. 3.5 which displays the SPSF. The upper panel in this figure exhibits a cosine-like  $k_x$ -resolved dispersion associated to the wire similar to Eq. (3.18). The intrinsic width in this band is due to the hybridization with the substrate. This band crosses the Fermi level  $\epsilon_F = 0$  in  $k_x \approx \frac{\pi}{2}$  at half filling. The lower panel shows two continua of the valence and conduction bands with an indirect band gap close to  $2t_s$  and a constant direct gap close to  $6t_s$ . These results clearly demonstrate that the 1D feature of the wire is preserved for weak wire-substrate hybridizations. There is a weak effect on the spectral weight of the dispersion that mixed with the substrate continua far from the Fermi energy. The continuous rugged DOS curves are the results of finite size effects and  $\delta$ -peak broadening using a Lorentzian with width  $\eta = 0.1$ . The impact of reducing the number of legs is demonstrated by performing the same calculations of the DOS and SPSF for the Hamiltonian (3.51) truncated to NLM with 51 legs and 3 legs, respectively. The intra-wire hopping keeps the value  $t_w = 3$ . The rest of the ladder system which represents the semiconducting substrate controlled by the substrate intra-leg hopping  $t_s$ , the nearest neighbor hopping  $t_{n+1}^{\text{rung}}$  and the wire-substrate hybridization  $\Gamma$ . For the 3-leg NLM  $\Gamma = \sqrt{2}t_{ws}$  and  $t_1^{\text{rung}} = \sqrt{3t_s^2 + \epsilon_s^2}$  while for larger number of legs  $t_{n+1}^{\text{rung}}$  is determined using the Lanczos algorithm it described in Sec. 3.2.2. The number of legs in the NLM must be an odd number due to the required symmetric representation of the conduction and valence bands. Each site in the substrate is described using two orbitals, one for the conduction band and the other for the valence band. On the other hand, each site in the wire has just one orbital. This results in an odd total number of sites in the chain representation and, hence, odd number of legs in the 2D ladder system, which requires an odd number of legs (at least 3 legs) in the NLM to reproduce gapped substrate bands. The results are shown in Figs. 3.6 and 3.7. Both figures reveal



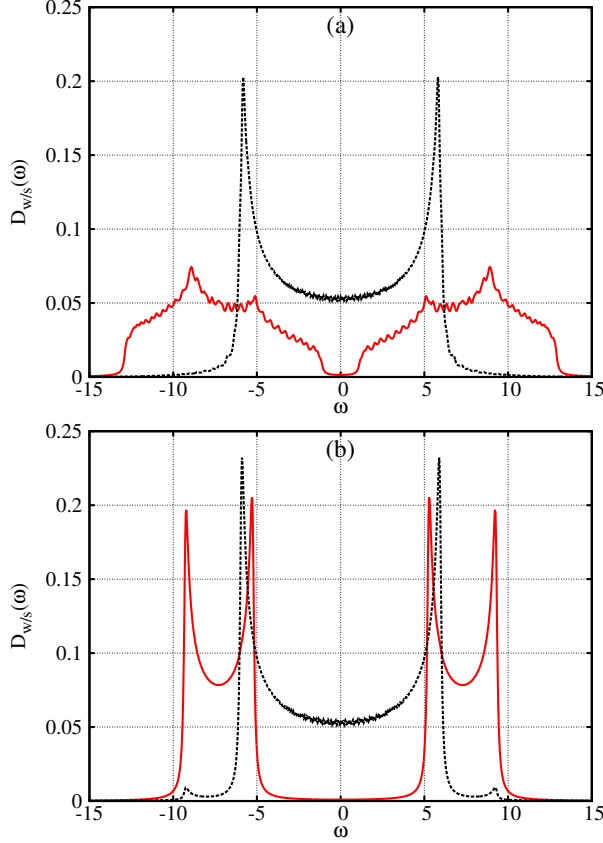


Figure 3.6: DOS of a noninteracting wire on an effective ladder model with (a)  $N_{\text{leg}} = 51$  legs and (b)  $N_{\text{leg}} = 3$ . The DOS in the wire [ $D_w(\omega)$ , dotted black line] and in the substrate [ $D_s(\omega)$ , solid red line]. The other parameters are given in the text. These figures are adapted from Ref [49].

little effect on the wire DOS spectrum and SPSF spectrum for both system widths. The less affected parts are close to the Fermi energy. However, the substrate DOS spectrum and SPSF continuum display very clear differences from the full wire-substrate results. The DOS in the substrate shown in Fig. 3.6(a) for the 51-leg ladder is different from the DOS in Fig 3.4. However, the energy range of the conduction and valence bands as well as the substrate band gap are reproduced almost correctly for the 51-leg NLM. In Fig. 3.6(b), the 3-leg NLM only shows two-leg ladder bands for the substrate with typical van Hove singularities distributed symmetrically around the Fermi energy. Moreover, the band gap in the 3-leg ladder is clearly enlarged with respect to the band gap in the full system. This gap enlargement is due to the reduction of the original quasi-dimerized long chain described in the chain representation (see Sec. 3.2.2) into only a single trimer which produces a 3-leg ladder in the real-space representation. The SPSF in Fig. 3.7 confirms these results. The spectral weight distribution of the substrate in the 51-leg ladder, Fig. 3.7(a), is clearly different from the spectral weight distribution in the full wire-substrate system but it reproduces the energy ranges and the band gap of the original system. Furthermore, it is also clear in Fig. 3.7(b) that the two valence and conduction bands are distributed symmetrically around the Fermi energy in the 3-leg NLM with the same band gap enlargement as in the DOS in Fig. 3.6(b). The wire dispersion is almost

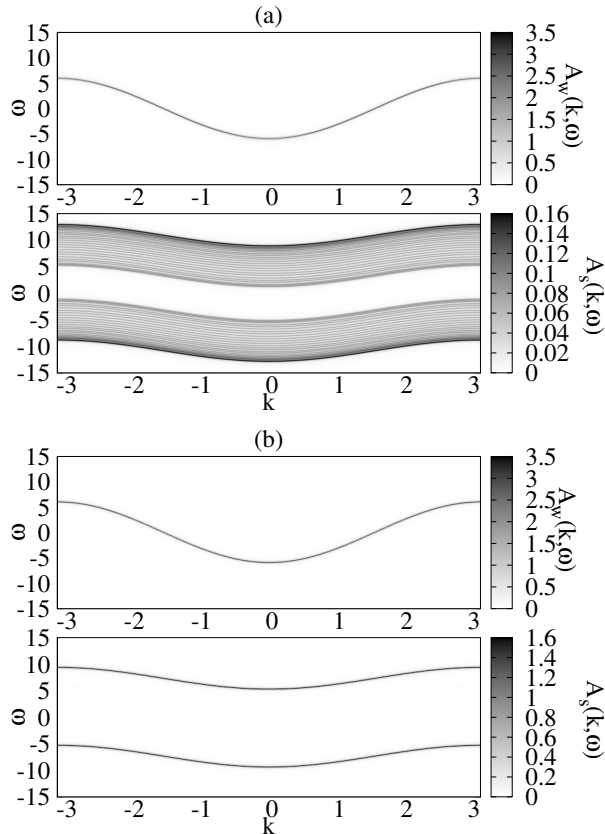


Figure 3.7: Spectral functions of a noninteracting wire on an effective ladder model with (a)  $N_{\text{leg}} = 51$  legs and (b)  $N_{\text{leg}} = 3$ . The spectral function in the wire [ $A_w(\omega, k_x)$ , top (a) and (b)] and in the substrate [ $A_s(\omega, k_x)$ , bottom (a) and (b)]. The other parameters are given in the text. These figures are published in Ref [49].

preserved in Fig. 3.7(b). The very weak influence of truncating the number of legs on the spectral properties close to the Fermi energy suggests the validity of the NLM even for 3-leg ladder system at least qualitatively.

The dispersive band within the substrate band gap persists for strong wire-substrate hybridization but accompanied with two other bands situated symmetrically around the middle of the substrate band gap. The separation between these two additional bands is larger than the substrate band gap and increases with  $t_{\text{ws}}$  until for strong enough hybridization (e.g.,  $t_{\text{ws}} = 8$ ) they split from the continua of the valence and conduction bands. The central dispersive band within the substrate band gap has eigenstates which localize on the wire or on its nearest neighbor substrate sites but delocalize in the wire direction. This means that the wire-substrate model preserves the 1D features even for strong wire-substrate hybridization. The formation of the three bands in the strong hybridization can be illustrated by taking the limit  $\epsilon_c - \epsilon_v, t_{\text{ws}} \gg t_w \gg t_s$ . In this case each wire site builds a trimer with its closest two nearest-neighbor substrate sites due to the strong wire-substrate hybridization and rung hopping (remember that each substrate site has two orbitals). Then the wire hopping  $t_w$  forms a three-leg ladder system from these trimers which then hybridize slightly by weak  $\sim t_s$  with the rest of the substrate.

It should be indicated that all single-electron eigenstates are delocalized in the full

wire-substrate system if the substrate is metallic. This is because the 1D wire band is buried in the substrate metallic continua. Hence one can not observe 1D features. Moreover, the spectral properties at Fermi energy are not preserved while varying the number of legs in the NLM Eq.(3.51). This makes the few-leg truncation invalid for metallic substrates.

### 3.3.2 Interacting wire : testing with quantum Monte Carlo

The former discussion demonstrates the usefulness of the NLMs for the noninteracting case. This and the next subsections are devoted to the applicability of the NLM to a correlated wire described by the one-dimensional Hubbard model with repulsive interaction, i.e.  $U > 0$ . The first subsection compares the correlated wire on 3D semiconducting substrate to the NLM with  $N_{\text{leg}} = 3$ . The second subsection analyzes the finite size effects for correlated NLM with several widths.

The correlated NLM is described using the first few legs in the ladder Hamiltonian (3.51) where the first leg represents a correlated wire using the 1D Hubbard model. The wire-substrate coupling and the substrate parameters are similar to those described in the noninteracting case in addition to the on-site Coulomb interaction  $U = 4$ . The half-filled system corresponds to the number of electrons [in the full wire-substrate model]  $N_p = N_{\text{imp}}L_x$  and  $N_p = N_{\text{leg}}L_x$  for the NLM. The full system can be doped away from half filling using a finite bulk doping  $y \in (-1, 1)$  such that  $N_p = (1 + y)N_{\text{imp}}L_x$  electrons are in the full wire-substrate model or  $N_p = (1 + y)N_{\text{leg}}L_x$  electrons in the NLM. This produces a large shift of the chemical potential which then lies within one of the substrate bands. Therefore, the substrate is metallic which is not relevant to the experiments with semiconducting substrates nor applicable to the NLM approximation. A relevant doping is achieved by a finite wire doping  $y_w \in (-1, 1)$  which corresponds to  $N_p = N_{\text{imp}}L_x + y_wL_x$  for the full wire-substrate model or  $N_p = N_{\text{leg}}L_x + y_wL_x$  for the NLM. This finite wire doping is equivalent to a vanishing bulk doping, i.e.  $y \approx 0$  and  $N_p/(N_{\text{imp}}L_x) \approx 1$ . Thus the finite wire doping is relevant to the experimental systems of atomic wire reconstructions discussed in Sec. 1.2. Each site in the wire has a potential  $\epsilon_w = -U/2$  to set the Hubbard upper and lower bands symmetrically around the substrate band gap at half filling.

The comparison between the correlated full wire-substrate model and the NLM was performed using results from the CT-INT method similarly to Sec. 2.4 by Martin Hohenadler. For the CT-INT calculations the full wire-substrate model has the dimensions  $L_x = L_y = 42$  and  $L_z = 10$  while the rest of the model parameters are equal to those chosen for the noninteracting case. The spectral function on the wire is defined similarly to Eq.(2.52) by performing the measurements using the wire operator  $d_{wk_x\sigma}$ . The spectral functions  $A(\omega, k_x, n)$  in the NLM and  $A_s(\omega, k_x, y, z)$  for specific chains in the substrate of the 3D wire-substrate model are obtained in a similar way. However, as calculations over the full substrate are expensive, the spectral functions are averaged over chains at the coordinates  $(y = y_0, z = 1)$  and  $(y = y_0 + L_y/2, z = L_z)$ . The calculations for the 3-leg NLM are averaged over the full ladder system. Fig. 3.8 demonstrates the results for the spectral functions  $A_w(\omega, k_x)$  and  $A_s(\omega, k_x, y = y_0, z = 1)$  of the full wire-substrate system compared with the spectral functions  $A_w(\omega, k_x)$  and  $A_s(\omega, k_x)$  of the 3-leg NLM. The calculations were done using a chemical potential on the wire  $\mu = 1.58$  for the NLM

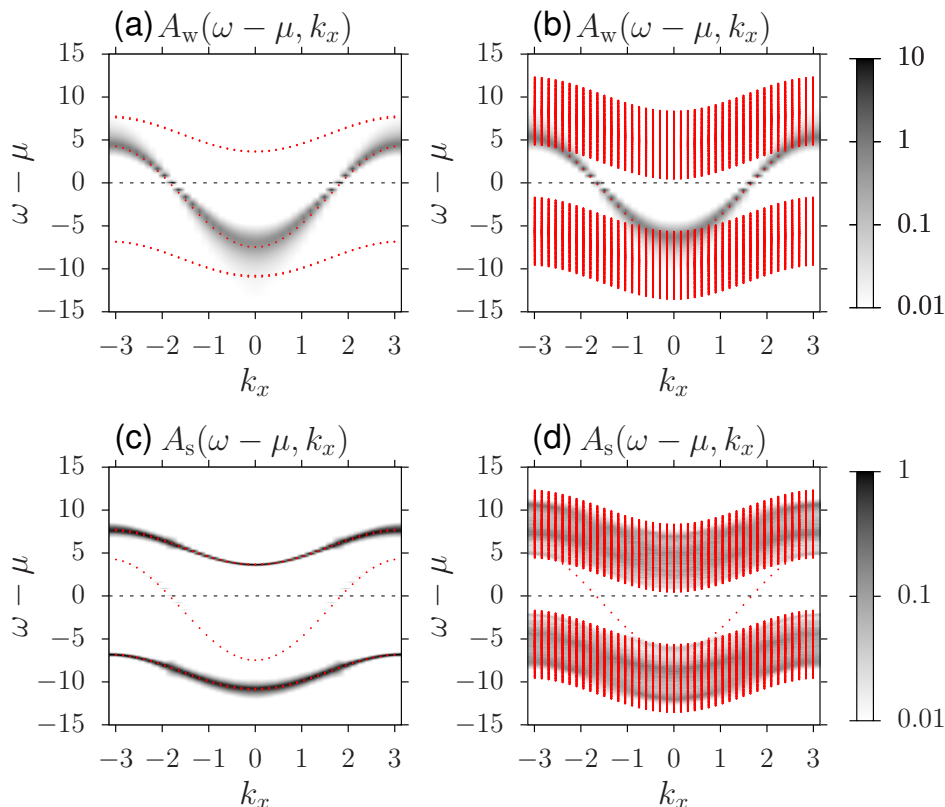


Figure 3.8: CT-INT QMC calculations with  $\beta = 15$  of spectral functions for an interacting wire with  $U = 4$ . A wire doping  $y_w \approx 12.5\%$  is obtained by tuning the chemical potential. Top: wire spectral function  $A_w(\omega, k_x)$  for (a) the three-leg NLM and (b) the 3D wire-substrate model. Bottom: (c) substrate spectral function  $A_s(\omega, k_x)$  for the three-leg NLM, (d) substrate spectral function  $A_s(\omega, k_x)$  of the full model averaged over the chains at the minimal and the maximal distance from the wire. The length  $L_x = 42$  is fixed for all cases. For the 3D substrate lattice,  $L_y = 42$  and  $L_z = 10$  are used. All other parameters are as in Figs. 3.5–3.7. Red symbols illustrate the noninteracting energy levels. Calculations and figures by Martin Hohenadler. The figure is published in Ref. [49].

and  $\mu = 0.60$  for the full model. The chemical potential in both cases corresponds to a total doping of 5.25(1) electrons (or  $y_w \approx 12.5\%$  for  $L_x = 42$ ). Fig. 3.8(a) and (b) reveal similarities between spectral functions of the wire close to Fermi level with gapless excitations for both the wire-substrate model and the NLM. The spectral functions of the substrate demonstrates clear difference between the wire-substrate model and the NLM but with vanishing spectral weight at the Fermi level. This is shown in Fig. 3.8(c) and (d). These results confirm the capability of the NLM to represent the low-energy excitations of the correlated metallic wire in the full wire-substrate model as in the noninteracting case.

### 3.3.3 Interacting wire : testing with DMRG

Similarly to the previous DMRG investigation of the asymmetric Hubbard ladder in Sec. 2.3 the DMRG method is used to investigate the correlated-wire NLM. The finite-system DMRG algorithm is used on NLM lattices with up to  $L_x = 200$  rungs at half filling and  $L_x = 208$  away from half filling in the 3-leg and 7-leg ladder cases. For the other system widths a length up to  $L_x = 128$  is used. All calculations for the NLM were performed using open boundary conditions and up to  $m = 2024$  density-matrix eigenstates yielding discarded weights smaller than  $10^{-6}$ . Truncation errors are investigated systematically by keeping variable numbers of density-matrix eigenstates and extrapolating ground-state energies to the limit of vanishing discarded weights. The resulting error estimates for gaps are shown in the figures when they are larger than the symbol sizes. The calculations have been performed using weak to intermediate interactions corresponding to  $U/t_w \lesssim 5$ . Charge, spin and single-particle excitations are defined using Eqs(2.39),(2.40) and (2.41). The mapping idea described in Sec. 3.2 produces a 2D ladder system while the finite-system DMRG method is appropriate for quasi-one-dimensional systems or ladder systems with several number of legs. Therefore, it is important to see how the finite-system DMRG results scale when increasing the system length  $L_x$  and the width  $N_{\text{leg}}$  in order to investigate the validity of the NLM as a good approximation of the wire-substrate model. It is known for 2D electron systems that DMRG is limited by an exponential increase in the required CPU time and memory as functions of the system width due to a rapid growth of entanglement [52]. However, the entanglement is related to the number of bands crossing the Fermi level in noninteracting systems [99], i.e. number of gapless excitation modes. This number is proportional to the system width in the homogeneous Hubbard ladder but it is just one band in the present NLM. Therefore, it is expected that increasing the system width in the correlated NLM should have less influence than increasing the width in homogeneous Hubbard ladder. To analyze the effect of width in correlated NLM, the charge gap is calculated for ladders with various lengths  $L_x$  and widths  $N_{\text{leg}}$  (the other gaps are discussed in details in the next chapter). In Fig. 3.9(a) the charge gap  $E_c$  is shown at half filling for  $U = 4$  and hybridization  $t_{\text{ws}} = 0.5$  as a function of the inverse ladder length  $1/L_x$  for different number of legs  $N_{\text{leg}}$ . In the 1D Mott insulators, e.g. the 1D Hubbard chain at half filling, charge and single-particle gaps decrease with the inverse of the system length toward finite values in the limit  $L_x \rightarrow \infty$ . Thus, extrapolation of the charge gap for each lattice width indeed gives finite and almost equal gaps for all  $N_{\text{leg}}$  for the chosen parameters. However, for other parameter sets, this extrapolation shows different behavior of the gap size depending on the lattice width  $N_{\text{leg}}$ . This variation in the finite-size scaling is related to the large variation in the effective substrate band gap with the number of legs which observed in the noninteracting NLM in Sec 3.3.1.

For 1D gapless electron systems, e.g. the 1D Hubbard model away from half filling, finite size gaps vanish linearly according to the conformal field theory analysis [4] such that

$$E_i = \frac{\pi v_i}{L_x} \quad (3.61)$$

for  $L_x \gg 1$ , where  $i = c, s$  or  $p$  and  $v_i$  is the velocity of the corresponding excitation. Therefore, Fig. 3.9(b) shows the charge gap away from half filling for  $U = 4$  and  $t_{\text{ws}} = 0.5$  as a function of the inverse ladder length for two different numbers of legs  $N_{\text{leg}}$ . The

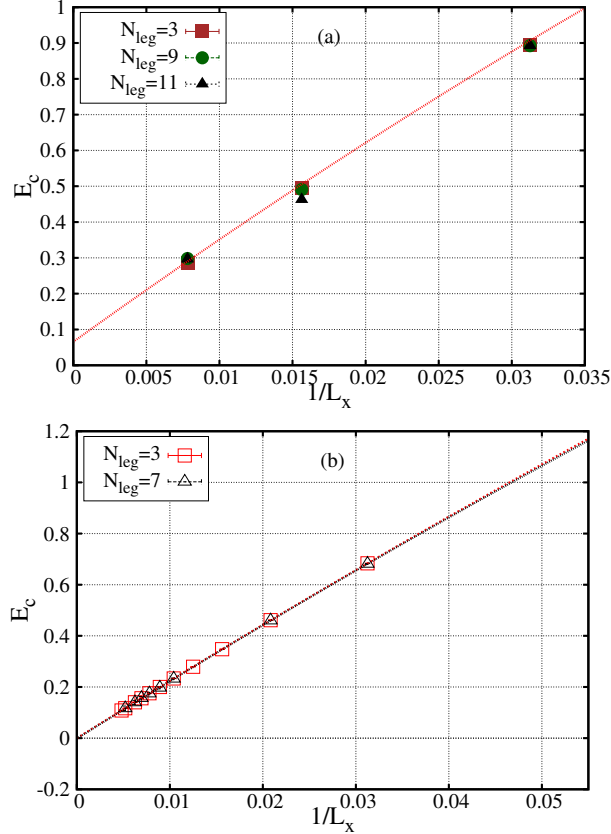


Figure 3.9: Charge gap (2.39) of the NLM calculated with DMRG (a) at half filling and (b) away from half filling as function of inverse ladder length  $1/L_x$  for different numbers of legs  $N_{\text{leg}}$ . The Hubbard coupling is  $U = 4$  and the hybridization is  $t_{\text{ws}} = 0.5$ . In (a) the line shows the finite-size gap of the half-filled 1D Hubbard model with open boundary conditions and a hopping  $t_w = 3$  while in (b) the lines are quadratic fits in  $1/L_x$ . These figures are adapted from Ref. [50].

charge gap vanishes linearly with  $1/L_x$  for a fixed number of legs. The velocities of charge, spin and single-electron excitations are calculated from the line slopes in the finite-size-scaling analysis. In a single noninteracting wire decoupled from the substrate charge, spin and single-electron velocities are equal to the Fermi velocity  $v_F = 2t_w \sin(k_F)$ , which is  $v_F = 2t_w = 6$  at half filling and  $v_F \approx 1.96t_w \approx 5.88$  at  $y_w = 12.5\%$  doping. The calculated velocity  $v_c$  does not change significantly with the number of legs  $N_{\text{leg}} \geq 3$  as shown in Fig. 3.9(b) for the chosen parameter set with  $v_c/v_F \approx 1.2$ . The DMRG calculations for gapless excitation modes are limited to a few values of  $N_{\text{leg}}$ , and hence, significant finite-size corrections are not excluded for larger numbers of legs beyond  $N_{\text{leg}} = 7$ .

It is clear that the finite-size extrapolation of the correlated NLM to the thermodynamic limit should be done by fixing the ratio  $N_{\text{leg}}/L_x$ . Such scaling of system width is difficult to handle for DMRG. Therefore, it is very hard to prove that the correlated NLM is a good quantitative approximation to the full wire-substrate model using only DMRG. But, nevertheless, the NLM shows that properties such as gapped vs. gapless excitations or excitations on the wires vs. on the substrate do not depend on the ladder width. Therefore, the correlated NLM gives a good qualitative approximation to the full

wire-substrate model.

There are several alternatives to the regular DMRG method to achieve larger number of legs using different representations of the NLM. One option is the two-step DMRG proposed in [100, 101] which is appropriate for ladder systems with weakly coupled legs. An other option is the DMRG method in momentum space [102, 103, 99] which has been used for weak electron-electron interaction to calculate momentum-space resolved observables. However, this option can not be applied directly to the NLM model due to the absence of translation invariance in the rung direction. Nevertheless, the construction of NLM in a mixed  $(k_x, y, z)$  representation results in  $yz$ -slices of the substrate which are decoupled from each other as it discussed in Sec. 3.2. Thus a version of DMRG in a mixed representation [99] can be used for the NLM in a  $(k_x, y, z)$  representation or a  $(k_x, n)$  representation, i.e. momentum space in the wire direction and Lanczos basis in the other directions. A third option is to consider each  $yz$ -slice in the mixed representation or each rung in the NLM as a one big site, i.e. with a large number of states, and use DMRG methods that treat systems with such big sites [104, 105, 106]. In general, the entanglement between the rungs in the substrate is expected to be smaller than between rungs in homogeneous ladder systems as discussed before. One interesting option is the application of field-theoretical approaches [107, 4, 108, 109] from the mixed representations  $k_x, y, z$  or  $k_x, n$ .

### 3.4 Summary

A model of correlated atomic wire on noninteracting substrate is constructed. This model is exactly mapped onto a 2D ladder system where the first leg corresponds to the wire and the rest describes degrees of freedoms on the substrate. It has been shown that the reduction of the 3D ladder to a few-leg ladder system is a good approximation for models with insulating substrates but not with metallic substrates. The resulting narrow ladder model can be investigated using methods for quasi 1D correlated electrons such as DMRG, QMC and field-theoretical methods.

# Chapter 4

## NLM for correlated Hubbard wires

In the former chapter the mapping of a 3D wire-substrate model into a 2D ladder system was established. The validity of the NLM was also tested for noninteracting as well as interacting wires. This chapter is devoted to further exploring the impact of wire-substrate hybridization on a correlated wire, namely, the 1D Hubbard model. The main idea is to use the well established knowledge about the 1D Hubbard model properties and to study how they are affected by the wire-substrate hybridization. Furthermore, it is interesting to investigate the properties and phases of the NLM. The numerical investigations are based on DMRG and CT-INT calculations. The CT-INT are done by Martin Hohenadler on the full wire-substrate model (3.1) and the NLM derived by keeping only a few legs in the Hamiltonian (3.51). DMRG calculations are done for the NLM. Most of the investigations presented here are published in Ref. [50].

Beside calculating charge (2.39), spin (2.40) and single-particle (2.41) excitations, DMRG is used to measure different densities and correlation functions similar to Eqs.(2.43) and (2.44). However, to adapt the notations for the wire-substrate model and the NLM, the following definitions are used. The total charge on leg  $n$  is defined as

$$C(n) = \left\langle \psi_{\text{GS}} \left| \sum_{x,\sigma} g_{xn\sigma}^\dagger g_{xn\sigma} \right| \psi_{\text{GS}} \right\rangle \quad (4.1)$$

while the total spin density is defined by

$$S(n) = \left\langle \psi_{\text{GS}} \left| \sum_{x,\sigma} \sigma g_{xn\sigma}^\dagger g_{xn\sigma} \right| \psi_{\text{GS}} \right\rangle. \quad (4.2)$$

$|\psi_{\text{GS}}\rangle$  is the ground state for a given number of electrons of each spin  $M_\sigma$  while the operators  $g_{xn\sigma}^\dagger$  ( $g_{xn\sigma}$ ) create (annihilate) electrons with spin  $\sigma$  at position  $x$  in the  $n$ -th leg, see Eq.(3.38). Measurements of charge and spin densities indicate how they distribute in the ground state among legs. Additionally, variations  $\Delta C(n)$  and  $\Delta S(n)$  of these quantities for  $M_\sigma \pm 1$  indicate whether the lowest charge, spin and single-particle excitations (defined by the correspondent gaps) are mostly localized on the wire or distributed in the substrate.



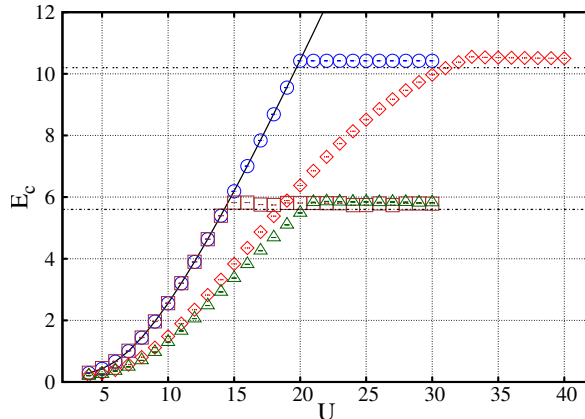


Figure 4.1: Charge gaps (2.39) calculated with DMRG at half filling as a function of the Hubbard coupling  $U$ . Circles and diamonds display results of a three-leg NLM with  $t_{ws} = 0.1$  and  $t_{ws} = 2$ , respectively. Squares and triangles display results for a seven-leg NLM with  $t_{ws} = 0.1$  and  $t_{ws} = 2$ , respectively. The solid line indicates the Mott gap of the 1D Hubbard chain with a hopping  $t_w = 3$ . The horizontal dashed lines indicate the effective substrate band gaps  $\Delta_s(N_{\text{leg}} = 3) \approx 10$  and  $\Delta_s(N_{\text{leg}} = 7) \approx 5.5$  of the noninteracting NLM. This figure is adapted from Ref. [50].

Similarly, the charge correlation function for the wire is defined by

$$F_c(x - x') = \left\langle \sum_{\sigma} n_{wx\sigma} \sum_{\sigma} n_{wx'\sigma} \right\rangle - \left\langle \sum_{\sigma} n_{wx\sigma} \right\rangle \left\langle \sum_{\sigma} n_{wx'\sigma} \right\rangle \quad (4.3)$$

while the spin correlation function is

$$F_s(x - x') = \left\langle \sum_{\sigma} \sigma n_{wx\sigma} \sum_{\sigma} \sigma n_{wx'\sigma} \right\rangle. \quad (4.4)$$

The expectation values are calculated using the ground state  $|\psi_{\text{GS}}\rangle$ . A discussion of two cases, namely, the half-filled lattice as well as the lattice away from half filling, are presented in the following sections.

## 4.1 NLM for insulating Hubbard wire

The 1D Hubbard model at half filling is a paramagnetic Mott insulator for any finite electron-electron interaction, i.e.  $U > 0$ . Therefore, for  $t_{ws} = 0$ , the wire in the wire-substrate and the NLM models has a Mott gap that depend on the Hubbard interaction  $U$ . This gap can be calculated using Bethe-ansatz methods [10] or DMRG. Hence, it is interesting to see to what extent the correlated NLM and the wire-substrate model change or preserve the 1D Mott insulating features for  $t_{ws} > 0$ . In Fig. 4.1, the charge gap of two NLM lattices (3-leg and 7-leg ladders) are compared with the 1D Hubbard chain at half

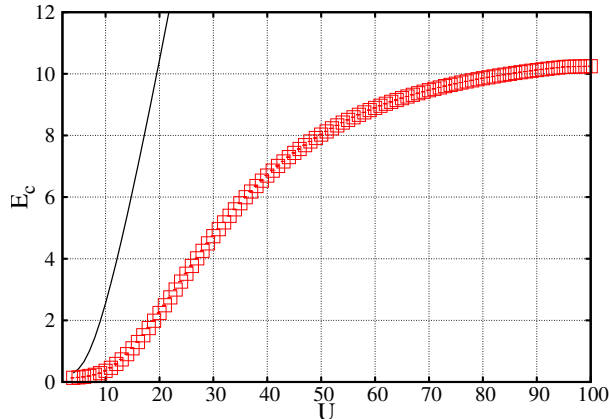


Figure 4.2: Charge gaps (2.39) calculated with DMRG at half filling as a function of the Hubbard coupling  $U$  for a three-leg NLM with  $t_{\text{ws}} = 4$  (squares) The solid line indicates the Mott gap of the 1D Hubbard chain with a hopping  $t_w = 3$ .

filling. The system length is  $L_x = 128$ . The charge gap has been calculated as a function of the Hubbard interaction  $U$  with two values of the wire-substrate hybridization,  $t_{\text{ws}} = 0.1$  and 2, for both ladder systems. For  $t_{\text{ws}} = 0.1$ , the charge gaps of both ladder systems are very close to the gap of the 1D Hubbard chain up to a value of the interaction  $U = U_c$ . For larger  $U$ , they saturate to a fixed gap value that depends on the number of legs. The saturation gap is close to the band gap of the corresponding noninteracting NLM. This saturation gap decreases upon increasing the number of legs and, eventually, it should reach the value of the band gap of the full substrate. For  $t_{\text{ws}} = 2$ , both ladder systems exhibit reduced charge gaps in comparison to the Mott gap of the 1D Hubbard chain at half filling. However, both systems reach similar value of gap saturation as for  $t_{\text{ws}} = 0.1$  but for a larger value of the interaction  $U$ . The behavior of the weakly hybridized ladder system ( $t_{\text{ws}} = 0.1$ ) can be explained in a simple way. The wire chain has a Mott gap at half filling which is very close to the Mott gap of the half filled 1D Hubbard model. The band gap of the NLM substrate is much larger than the wire Mott gap for weak interaction  $U$  and, thus, the lowest charge excitations localize in the wire in this case. However, by increasing the interaction  $U$  the wire Mott gap increases until it reaches the value of the NLM substrate band gap. For a wire Mott gap larger than the NLM substrate band gap the lowest charge excitation delocalizes in the NLM substrate and therefore the NLM charge gap saturates to its substrate band gap. The same explanation is applied to the NLM ladders with larger wire-substrate hybridization, e.g.  $t_{\text{ws}} = 2$ , but apparently, the wire-substrate hybridization is responsible for reducing the Mott gap in the wire, and hence, moving the saturation to a larger value  $U_c$ . This is confirmed in Fig. 4.2 which shows the charge gap as a function of the Hubbard interaction  $U$  for  $t_{\text{ws}} = 4$  in comparison to the 1D Hubbard model. In this case, the saturation does not clearly appear up to vary large values of  $U$ . Apparently, the saturation is developing smoothly in this case. The single-particle gap of the correlated NLM behaves similar to the charge gap.

The 1D Hubbard model has gapless spin excitations at half filling with spin velocities which decrease for increasing interaction  $U$  [11]. Fig. 4.3 shows spin gap extrapolations at half filling as functions of  $1/L_x$ . These calculations are done for correlated NLM with

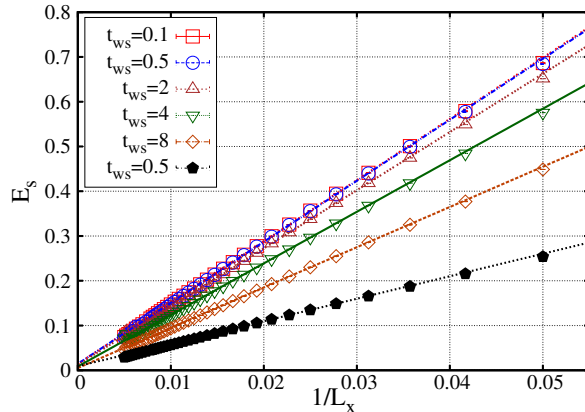


Figure 4.3: Spin gaps (2.40) of the half-filled three-leg NLM calculated with DMRG as a function of the inverse ladder length for Hubbard couplings  $U = 4$  (open symbols) and  $U = 24$  (filled symbols) and various hybridization strengths  $t_{\text{ws}}$ . This figure is adapted from Ref. [50].

$U = 4$  and  $t_{\text{ws}} = 0.1, 0.5, 2, 4$  and  $8$  which correspond to  $U < U_c$  as well as for  $U = 24$  and  $t_{\text{ws}} = 0.5$  which correspond to  $U > U_c$ . Indeed, the correlated NLM at half filling has gapless spin excitations for all parameter sets shown. As shown above increasing the wire-substrate hybridization decrease the charge gap of the correlated NLM which implies reduction of the strength of the effective electron-electron interaction. However, the calculated spin velocities reduce with increasing wire-substrate hybridization, which contradicts this implication. This result suggests that the correlated NLM deviates qualitatively from the physics of the 1D Hubbard model for strong wire-substrate hybridizations.

Charge and spin density distributions at half filling have no significant features but more insights can be gained by analyzing the variations of these densities from half filling caused by charge, spin and single-particle lowest excitations. Fig. 4.4 displays the variations of the charge density  $\Delta C(0) = C(0) - L_x$  due to one or two electrons added to half filling. These measurements are done on the wire leg, i.e.  $n = 0$ . It is clear that most of the lowest charge excitations are localized on the wire for  $U < U_c$  but delocalized on the noninteracting substrate legs, i.e.  $n > 0$ , for  $U > U_c$ . The variations of the spin density  $S(n)$  for the two-particle excitation is almost zero for all cases while for the single-particle excitation the spin density goes to the wire for  $U < U_c$  but on the substrate noninteracting legs for  $U > U_c$ . However, for the triplet excitation the variations of  $S(n)$  show localization of the lowest spin excitations on the wire leg for any  $U \geq 4$ . The behavior of  $C(n)$  and  $S(n)$  variations are clearer in the case of weak hybridizations  $t_{\text{ws}}$ . Moreover, this behavior is also seen in correlated NLM with larger number of legs, e.g.  $N_{\text{leg}} = 7$ . Therefore, these results for the correlated NLM at half filling suggest two phases, a quasi-1D Mott insulator with gapless spin excitations for  $U < U_c$  and a band insulator for  $U > U_c$ . For a fixed wire-substrate hybridization  $t_{\text{ws}}$  (at least for  $t_{\text{ws}} < 4$ ), the correlated NLM exhibits a transition from a Mott insulator to a band insulator by increasing the Hubbard interaction  $U$ . Nevertheless, the band insulator phase contains embedded magnetic impurities (or embedded Heisenberg chain) represented by the spins of the wire electrons. These embedded magnetic impurities are responsible for the gapless

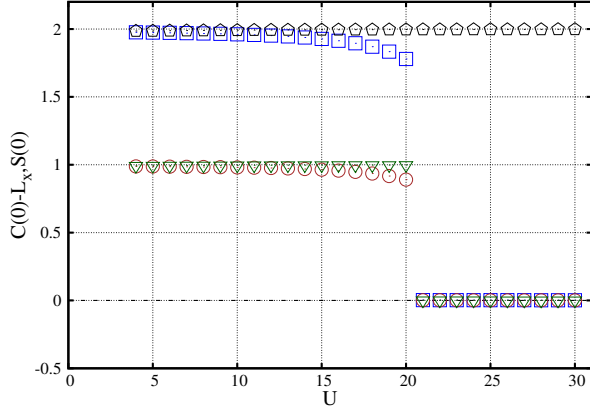


Figure 4.4: Variations of the total charge  $\Delta C(0) = C(0) - L_x$  and spin  $\Delta S(0) = S(0)$  on the wire leg calculated with DMRG for the lowest charge (squares), spin (pentagons), and single-particle (circles and triangles, respectively) excitations of the half-filled three-leg NLM as a function of the Hubbard coupling  $U$  for  $t_{ws} = 0.5$ . This figure is adapted from Ref. [50].

spin excitations. From the analysis of the noninteracting case, the band gap of the full wire-substrate model is  $\Delta_s = 2$  which is equal to a Mott gap produced by a wire with Hubbard interaction  $U \approx 9$  for weak wire-substrate hybridization. Although it is hard to simulate the current correlated NLM with large number of legs using DMRG, the critical value  $U_c$  remains finite for all investigated ladder widths and is expected to be  $U_c \approx 9$  for the full correlated wire-substrate model at half filling. However, the value of  $U_c$  is larger for larger hybridization  $t_{ws}$  in the full wire-substrate model.

The 1D Hubbard model at half filling undergoes a phase transition from a metallic Fermi gas at  $U = 0$  to a Mott insulator at  $U > 0$ . It is assumed that similar transition occur in the NLM but the critical value of Hubbard interaction  $U$  can not be identified using only DMRG calculations. However, it is probably possible to study this transition using methods suitable for weakly interacting quasi-one-dimensional systems such as field-theoretical approaches [107, 4, 110, 108, 109].

As in the previous chapter, the grand canonical variant of the CT-INT method with an inverse temperature  $\beta$  is used to shed more light on the DMRG results. The chemical potential is adjusted to  $\mu = 0$  which corresponds to half-filled systems. Beside the SPSF that can be measured in the angle-resolved photoemission spectroscopy, the dynamic charge and spin structure factors have been calculated. The definition of the dynamic charge ( $\alpha = \rho$ ) and spin ( $\alpha = \sigma$ ) structure factors of the wire is

$$S_\alpha(\omega, k_x) = \frac{1}{Z} \sum_{ij} |\langle i | \hat{S}_\alpha(k_x) | j \rangle|^2 (e^{-\beta E_i} + e^{-\beta E_j}) \times \delta(E_j - E_i - \omega). \quad (4.5)$$

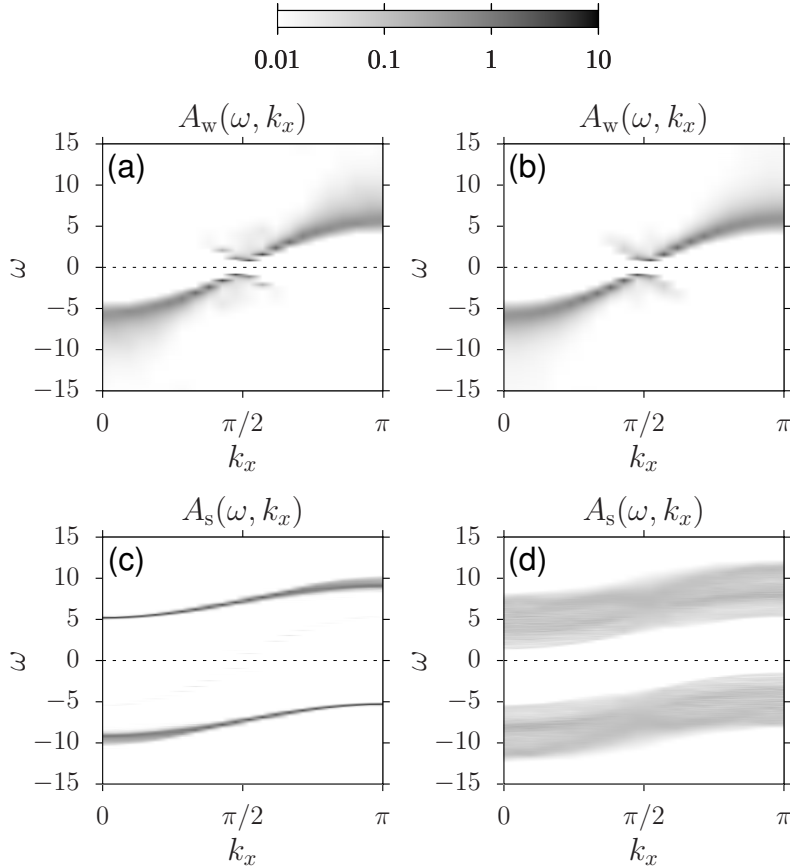


Figure 4.5: (a) and (b) show spectral functions on the wire  $A_w(\omega, k_x)$  while (c) and (d) are on the substrate  $A_s(\omega, k_x)$ . These calculations are done using CT-INT simulations for  $U = 8$ ,  $t_{\text{ws}} = 0.5$ ,  $\beta = 15$ , and  $L_x = 42$ . The chemical potential is adjusted to  $\mu = 0$ , corresponding to half-filling. Panels (a) and (c) show results for the three-leg NLM, panels (b) and (d) for the 3D wire-substrate model ( $L_y = 42$ ,  $L_z = 10$ ). Calculations and figure by Martin Hohenadler. The figure is published in Ref. [50].

with

$$\begin{aligned}\hat{S}_\rho(k_x) &= \frac{1}{\sqrt{L_x}} \sum_x e^{ik_x x} \sum_\sigma c_{\text{wx}\sigma}^\dagger c_{\text{wx}\sigma}, \\ \hat{S}_\sigma(k_x) &= \frac{1}{\sqrt{L_x}} \sum_x e^{ik_x x} \sum_\sigma \sigma c_{\text{wx}\sigma}^\dagger c_{\text{wx}\sigma}.\end{aligned}\quad (4.6)$$

where  $|i\rangle$  is an eigenstate with eigenenergy  $E_i$ . As mentioned previously, the dynamic charge structure factor can be measured in the electron-energy-loss spectroscopy experiments and the dynamic spin structure factor can be measured in the inelastic-neutron-scattering experiments. Both of them are resulted to the charge and spin gaps, respectively, while the SPSF is resulted to the single-particle gap. The CT-INT SPSF of the 3-leg NLM and the 3D wire-substrate model are displayed in Fig. 4.5. The calculations have been done for  $U = 8$  and  $t_{\text{ws}} = 0.5$ . Fig. 4.5(a) displays the SPSF of the wire [ $A_w(\omega, k_x)$ ] in the 3-leg NLM and Fig. 4.5(b) displays the same spectral function in the

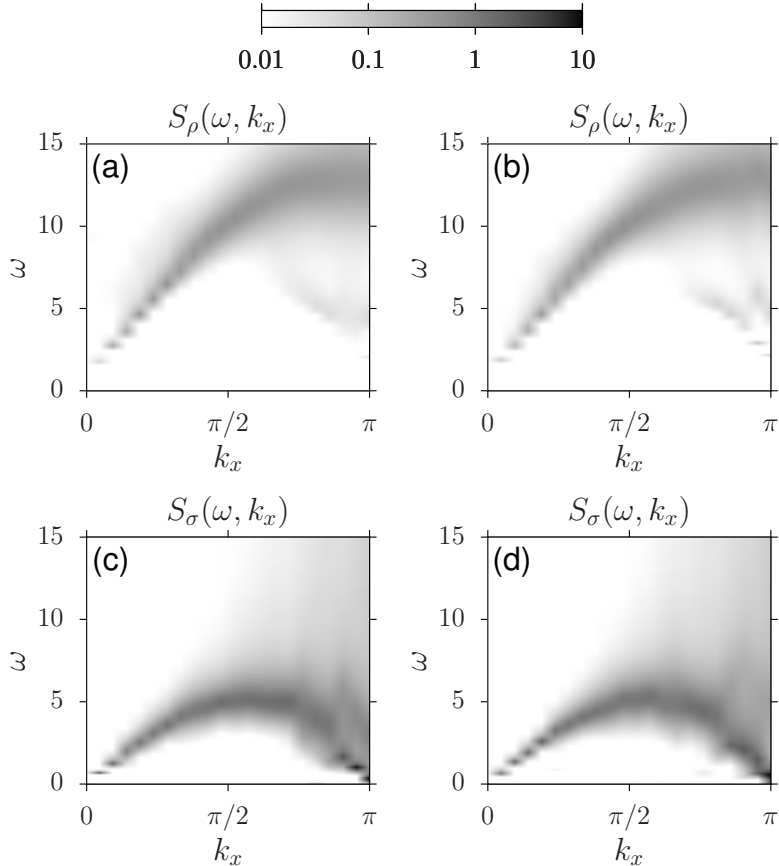


Figure 4.6: (a) and (b) show the dynamic charge structure factor  $S_\rho(\omega, k_x)$  while (c) and (d) show the dynamic spin structure factor  $S_\sigma(\omega, k_x)$ . All cases are calculated using CT-INT simulations on the wire for the same parameters as in Fig. 4.5. Panels (a) and (c) show results for the three-leg NLM, panels (b) and (d) for the 3D wire-substrate model. Calculations and figure by Martin Hohenadler. The figure is published in Ref. [50].

3D wire-substrate system. They are clearly similar even though the SPSF of the substrate  $[A_s(\omega, k_x)]$  in Fig. 4.5(c) and (d) are quite different from each other in the two systems. The wire spectral functions in Fig. 4.5(a) and (b) are quite similar (within the numerical accuracy) to those of the 1D Mott insulator [111, 77, 112, 113] with a gap closely related to the gap calculated using DMRG in Fig.4.1. The substrate band gap is also clear in the 3D substrate SPSF shown in Fig. 4.5(d) to be  $\Delta_s(N_{\text{leg}} = 3) \approx 2$ . This band gap is enlarged in Fig. 4.5(c) of the 3-leg NLM to be  $\Delta_s(N_{\text{leg}} = 3) \approx 10$ . The low-energy single-particle excitations of the 3-leg NLM remain in the wire which is also the case for the 3D wire-substrate model. Fig. 4.6 demonstrates the dynamic charge and spin structure factors calculated for the wire using the same system parameters as in Fig. 4.5. Both structure factors display similar spectra for the 3-leg NLM and the 3D wire-substrate model. Moreover,  $S_\rho(\omega, k_x)$  and  $S_\sigma(\omega, k_x)$  agree with the spectra seen in the Mott insulating phase of the 1D Hubbard model at half filling [111, 113, 114, 115]. These results confirm the validity of the 3-leg NLM as an approximation of the low-energy properties of the 3D wire-substrate model for  $U < U_c$  in the sense that in this parameter regime

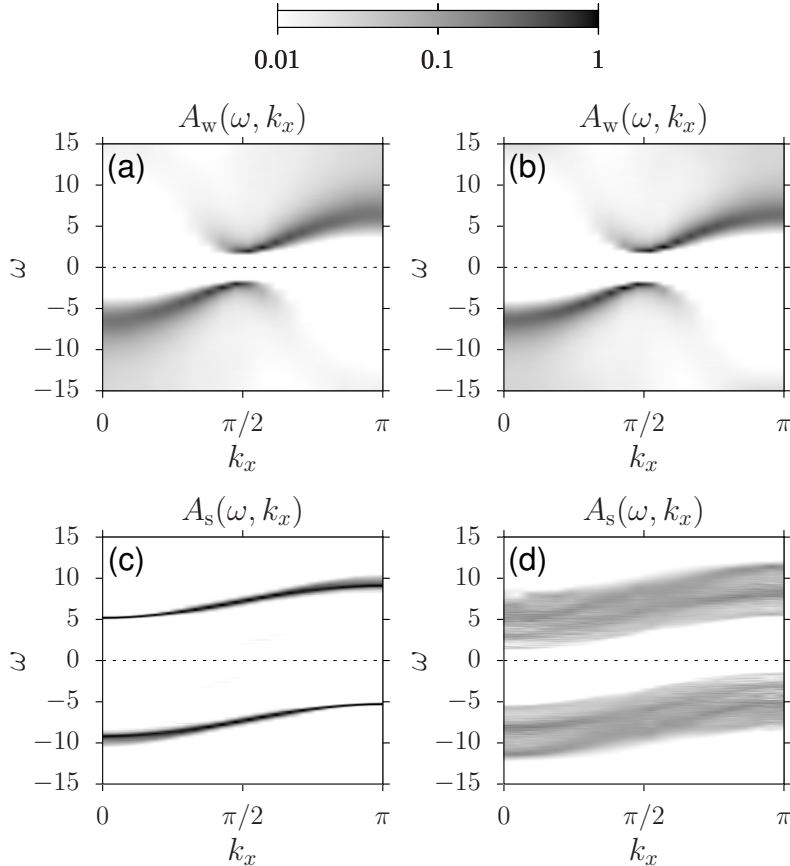


Figure 4.7: (a) and (b) show spectral functions on the wire  $A_w(\omega, k_x)$  while (c) and (d) are on the substrate  $A_s(\omega, k_x)$ . These calculations are done using CT-INT simulations for  $U = 12$ ,  $t_{ws} = 0.5$ ,  $\beta = 10$ , and  $L_x = 42$ . The chemical potential is adjusted to  $\mu = 0$ , corresponding to half-filling. Panels (a) and (c) show results for the three-leg NLM, panels (b) and (d) for the 3D wire-substrate model ( $L_y = 42$ ,  $L_z = 10$ ). Calculations and figure by Martin Hohenadler. The figure is published in Ref. [50].

the localization of the low-energy excitations in the wire subsystem is not an artifact but an actual feature inherited by the NLM from the original 3D wire-substrate model. The critical coupling for the 3D wire-substrate model at  $t_{ws} = 0.5$  is  $U_c \approx 9$  as estimated from DMRG calculations. This estimation is confirmed by the CT-INT calculations. Fig. 4.7(d) shows the SPSF of the substrate in the case  $U > U_c \approx 9$  while Fig. 4.7(c) displays the case  $U < U_c \approx 20$  due to the band gap enlargement in the 3-leg NLM. Nevertheless, the SPSF of the wire in Figs. 4.7(a) and (b) are similar for both systems and exhibit a gap  $\Delta_w \approx 4$  which is similar to the corresponding 1D Hubbard model at half filling and larger than the substrate band gap  $\Delta_s \approx 2$  in the 3D wire-substrate model. Thus, the low energy single-particle excitations of the 3D wire-substrate model are assigned to the conduction or valence band and delocalize in the substrate. This confirms the qualitative validity of the DMRG interpretation of the NLM for  $U > U_c \approx 20$  in the 3-leg NLM. By looking to the spin structure factor in Figs. 4.8(c) and (d) one can see clear gapless spin excitations localized in the wire despite the single-particle excitations

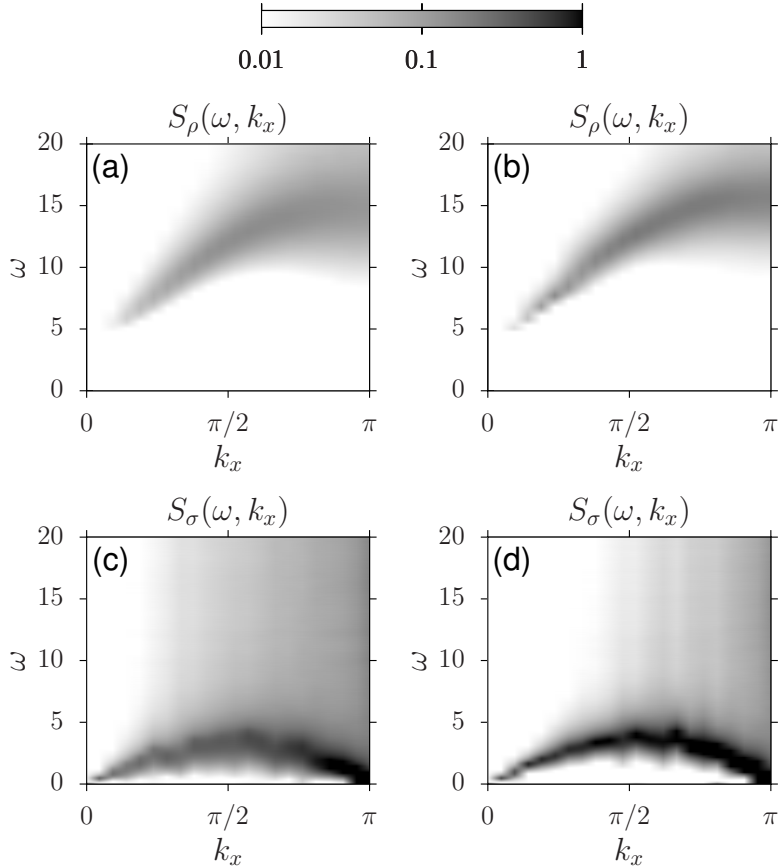


Figure 4.8: (a) and (b) show the dynamic charge structure factor  $S_\rho(\omega, k_x)$  while (c) and (d) show the dynamic spin structure factor  $S_\sigma(\omega, k_x)$ . All cases are calculated using CT-INT simulations on the wire for the same parameters as in Fig. 4.7. Panels (a) and (c) show results for the three-leg NLM, panels (b) and (d) for the 3D wire-substrate model. Calculations and figure by Martin Hohenadler. The figure is published in Ref. [50].

of the 3D wire-substrate model delocalize in the substrate. The charge structure factor in Figs. 4.8(a) and (b) do not reveal any spectral weight for  $\omega \lesssim 4$  meaning that charge excitations of the 3D wire-substrate model are high energy excitations but still localize in the wire. This, again, confirms the qualitative validity of the DMRG interpretations above the critical coupling.

The CT-INT method confirms that the transition from Mott insulator for  $U < U_c$  to a band insulator for  $U > U_c$  is not an artificial property of the NLM but an inherited property from the 3D wire-substrate model. This transition can be explained in the weak hybridization  $t_{ws}$ . At half filling a Mott gap is opened in the wire due to the umklapp scattering and electron-electron interactions (see chapter 1). It is situated in the middle of the substrate band gap and enlarged by increasing the coupling  $U$  until it reaches a value equal to the substrate band gap of  $U = U_c$ . By further increasing  $U$ , the Mott gap becomes even larger than the substrate band gap, which changes the nature of the elementary excitations from holon and spinon excitations in the 1D Mott insulator to electrons and holes in the band insulating substrate. This interpretation is confirmed by



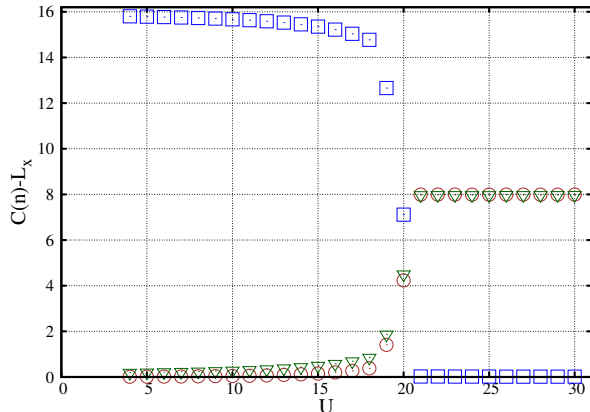


Figure 4.9: Difference between the total charge away from half filling  $C(n)$  and at half filling  $C(n) = L_x$  in the wire leg (squares) as well as in the first (circles) and second (triangles) substrate legs as a function of the Hubbard interaction  $U$ . The data were calculated with DMRG for a three-leg NLM with length  $L_x = 128$  and doped away from half filling with 16 particles. This figure is adapted from Ref. [50].

the agreement between the gap of the 1D Hubbard model and the Mott gap in the NLM for weak hybridization  $t_{ws}$ . It is also confirmed by the agreement between the saturation gap in the correlated NLM and the band gap in the corresponding noninteracting NLM. This description is valid even for large hybridization at least up to  $t_{ws} = 4$ . The charge and spin structure factors also support the interpretations of charge and spin density variations seen by DMRG for charge, spin and single-particle excitations. They also indicate that "local" experimental measurements could reveal properties of the embedded spin chain for  $U > U_c$ .

## 4.2 NLM for metallic Hubbard wire

The doped 1D Hubbard model represents a Luttinger liquid with gapless low energy charge and spin excitations. Therefore, doped wire which is completely decoupled from the substrate ( $t_{ws} = 0$ ) is a doped 1D Hubbard model making and is a Luttinger liquid. The Luttinger liquid properties are expected to persist for  $t_{ws} \neq 0$  and, hence, to be relevant to experimental realizations of atomic quantum wires discussed in Sec.1.2. Therefore,  $L_x/8$  electrons are added to the correlated NLM as well as to the 3D wire-substrate model. This corresponds to  $y_w = 12.5\%$  doping similar to the cases discussed in Secs. 3.3.3 and 3.3.2. Hole doping, i.e. electron removing, is equivalent to adding electrons due to the electron-hole symmetry of the model. To achieve  $y_w \approx 12.5\%$  doping in QMC calculations, different chemical potentials are used for the 3D wire-substrate model and the NLM due to the difference in the substrate band gap.

By analyzing the variation of charge density in the doped correlated NLM with respect to half filling one can distinguish two different trends for weak wire-substrate hybridization  $t_{ws}$ . Fig. 4.9 displays the charge density variation as a function of the coupling  $U$ . Most added charges localize in the wire for Hubbard interactions  $U \lesssim U_c$  where  $U_c \approx 20$  in the half filling cases of Sec. 4.1. Then, the added charges go abruptly to the substrate

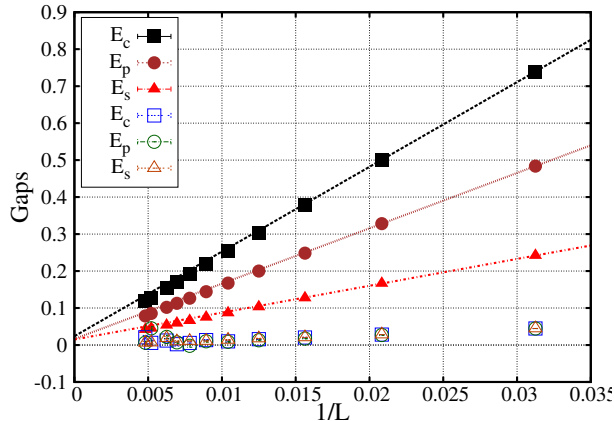


Figure 4.10: Charge ( $E_c$ ), spin ( $E_s$ ), and single-particle ( $E_p$ ) gaps calculated with DMRG for the three-leg NLM away from half filling with Hubbard interactions  $U = 16$  (filled symbols) and  $U = 24$  (open symbols). Slanting lines are linear fits. This figure is adapted from Ref. [50].

legs for  $U \gtrsim U_c$ . The additional electrons occupy the lowest excited states which correspond to the wire's upper Hubbard band for  $U \lesssim U_c$  but to the conduction band of the substrate legs for  $U \gtrsim U_c$ .

The finite-size scaling of charge, spin and single-particle gaps are different in the doped Mott and doped band insulating phases although they all vanish in the thermodynamic limit. Fig. 4.10 shows finite-size scaling of charge, single-particle and spin gaps for  $U = 16$  and  $U = 24$  at weak hybridization  $t_{ws} = 0.5$ . For  $U = 16$  (which corresponds to  $U < U_c$ ) the finite size gaps scale linearly with  $1/L_x$ . The corresponding velocities are given by Eq.(3.61). The largest value is found for charge velocity,  $v_c$ , and the smallest is found for the spin velocity,  $v_s$ . The single-particle velocity,  $v_p$ , gives the average of both charge and spin velocities. For  $U = 24$  (which corresponds to  $U > U_c$ ), charge, spin and single-particle gaps are equal within the numerical errors but they are much smaller than for  $U \lesssim U_c$  and they yield smaller velocities as well. The relatively large DMRG errors make it hard to determine the scaling with  $1/L_x$ . The excitation velocities have been investigated systematically for  $U \lesssim U_c$  (see Fig. 4.11). For very weak hybridizations  $t_{ws}$ , these velocities approach the values of those found in the similarly doped 1D Hubbard model. This result is found to be the same for larger ladder widths up to  $N_{leg} = 7$  legs. The spin velocities reduce significantly with increasing Hubbard interaction  $U$  while charge velocities are less affected. This trend is also seen for strong hybridization  $t_{ws}$ . In general, increasing the hybridization  $t_{ws}$  reduces the excitation velocities as seen in Fig. 4.11. The difference between charge and spin velocities is a typical feature of Luttinger liquids. This feature persists for strong hybridization  $t_{ws} > 0.5$  but with a different dependence on  $U$  than in the 1D Hubbard model.

The variations of charge and spin density distributions between excited and ground states of doped 3-leg correlated NLM are shown in Fig. 4.12. These distributions display the locations of the lowest charge and spin excitations away from half filling. For weak to moderate wire-substrate hybridizations, the distributions of charge and spin excitations are similar to the case at half filling, most charges localize in the wire leg for  $U \lesssim U_c$ . Increasing the hybridization  $t_{ws}$  in the region of  $U \lesssim U_c$  shows charge and spin

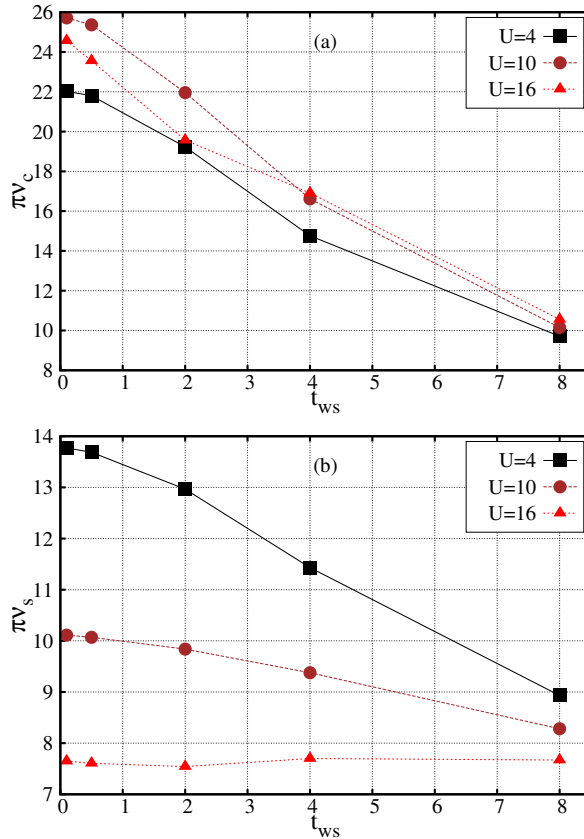


Figure 4.11: (a) Charge and (b) spin velocities calculated from the finite-size scaling of DMRG gaps in the three-leg NLM away from half filling as a function of the wire-substrate hybridization strength  $t_{ws}$  for three values of the Hubbard interaction  $U$ . These figures are adapted from Ref. [50].

distributions in both wire and substrate legs but with complex dependence on  $U$ . For  $U \gtrsim U_c$  all low-energy excitations, including spin excitations, delocalize almost entirely on the substrate legs and it seems that this behavior applied also for larger ladder widths, at least up to 7 legs. The distribution of the low-energy excitations in the substrate for  $U \gtrsim U_c$  in addition to the similarity between the excitation velocities imply that the overall system behave like a Fermi liquid. This interpretation is accompanied with the realization that the wire is still present as a chain of embedded spin impurities, for  $U > U_c$ , similarly to the cases at half filling.

This is confirmed by measuring the charge and spin correlation functions in the wire for  $U \lesssim U_c$  and  $U \gtrsim U_c$ . Fig. 4.13 illustrates this behavior by showing the measurements of the charge correlation functions for the wire which are defined in Eqs.(4.3) and (4.4). Fig. 4.13(a) shows charge density correlations in the wire for  $t_{ws} = 0.5$  and  $U = 24$  where  $U_c \approx 20$ . The charge density correlations exhibit an exponential decay for short distance  $x$  which agree quantitatively with the correlations for the 1D Hubbard chain at half filling. For long distance,  $F_c(x)$  saturates due to DMRG errors and the interferences with the power-law correlations in the substrate legs. This exponential decay in the wire is due to the average occupancy by one electron per site in the wire for  $U \gtrsim U_c \approx 20$ . For  $t_{ws} = 2.0$  and  $U = 24$  the critical Hubbard interaction is  $U_c \approx 32$ . Therefore,

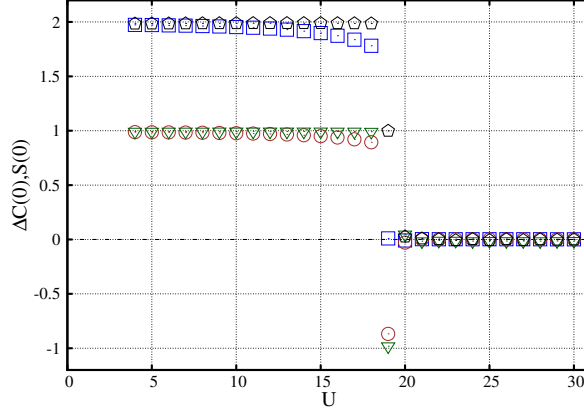


Figure 4.12: Variations of the charge  $\Delta C(0)$  and spin  $\Delta S(0) = S(0)$  on the wire leg calculated with DMRG for the lowest charge (squares), spin (pentagons), and single-particle (circles and triangles, respectively) excitations of the three-leg NLM away from half filling as a function of the Hubbard coupling  $U$ . This figure is adapted from Ref. [50].

the charge density correlations exhibit a power-law decay as expected for correlated 1D gapless electrons. The deviation of the power-law decay in the wire for  $t_{\text{ws}} = 2.0$  from the power-law decay in the 1D Hubbard chain doped with 12.5% electrons is due the large wire-substrate hybridization. On the other hand, Fig. 4.13(b) shows the spin correlations for the same systems. It is clear that the spin correlations have a power-law decay for all cases. This figure also shows a quantitative agreement between the case of weak wire-substrate hybridization ( $t_{\text{ws}} = 0.5$  and  $U = 24$ ) and the 1D Hubbard model at half filling. The wire charge and spin correlations of the 3-leg correlated NLM for  $U > U_c$  behave similarly to the 1D Hubbard model at half filling meaning that the wire still exhibits a chain of correlated impurities embedded in the substrate. In consistence with the half filling case, the doped correlated NLM shows a transition from a quasi-1D gapless phase (Luttinger liquid) at  $U \lesssim U_c$  to a Fermi liquid at  $U \gtrsim U_c$ .

The spectral properties are calculated using the CT-INT method and they confirm the distinct phases of doped NLM. The SPSF is shown in Fig. 4.14 for the doped 3-leg NLM and the doped 3D wire-substrate model with model parameters similar to those used to obtain Fig. 4.5 (i.e for  $U > U_c$ ). The SPSFs measured on the wire are nearly analogous in the 3-leg NLM [Fig. 4.14(a)] and the 3D wire-substrate model [Fig. 4.14(b)]. Both of them demonstrate gapless single-particle excitations. On the other side, a clear gap is depicted in Fig. 4.14(c) for the substrate SPSF of the 3-leg NLM. The Fermi energy ( $\omega = \mu$ ) of the 3D wire-substrate model is shifted quite close to the bottom of the SPSF conduction band but it is still located within the substrate band gap as shown in Fig. 4.14(d). The little spectral weight just touching the bottom of the conduction band is the result of the finite temperature  $\beta^{-1}$  in the QMC calculations. These results confirm the DMRG findings of gapless low-energy excitations that localize in the wire. They also confirm that these properties are inherited by the 3-leg NLM as an approximation to the 3D wire-substrate model.

The dynamic charge and spin structure factors measured on the wire are similar in both the 3-leg NLM and the 3D wire substrate model. This is seen clearly in Fig. 4.15 with gapless charge and spin excitation. Both dynamic structure factors resemble those

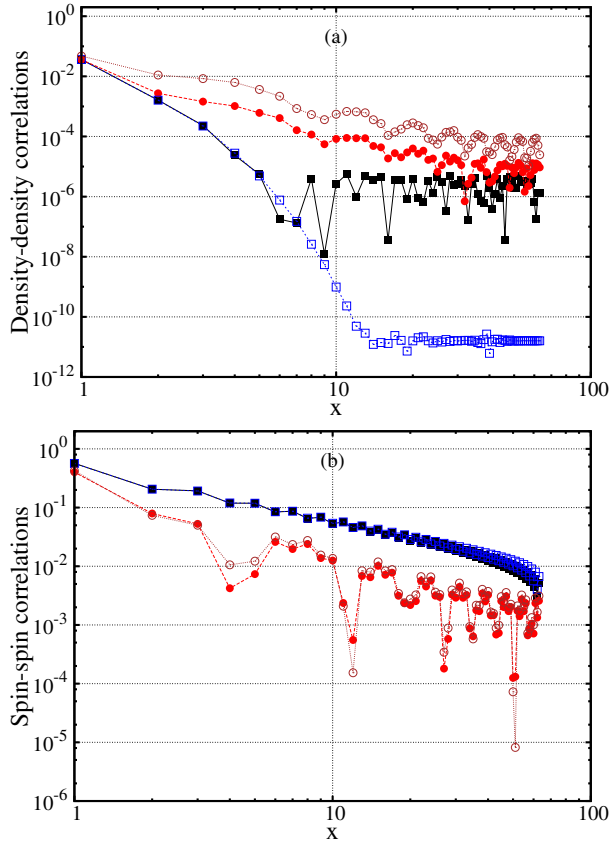


Figure 4.13: (a) Charge and (b) spin correlation functions on the wire leg calculated with DMRG for a three-leg NLM away from half filling with  $t_{\text{ws}} = 0.5$  (filled squares), and  $t_{\text{ws}} = 2$  (filled circles) as well as for the 1D Hubbard model at half filling (open squares) and at 12.5% doping away from half filling (open circles). In all four cases  $U = 24$ . These figures are adapted from Ref. [50].

of the Luttinger liquid phase realized in the doped 1D Hubbard model [116].

The large critical value of the coupling  $U_c \approx 20$  does not allow to investigate the crossover between the two gapless phases in the 3-leg NLM. However, the critical value  $U_c \approx 9$  of the 3D wire-substrate model allows us to perform the investigations using the CT-INT method. Fig. 4.16 displays the SPSF of the doped 3-leg NLM and the 3D wire-substrate model for  $U = 12$  and other parameters similar to Fig. 4.7 but with different chemical potential. The chemical potential corresponds to a finite wire doping  $y_w = 12.5\%$  which shifts the Fermi energy to just above the bottom edge of the conduction band. The determination of the chemical potential in this case turned to be a fine-tune problem. The value of the  $U$  coupling is larger than the critical value of the 3D wire-substrate model but smaller than the critical value of the 3-leg NLM. Thus, the wire SPSF shown in Fig. 4.16(a) resembles qualitatively the SPSF with gapless excitations seen in Fig. 4.14(a). In contrast, the SPSF of Fig. 4.16(b) looks alike those of the 1D Hubbard model with gapped excitations at half filling. The Fermi energy is located in the wire Mott gap close to the bottom of the conduction band. However, by looking to Fig. 4.16(d) one sees that, indeed, the Fermi energy lies just above the bottom edge of the conduction band which gives a doped band insulator with gapless single-particle

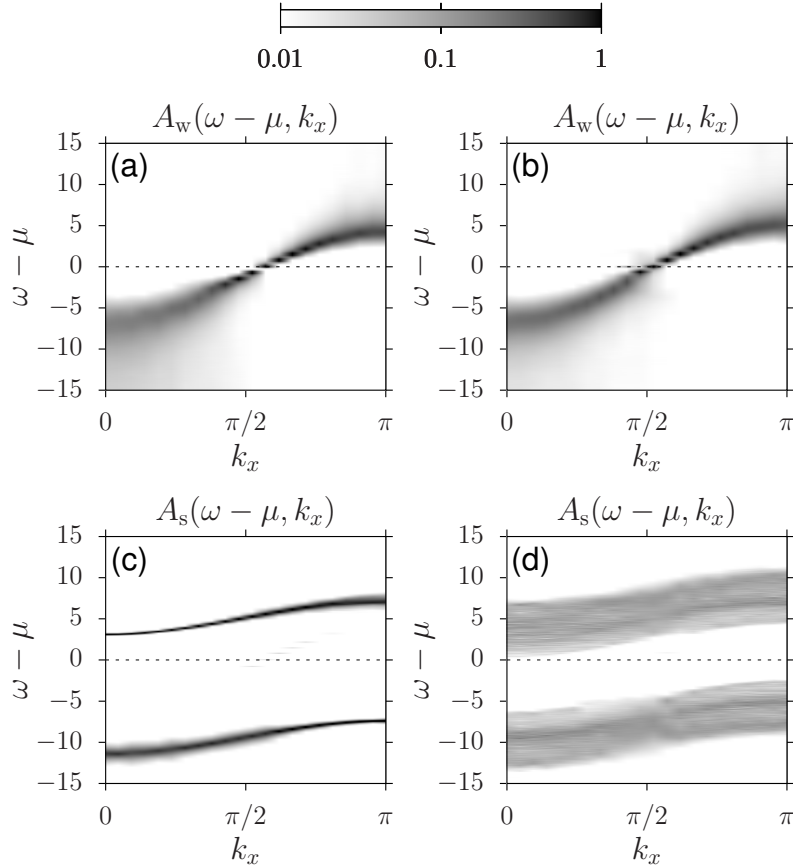


Figure 4.14: (a) and (b) show spectral functions on the wire  $A_w(\omega, k_x)$  while (c) and (d) are on the substrate  $A_s(\omega, k_x)$ . These calculations are done using CT-INT simulations for  $U = 8$ ,  $t_{ws} = 0.5$ ,  $\beta = 15$ , and  $L_x = 42$ . Panels (a) and (c) show results for the three-leg NLM, panels (b) and (d) for the 3D wire-substrate model ( $L_y = 42$ ,  $L_z = 10$ ). The chemical potential is tuned to  $\mu = 2.1375$  for the NLM and to  $\mu = 0.99$  for the 3D model, corresponding to a doping of  $y_w \approx 12.5\%$ . Calculations and figure by Martin Hohenadler. The figure is published in Ref. [50].

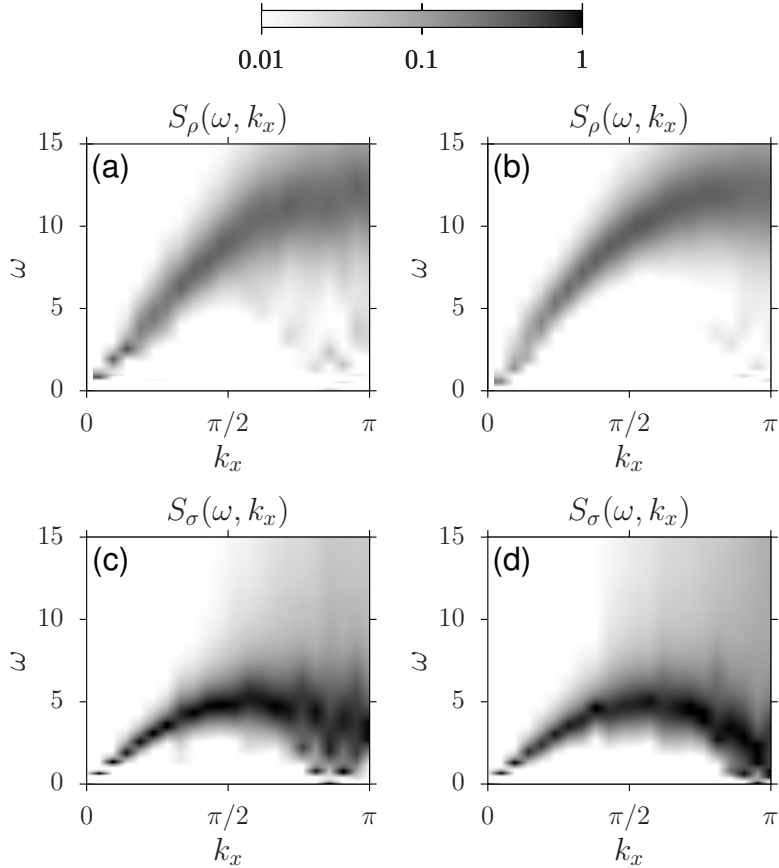


Figure 4.15: (a) and (b) show the dynamic charge structure factor  $S_\rho(\omega, k_x)$  while (c) and (d) show the dynamic spin structure factor  $S_\sigma(\omega, k_x)$ . All cases are calculated using CT-INT simulations on the wire for the same parameters as in Fig. 4.14. Panels (a) and (c) show results for the three-leg NLM, panels (b) and (d) for the 3D wire-substrate model. Calculations and figure by Martin Hohenadler. The figure is published in Ref. [50].

excitations delocalized in the 3D substrate. Despite the shift of the Fermi energy towards the conduction band, it still lies within the substrate band gap of the 3-leg NLM as seen in Fig. 4.16(c). These findings are confirmed by the dynamic charge and spin structure factors in Fig. 4.17. The gapped charge excitations but gapless spin excitations on the wire are confirmed in Figs. 4.17 (b) and (d), respectively, for the 3D wire-substrate model. The charge gap in this case is equal to the Mott gap shown for the half-filled 3D wire-substrate model in Fig. 4.8(b). Both structure factors reveal gapless charge and spin excitations for the 3-leg NLM in Figs. 4.17(a) and (c), respectively. Therefore, the wire exhibits a Mott insulating character in the 3D wire-substrate model but a Luttinger liquid behavior in the 3-leg NLM. This discrepancy is explained by the dependence of the substrate band gap  $\Delta_s(N_{\text{leg}})$  on the number of legs in the 3-leg NLM, which causes the NLM approximation to fail in such cases. A possible treatment of this problem is to change the rung hopping  $t_n^{\text{rung}}$  in the Hamiltonian (3.51) to rescale the substrate band gap  $\Delta_s(N_{\text{leg}})$ .

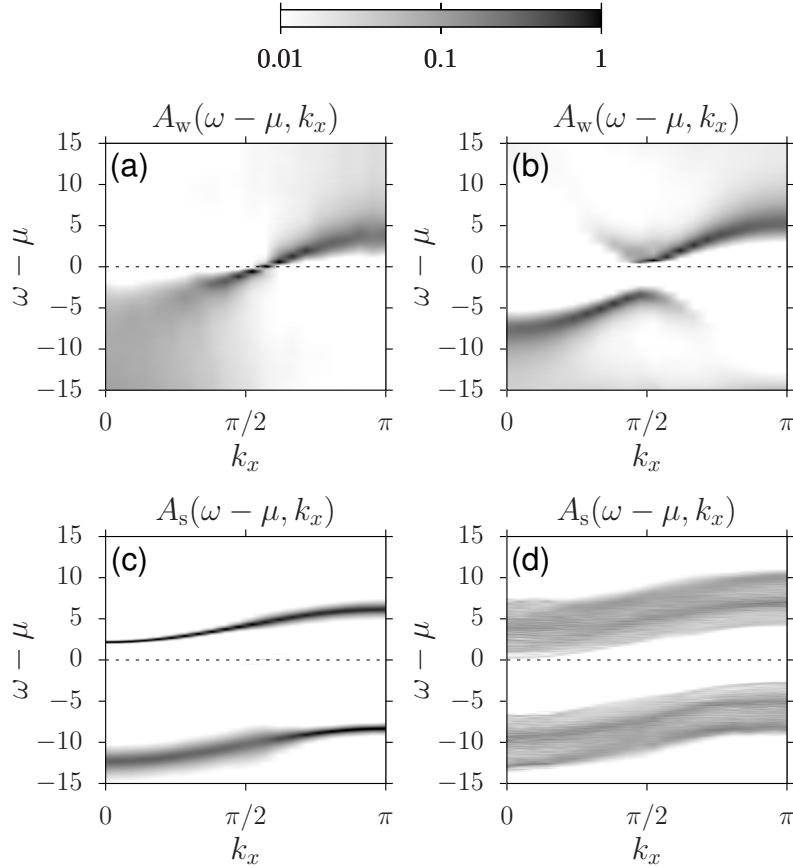


Figure 4.16: (a) and (b) show spectral functions on the wire  $A_w(\omega, k_x)$  while (c) and (d) are on the substrate  $A_s(\omega, k_x)$ . These calculations are done using CT-INT simulations for  $U = 12$ ,  $\beta = 10$ , and  $L_x = 42$ . Panels (a) and (c) show results for the three-leg NLM, panels (b) and (d) for the 3D wire-substrate model ( $L_y = 42$ ,  $L_z = 10$ ). The chemical potential is tuned to  $\mu = 3.08$  for the NLM and to  $\mu = 1.205$  for the 3D model, corresponding to a doping of  $y_w \approx 12.5\%$ . Calculations and figure by Martin Hohenadler. The figure is published in Ref. [50].



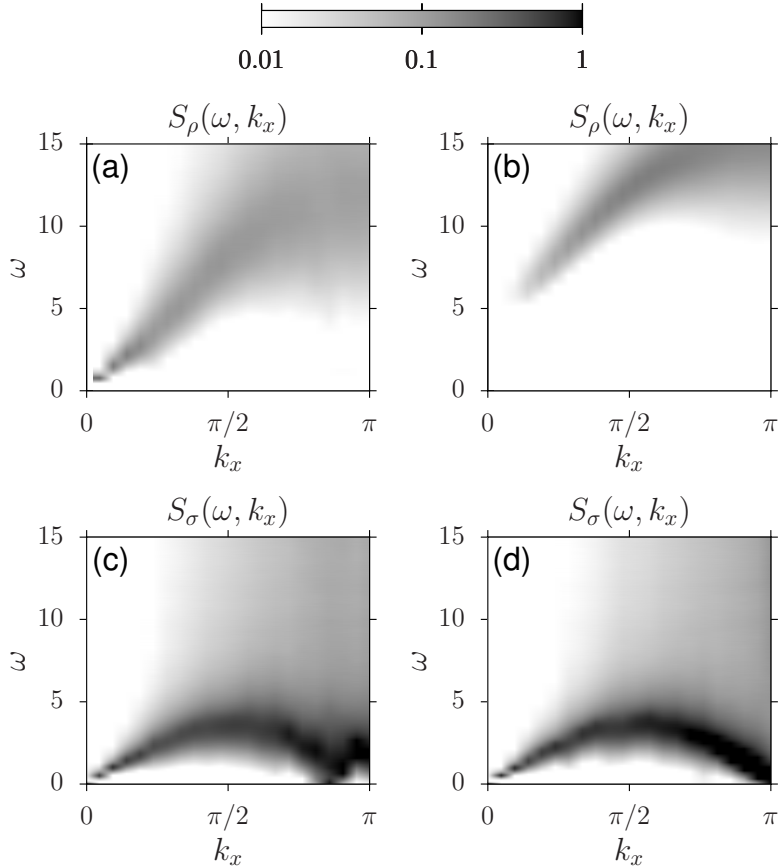


Figure 4.17: (a) and (b) show the dynamic charge structure factor  $S_\rho(\omega, k_x)$  while (c) and (d) show the dynamic spin structure factor  $S_\sigma(\omega, k_x)$ . All cases are calculated using CT-INT simulations on the wire for the same parameters as in Fig. 4.16. Panels (a) and (c) show results for the three-leg NLM, panels (b) and (d) for the 3D wire-substrate model. Calculations and figure by Martin Hohenadler. The figure is published in Ref. [50].

### 4.3 Discussion

As discussed in Sec.1.1, isolated correlated 1D conductors are classified as Luttinger liquids and coupled Luttinger liquids retain this feature in certain conditions. Thus, there is no surprise to find a Luttinger liquid phase in the correlated NLM. The surprising finding is the uncorrelated gapless phase for strong coupling. The confinement of low-energy excitations on the wire gives rise to the distinctive Luttinger liquid features such as the dynamic spin charge separations seen for  $U < U_c$ . The other case of  $U > U_c$  is distinguished by the disappearance of these Luttinger liquid features, i.e. due to the equal finite-size scaling of charge and spin gaps as well as the delocalization of excitations in the substrate legs. By increasing the hybridization  $t_{ws}$  the difference between charge and spin velocities reduces and it is unsettled if the weakly-coupled Luttinger liquid persists or it becomes a quasi 1D Fermi gas in the  $t_{ws} \rightarrow \infty$  limit. However, increasing the wire-substrate hybridization seems to preserve the one-dimensionality of the system.

The 3D wire-substrate model and the corresponding NLM can be extended to electron-

phonon Hamiltonian or generalized Hubbard model. They provide a promising platform to investigate experimental wire-substrate systems using DMRG, QMC and other methods for correlated electrons. The band structure and the wire-substrate hybridization could be inferred from first principle calculations but fixing the electron-electron interactions remain an open problem.

# Chapter 5

## Summary and outlook

Two approaches to model systems of atomic nanowires on semiconducting substrate are presented in this thesis. In both approaches, the 1D Hubbard model is used to describe the correlated wire. In the first approach, the substrate is reduced to be represented by a 1D tight-binding chain and the wire-substrate hybridization is described by a single-particle hopping between sites in the wire and their adjacent sites in the tight-binding chain. The same hybridization is used in the second approach but the substrate is described using a 3D tight-binding model with two orbital per site to produce an insulating substrate. The first model demonstrates an asymmetric ladder system and it reveals rich physics at half filling despite its simplicity. In part of its parameter regime, this asymmetric ladder displays properties similar to those in the symmetric two-leg Hubbard ladder at half filling and in other parameter regimes it exhibits properties of the Kondo-Heisenberg model at half filling. An interesting phase which is also uncovered in this asymmetric ladder is classified as a Luttinger liquid phase. This phase is characterized by dynamical spin-charge separation but with single-particle excitation velocity equal to the charge excitation velocity. This is attributed to an effective decoupling between the two legs in this phase, i.e. the Hubbard leg behaves as an independent 1D Hubbard chain and the other leg as an independent tight-binding chain. The analysis of excitation densities as well as the correlation functions are in consistence with such effective decoupling. An other phase, the Kondo-Mott phase is characterized by a commensurate wave number of its lowest excitation equal to  $\pi/2$ . This phase reveals small spin gaps which are reflected in spin-spin correlations with correlation lengths larger than the studied system sizes and hence indistinguishable from power-law decays. The density-density correlations show much more obvious exponential decay. The spin-gapped Mott insulating phase is featured by incommensurate wave number for its lowest excitations. It is also characterized by finite pair-binding energy. However, no enhancement of pairing correlations is found in comparison to the noninteracting system  $U = 0$ . The fourth phase is the correlated band insulating phase with lowest excitations commensurate wave number at 0 or  $\pi$ . The charge and spin gaps scale linearly with  $t_{\perp}$  in this phase. Nevertheless, this model is dominated by physics of correlated ladder systems except for the Luttinger liquid phase and hence it is not appropriate as a model for wire-substrate systems.

In the future, it would be interesting to perform field-theoretical study on the asymmetric 2-leg ladder to confirm the Luttinger liquid phase and the properties in the other phases, especially the asymptotic behavior of different correlation functions. Further-

more, the DMRG and the related MPS methods could be used to study the precise points of phase transition by measuring entanglement entropy or entanglement spectrum. An other interesting point is to allow additional parameters in the asymmetric model by varying independently the intra-leg hopping in the Hubbard leg. This could provide an appropriate way to compare with the Kondo-Heisenberg model.

The second approach considers a 3D tight-binding model for the substrate while keeping the models for the wire and the wire-substrate hybridization similar to the first approach. However, the 3D nature of the substrate prevents state-of-the-art methods of quasi-on-dimensional systems from treating this modeling approach. Therefore, an exact procedure to map the 3D wire-substrate model onto 2D ladder model has been introduced. This procedure depends on producing a set of independent single-impurity problems on 2D hosts by transforming the 3D wire-substrate model to the momentum space. Each 2D problem is mapped onto a 1D chain using the Lanczos algorithm and then transformed back to real space in the  $x$ -direction. This transformations are performed for a noninteracting 3D wire-substrate model. Then, the Coulomb electron-electron interaction is restored in the wire. An other way to perform the mapping is possible by starting from a decoupled wire-substrate model. Then the described steps can be done separately for each band in the substrate. The wire could be then coupled only to the adjacent substrate sites. The next step is to reduce the 2D ladder model to just a limited number of legs which should serve as a good approximation. Indeed, the performed systematic investigations show that it is a good approximation for models with insulating substrate as long as the low-energy excitations localize on the wire. If the lowest excitations delocalize on the substrate this indicates, for wires with Hubbard like interaction, a crossover from a Luttinger liquid to a doped band insulator for systems doped away from half filling. Systems at half filling show a crossover from 1D Mott insulator to band insulator. For metallic substrates the approximation by just few-leg ladders is not a good approximation. It is worth to mention that the number of legs must be odd numbers to represent the insulating substrate with its conduction and valence bands as well as the wire band. The mapping idea and the approximation by limited number of legs provide good platform to investigate electron correlation effects on systems of atomic nanowires on semiconducting substrates similar to those discussed on Sec.1.2.

For future studies it is interesting to perform more systematic investigations on the convergence of the NLM with the number of legs. This is much more convenient by choosing the wire as a spinless fermion chain. This offers the possibility to investigate the influence of the substrate on the quantum phase transition between a Luttinger liquid and a charge-density-wave insulator that appears in the one-dimensional spinless fermion model. Moreover, it allows the calculation of the structure factor for the NLM and, consequently, the calculations of Luttinger liquid parameters.

The ladder mapping and the NLM are capable for generalizations that can capture other physical properties, such as spin-orbit coupling, electron-phonon coupling, multi-wire system on a substrate, etc. The multi-wire system on a substrate can be constructed using the block-Lanczos method introduced in Ref. [90]. This will allow to investigate the influence of wire-wire coupling on the one-dimensional properties in the presence of the substrate.

An important future step is to use the NLM for real wire-substrate system. The parameters and the range of hopping integrals for the substrate as well as the wire-substrate

hybridization can be selected using experimental and DFT results. The remaining open issue then is to chose appropriate value and range for the electron-electron Coulomb interaction.

# Bibliography

- [1] D. Baeriswyl and L. Degiorgi (Eds.), *Strong Interactions in Low Dimensions* (Kluwer Academic Publishers, Dordrecht, 2004).
- [2] S. Kagoshima, H. Nagasawa, and T. Sambongi, *One-Dimensional Conductors* (Springer, Berlin, 1982).
- [3] G. Grüner, *Density Waves in Solids* (Perseus Publishing, Cambridge, 2000).
- [4] T. Giamarchi, *Quantum Physics in One Dimension* (Oxford University Press, Oxford, 2007).
- [5] M. Dressel, ISRN Condens. Matter Phys. 2012, 732973.
- [6] H. Kiess (ed.), *Conjugated Conducting Polymers* (Springer, Berlin, 1992).
- [7] F. D. M. Haldane, J. Phys. C: Solid State Phys. **14**, 2585 (1981).
- [8] J. Sólyom, *Fundamental of the Physics of Solids*, **V. 3** (Springer-Verlag, Berlin Heidelberg, 2010).
- [9] J. Voit, J. Phys. Condens. Matter **5**, 8305 (1993).
- [10] F. Gebhard, *The Mott Metal-Insulator Transition* (Springer, Berlin, 1997).
- [11] F.H.L. Essler, H. Frahm, F. Göhmann, A. Klümper, and V. Korepin, *The One-Dimensional Hubbard Model* (Cambridge University Press, Cambridge, 2005).
- [12] H.-J. Mikeska and A.K. Kolezhuk, One-Dimensional Magnetism, Lect. Notes Phys. **645**, 1–83 (2004).
- [13] F. D. M. Haldane, Phys. Rev. Lett. **50**, 1153 (1983).
- [14] R. M. Noack, S. R. White, and D. J. Scalapino, Phys. Rev. Lett. **73**, 882 (1994).
- [15] E. Jeckelmann, D. J. Scalapino, and S. R. White, Phys. Rev. B **58**, 9492 (1998).
- [16] J. Schäfer, C. Blumenstein, S. Meyer, M. Wisnieski and R. Claessen, Phys. Rev. Lett. **101**, 236802 (2008).
- [17] D. Jerome, Chem. Rev. **104** (11), 5565 (2004).
- [18] T. Giamarchi, Int. J. Mod. Phys. B 26 22, 1244004 (2012).

- [19] R. Claessen, M. Sing, U. Schwingenschlögl, P. Blaha, M. Dressel, and C. S. Jacobsen Phys. Rev. Lett. **88**, 096402 (2002).
- [20] L. Markhof and V. Meden, Phys. Rev. B **93**, 085108 (2016).
- [21] O. M. Auslaender, A. Yacoby, R. de Picciotto, K. W. Baldwin, L. N. Pfeiffer, K. W. West, Science **295** 5556, 825 (2002).
- [22] Y. Tserkovnyak, B. Halperin, O. M. Auslaender, and A. Yacoby, Phys. Rev. Lett. **89**, 136805 (2002).
- [23] O. Gurlu, O. A. O Adam, H. J. W. Zandvliet and B. Poelsema, Appl. Phys. Lett. **83**, 4610 (2003).
- [24] N. Oncel, A. van Houselt, J. Huijben, A. Hallbäck, O. Gurlu, H. j. W. Zandvliet and B. Poelsema, Phys. Rev. Lett. **95**, 116801 (2005).
- [25] A. A. Stekolnikov, F. Bechstedt, M. Wisniewski, J. Schäfer and R. Claessen, Phys. Rev. Lett. **100**, 196101 (2008).
- [26] D. E. P. Vanpoucke and G. Brocks, Phys. Rev B **81**, 085410 (2010).
- [27] A. van Houselt, T. Gnielka, J. M. J. An der Brugh, N. Oncel, D. Kockmann, R. Heid, K-P Bohnen, B. Poelsema and H. J. W. Zandvliet, Surf. Sci. **602**, 1731 (2003).
- [28] I. Mochizuki, Y. Fukaya, A. Kawasuso, K. Yaji, A. Harasawa, I. Matsuda, K. Wada, and T. Hyodo, Phys. Rev. B **85**, 245438 (2012).
- [29] K. Yaji, I. Mochizuki, S. Kim, Y. Takeichi, A. Harasawa, Y. Ohtsubo, P. Le Fèvre, F. Bertran, A. Taleb-Ibrahimi, A. Kakizaki, and F. Komori, Phys. Rev. B **87**, 241413(R) (2013).
- [30] K.Yaji, S. Kim, I. Mochizuki, Y. Takeichi, Y. Ohtsubo, P. Le Fèvre, F. Bertran, A. Taleb-Ibrahimi, S. Shin and F. Komori, Journal of Physics: Condensed Matter **28**, 284001 (2016).
- [31] J. Wang, M. Li and E. I. Altman, Phys. Rev B **70**, 233312 (2004).
- [32] A. van Houselt, D. Kockmann, T. F. Mocking, B. Poelsema, and H. J. W. Zandvliet, Phys. Rev. Lett. **103**, 209701 (2009).
- [33] A. van Houselt, M. Fischer, B. Poelsema, and H. J. W. Zandvliet, Phys. Rev. B **78**, 233410 (2008).
- [34] K. Nakatsuji, R. Niikura, Y. Shibata, M. Yamada, T. Iimori, and F. Komori, Phys. Rev. B **80**, 081406(R) (2009).
- [35] S. Meyer, J. Schäfer, C. Blumenstein, P. Höpfner, A. Bostwick, J. L. McChesney, E. Rotenberg, and R. Claessen Phys. Rev. B **83**, 121411(R) (2011).
- [36] S. Sauer, F. Fuchs, F. Bechstedt, C. Blumenstein, and J. Schäfer Phys. Rev. B **81**, 075412 (2010).

- [37] C. Blumenstein, J. Schäfer, S. Mietke, S. Meyer, A. Dollinger, M. Lochner, X. Y. Cui, L. Patthey, R. Matzdorf, and R. Claessen, *Nature Physics* **7**, 776 (2011).
- [38] K. Nakatsuji, Y. Motomura, R. Niikura, and F. Komori, *Phys. Rev. B* **84**, 115411 (2011).
- [39] Jewook Park, Kan Nakatsuji, Tae-Hwan Kim, Sun Kyu Song, Fumio Komori, and Han Woong Yeom *Phys. Rev. B* **90**, 165410 (2014).
- [40] N. de Jong, R. Heimbuch, S. Eliëns, S. Smit, E. Frantzeskakis, J.-S. Caux, H. J. W. Zandvliet, and M. S. Golden, *Phys. Rev. B* **93**, 235444 (2016).
- [41] K. Seino and F. Bechstedt, *Phys. Rev. B* **93**, 125406 (2016).
- [42] K. Seino, S. Sanna and W Gero Schmidt, *Surf. Sci.* **667**, 101 (2018).
- [43] L Dudy, J Aulbach, T Wagner, J Schäfer and R Claessen, *J. Phys.: Condens. Matter* **29**, 433001 (2017).
- [44] Yoshiyuki Ohtsubo, Jun-ichiro Kishi, Kenta Hagiwara, Patrick Le Fèvre, François Bertran, Amina Taleb-Ibrahimi, Hiroyuki Yamane, Shin-ichiro Ideta, Masaharu Matsumami, Kiyohisa Tanaka, and Shin-ichi Kimura *Phys. Rev. Lett.* **115**, 256404 (2015).
- [45] Yoshiyuki Ohtsubo, Jun-ichiro Kishi, Kenta Hagiwara, Patrick Le Fèvre, Francois Bertran, Amina Taleb-Ibrahimi, Shin-ichi Kimura, *J. Electron. Spectrosc. Relat. Phenom.*, **220**, pages 37-39 (2017).
- [46] U. Schollwöck, *Rev. Mod. Phys.* **77**, 259 (2005).
- [47] Anas Abdelwahab, Eric Jeckelmann, and Martin Hohenadler *Phys. Rev. B* **91**, 155119 (2015).
- [48] H. Yoshizomi, T. Tohyama, and T. Morinari, *Progress of Theoretical Physics*, 122 (4) 943 (2009).
- [49] Anas Abdelwahab, Eric Jeckelmann, and Martin Hohenadler *Phys. Rev. B* **96**, 035445 (2017).
- [50] Anas Abdelwahab, Eric Jeckelmann, and Martin Hohenadler *Phys. Rev. B* **96**, 035446 (2017).
- [51] S. R. White, *Phys. Rev. Lett.* **69**, 2863 (1992); *Phys. Rev. B* **48**, 10345 (1993).
- [52] U. Schollwöck, *Ann. Phys.* **326** 1, 96 (2011).
- [53] R. Orus, *Ann. Phys.* **349**, 117 (2014).
- [54] M. Springborg and Y. Dong, *Metallic Chains / Chains of Metals* (Elsevier, Amsterdam, 2007).
- [55] I. K. Dash and A. J. Fisher, *J. Phys.: Condens. Matter* **13**, 5035 (2001).



- [56] I. K. Dash and A. J. Fisher, e-print arXiv:cond-mat/0210611v1.
- [57] A. E. Sikkema, I. Affleck, and S. R. White, Phys. Rev. Lett. **79**, 929 (1997).
- [58] O. Zachar and A. M. Tsvelik, Phys. Rev. B **64**, 033103 (2001).
- [59] E. Berg, E. Fradkin, and S. A. Kivelson, Phys. Rev. Lett. **105**, 146403 (2010).
- [60] A. Dobry, A. Jaefari, and E. Fradkin, Phys. Rev. B **87**, 245102 (2013).
- [61] E. Eidelstein, S. Moukouri, and A. Schiller, Phys. Rev. B **84** 014413 (2011).
- [62] K. A. Al-Hassanieh, C. D. Batista, P. Sengupta, and A. E. Feiguin, Phys. Rev. B **80**, 115116 (2009).
- [63] Anas Abdelwahab and Eric Jeckelmann, arXiv:1707.08780 [cond-mat.str-el].
- [64] L. Balents and M. P. A. Fisher, Phys. Rev. B **53**, 12133 (1996).
- [65] D. Controzzi and A. M. Tsvelik, Phys. Rev. B **72**, 035110 (2005).
- [66] A. M. Tsvelik, Phys. Rev. B **83**, 104405 (2011).
- [67] N. J. Robinson, F. H. L. Essler, E. Jeckelmann, and A. M. Tsvelik, Phys. Rev. B **85**, 195103 (2012).
- [68] S. T. Carr, B. N. Narozhny, and A. A. Nersisyan, Annals of Physics **339**, 22 (2013).
- [69] J. R. Schrieffer and P. A. Wolff, Phys. Rev. **149**, 491 (1966).
- [70] C. Lacroix and M. Cyrot, Phys. Rev. B **20**, 1969 (1979).
- [71] H. Eskes, A. M. Oleś, M. B. J. Meinders, and W. Stephan, **50**, 17980 (1994).
- [72] E. Jeckelmann, in *Computational Many Particle Physics* (Lecture Notes in Physics **739**), edited by H. Fehske, R. Schneider, and A. Weiße (Springer-Verlag, Berlin, Heidelberg, 2008), p. 597.
- [73] Clare C. Yu and Steven R. White, Phys. Rev. Lett. **97**, 3866 (1993).
- [74] A. Jaefari and E. Fradkin, Phys. Rev. B **85**, 035104 (2012).
- [75] H. Benthien, F. Gebhard, and E. Jeckelmann, Phys. Rev. Lett. **92**, 256401 (2004).
- [76] E. Jeckelmann, Progress of Theoretical Physics Supplement **176**, 143 (2008).
- [77] E. Jeckelmann and H. Benthien, in *Computational Many Particle Physics* (Lecture Notes in Physics **739**), edited by H. Fehske, R. Schneider, and A. Weiße (Springer-Verlag, Berlin, Heidelberg, 2008), p. 621.
- [78] A. N. Rubtsov, V. V. Savkin, and A. I. Lichtenstein, Phys. Rev. B **72**, 035122 (2005).
- [79] E. Gull, A. J. Millis, A. I. Lichtenstein, A. N. Rubtsov, M. Troyer, and P. Werner, Rev. Mod. Phys. **83**, 349 (2011).

- [80] O. Golinelli, Th. Jolicœur, and E. S. Sørensen, *Eur. Phys. J. B* **11**, 199 (1999).
- [81] A. Lavarélo, G. Roux, and N. Lafflorencie, *Phys. Rev. B* **84** 144407 (2011).
- [82] I. T. Shyiko, I. P. McCulloch, J. V. Gumenjuk-Sichevska, and A. K. Kolezhuk, *Phys. Rev. B* **88**, 014403 (2013).
- [83] A. Osterloh, L. Amico, G. Falci, and R. Fazio, *Nature* **416**, 608 (2002).
- [84] L.-A. Wu, M. S. Sarandy, and D. A. Lidar, *Phys. Rev. Lett.* **93**, 250404 (2004).
- [85] Ö. Legeza and J. Sólyom, *Phys. Rev. Lett.* **96**, 116401 (2006).
- [86] Ö. Legeza, J. Sólyom, L. Tincani, and R. M. Noack, *Phys. Rev. Lett.* **99**, 087203 (2007).
- [87] C. Mund, Ö. Legeza, and R. M. Noack, *Phys. Rev.* **79**, 245130 (2009).
- [88] Hui Li and F. D. M. Haldane, *Phys. Rev. Lett.* **101**, 010504 (2008).
- [89] G. De Chiara, L. Lepori, M. Lewenstein, and A. Sanpera, *Phys. Rev. Lett.* **109**, 237208 (2012).
- [90] T. Shirakawa and S. Yunoki, *Phys. Rev. B* **90**, 195109 (2014).
- [91] A. Allerdt, C. A. Büsser, G. B. Martins, and A. E. Feiguin, *Phys. Rev. B* **91**, 085101 (2015).
- [92] N. Oncel, *J. Phys.: Condens. Matter* **20**, 393001 (2008).
- [93] P. C. Snijders and H. H. Weitering, *Rev. Mod. Phys.* **82**, 307 (2010).
- [94] L. Cano-Cortès, A. Dolfen, J. Merino, J. Behler, B. Delley, K. Reuter, and E. Koch, *Eur. Phys. J. B* **56**, 173 (2007).
- [95] G. D. Mahan, *Many-Particle Physics* (Kluwer Academic, New York, 2000).
- [96] K. G. Wilson, *Rev. Mod. Phys.* **47**, 773 (1975).
- [97] D. C. Mattis in J. Bernasconi and T. Schneider (eds.), *Physics in One Dimension* (Springer, Berlin, 1981).
- [98] G. Knizia and G. K.-L. Chan, *Phys. Rev. Lett.* **109**, 186404 (2012).
- [99] G. Ehlers, J. Sólyom, Ö. Legeza, and R. M. Noack, *Phys. Rev. B* **92**, 235116 (2015).
- [100] S. Moukouri, *Phys. Rev. B* **70**, 014403 (2004).
- [101] S. Moukouri and E. Eidelstein, *Phys. Rev. B* **82**, 165132 (2010).
- [102] T. Xiang, *Phys. Rev. B* **53**, R10445(R) (1996).
- [103] S. Nishimoto, E. Jeckelmann, F. Gebhard, and R. M. Noack, *Phys. Rev. B* **65**, 165114 (2002).

- [104] C. Zhang, E. Jeckelmann, and S. R. White, *Phys. Rev. Lett.* **80**, 2661 (1998).
- [105] R. J. Bursill, *Phys. Rev. B* **60**, 1643 (1999).
- [106] E. Jeckelmann and H. Fehske, *Riv. Nuovo Cimento* **30**, 259 (2007).
- [107] J. Sólyom, *Advances in Physics*, **28**, 201 (1979).
- [108] A. O. Gogolin, A. A. Nersesyan, A. M. Tsvelik, *Bosonization and Strongly Correlated Systems*, Cambridge University Press 1998.
- [109] A. M. Tsvelik, *Quantum Field Theory in Condensed Matter Physics*, Cambridge University Press 2003.
- [110] K. Schönhammer, *Luttinger liquids: the basic concepts*, Chap. 4 of Ref. [1].
- [111] H. Benthien and E. Jeckelmann, *Phys. Rev. B* **75**, 205128 (2007).
- [112] M. Aichhorn, H. G. Evertz, W. von der Linden, and M. Potthoff, *Phys. Rev. B* **70**, 235107 (2004).
- [113] M. Raczkowski, F. F. Assaad, and L. Pollet, *Phys. Rev. B* **91**, 045137 (2015).
- [114] A. Nocera, N. D. Patel, J. Fernandez-Baca, E. Dagotto, and G. Alvarez, *Phys. Rev. B* **94**, 205145 (2016).
- [115] R. G. Pereira, K. Penc, S. R. White, P. D. Sacramento, and J. M. P. Carmelo, *Phys. Rev. B* **85**, 165132 (2012).
- [116] A. Abendschein and F. F. Assaad, *Phys. Rev. B* **73**, 165119 (2006).

## Acknowledgment

It was a great opportunity to be a student of Prof. Eric Jeckelmann and to work with him. His high-level knowledge and experience were easy to access by asking, discussing and managing my scientific work. He is my teacher and will always be. I owe immense thanks for him. Many thanks to Mrs. Gitta Richter for doing her best to make our work in Hannover as easy as possible with her kind way in handling our administrative considerations. My research has become more valuable after the collaboration with Dr. Martin Hohenadler and his work on Quantum Monte Carlo method. I thank him so much. I also had nice fruitful discussions with Dr. Tomonori Shirakawa and Dr. Satoshi Ejima and I am so indebted for that. During the preparation of my thesis I benefited from proofreading of Dr. Simone Faldella with whom I also had useful discussions. I want to express my thanks to him.

This research contributed to the DFG research unit FOR1700 on "Metallic nanowires on the atomic scale" lead by Prof. Herbert Pfnür and Prof. Christoph Tegenkamp. The workshops and conferences organized by this unit have offered very good opportunities for sharing knowledge in my research topic especially those ones organized for PhD students and postdocs. I would like to thank all members of this research unit. I also thank all members of the DFG research unit FOR1807 on "Advanced Computational Methods for Strongly Correlated Quantum Systems" lead by Prof. Fakhre F. Assaad and Prof. Reinhard Noack. This unit was also very useful in sharing knowledge.

I am glad to have Dr. Christoph Brockt, Mrs. Yasemin Ergün, Mr. Jan Bischoff and Mr. Christian Bick as colleagues in our research group for their nice company in working, conferences and "Mensa". I also do not forget our former colleague in the research group, Mr. Christian Isenberg, who was offering me his kind help during my first year in Hannover. Therefore, I thank them all.

I would like to thank Prof. Temo Vekua for the useful discussions and for offering a course on "Methods of Field Theory in Strongly Correlated Low Dimensional Systems" at the institute for theoretical physics in which I was the only student.

I would like to thank all people I joined with for lunch in the "Mensa", it was a nice chance for general discussions and to know other people. I would like to mention from them Prof. Holger Frahm, Prof. Olaf Lechtenfeld, Prof. Manfred Lein, Prof. Norbert Dragon, Prof. Hans-Jürgen Mikeska, Prof. Peter Ulrich Sauer, Prof. Marco Zagermann, Dr. Nikolay Shvetsov-Shilovski, Dr. Andreas Deser, Dr. Rafael Maldonado, Mr. Nicolas Eicke, Dr. Maria Tudorovskaya and Mrs. Natalia Braylovskaya. I ask God to have mercy on the late Prof. Hans-Ulrich Everts who I got to know as a kind and nice person in the institute during my PhD.

I would like to thank my Sudanese colleagues in Leibniz Universität Hannover. Among them I thank Mr. Mazin Hamad, Dr. Amir Dean and Dr. Ahmed Abdalla for their support. I thank all Sudanese friends in Hannover and lower Saxony whose I can not list their names because they are too many. They were very supportive for me and my family. I would like to thank my brothers and sisters in the "Islamische Hochschulvereinigung Hannover" for the good time and support.

I express my gratitude to all friends, colleagues and professors back in Sudan who were supporting me and standing beside me before I came to Hannover. They are so many to name them all.

I am so indebted to my family for their unconditional love and support. My wife Wadha, my daughters Mawadda and Hana, my brothers and sisters Ahmed, Akram, Zeinab, Azza, Sara, and Elnour and my parents Omer and Awatif. My parents are still with me by their support and prayers.

I ask almighty God to reward all people who helped or supported me with good, either I named them or I did not. From the beginning and at the end all praise to be to God who I live in his graces and who I worship through my scientific research and fulfilling my duties in all aspects of my life.

# CV

## Name

Anas Omer Abdelwahab Mohammed

## Personal Information

- Date and place of birth: 19/06/1977, Khartoum, Sudan.
- Sex: Male.
- Citizenship: Sudanese.
- Marital Status: married and father of two daughters.

## Education

- 1983 to 1994, elementary, intermediate and secondary school, Salalah, Sultanate of Oman.
- 1995, Sudanese Secondary School Certificate, Khartoum, Sudan.
- 2000, B.Sc. in Physics from Sudan University of Science and Technology, Khartoum, Sudan.
- 2004, Postgraduate Diploma in Physics from Sudan University of Science and Technology, Khartoum, Sudan.
- 2009, M.Sc. in Computational Physics from Al Neelain University, Khartoum, Sudan.

## Career

- April 2001 - October 2012, Teaching and Technical Assistant , Physics Department, College of Science, Sudan University of Science and Technology, Khartoum, Sudan.
- Since November 2012, Research Assistant, Institute für Theoretical Physics, Leibniz Universität Hannover, Research Group of Prof. Dr. Eric Jeckelmann, Hannover, Germany.

## Languages

- Arabic (native)
- English
- German

## Publications

- A.O. Abdelwahab, E. Jeckelmann and A. Artoli, *Density-matrix renormalization group study of the electro-absorption in conjugated polymers*, in Proceedings of SAIP2011, the 56th Annual Conference of the South African Institute of Physics, edited by I. Basson and A.E. Botha (University of South Africa, Pretoria, 2011), pp. 746 - 751. ISBN: 978-1-86888-688-3. Available online at <http://www.saip.org.za>.
- A. Abdelwahab, E. Jeckelmann and M. Hohenadler, *Ground-state and spectral properties of an asymmetric Hubbard ladder*, Phys. Rev. B **91**, 155119, Published 14 April 2015.
- A. Abdelwahab, E. Jeckelmann and M. Hohenadler, *Correlated atomic wires on substrates. I. Mapping to quasi-one-dimensional models*, Phys. Rev. B **96**, 035445, Published 31 July 2017.
- A. Abdelwahab, E. Jeckelmann and M. Hohenadler, *Correlated atomic wires on substrates. II. Application to Hubbard wires*, Phys. Rev. B **96**, 035446, Published 31 July 2017.
- A. Abdelwahab and Eric Jeckelmann, *Correlations and confinement of excitations in an asymmetric Hubbard ladder*, arXiv:1707.08780, submitted to The European Physical Journal B.